A Study of the Optical Properties of Semiconductor Crystallites

by
William Shaun O'Neill Rodden

A thesis submitted for the degree of
Doctor of Philosophy to the Faculty of Engineering
of the University of Glasgow
1992

Acknowledgements

Thesis Synopsis

The topic of this thesis is the fundamental optical properties of semiconductor crystallites, in particular crystallites of $CdSe_xS_{1-x}$ embedded within a silica glass host. After a brief introduction, a review will be presented of the considerable volume of published work relating to this material together with some relevant theory which can be utilised in the interpretation and understanding of the properties of such crystallites. This will be followed by a chapter describing the principles underlying the preparation of crystallites within a glass matrix, which is in many ways analogous to the crystallisation which occurs in highly saturated aqueous solutions. The equipment used to characterise and probe the properties of this material will then be discussed.

Results will then be presented of experimental measurements on microcrystallites. The use of the technique of Raman scattering from lattice vibrations to determine crystallite stoichiometry will be described. The absorption and photoluminescence of crystallites will then be considered followed by a discussion of the origins of the spectral features observed. The light emitting properties of crystallites and their dependence on crystallite size, stoichiometry, sample temperature and the intensity of the excitation source will then be considered. Results of a time resolved pump probe experiment will then be presented and discussed. This will be followed by a description of an experimental study of sample preparation. The effects of glass doping levels and crystallite growth temperature will be described. This will be followed by a description of an experimental study of the effects of phonon confinement within crystallites. The experimental results relating to phonon confinement will then be compared with the predictions of a phonon confinement model discussed in chapter two. There will then follow a brief discussion of preliminary work performed on other systems of crystallites. Finally, consideration will be given to areas in which the work of this project could be continued and extended.

Of the work presented in this thesis the phonon confinement results represent the first reported quantified observation of quasi-zero dimensional phonons in the microcrystallite doped glass system. The effect of phonon confinement upon the values for crystallite stoichiometry obtained from Raman scattering measurements is clarified and quantified. The thesis also presents a novel method of controlling the sizes of crystallites within a doped glass by altering the initial doping concentration. In addition, results of a preliminary investigation of InAs crystallites and coloured glasses prepared using a silicon dopant will be presented which represent new areas of research.

Table of Contents

List of Tables

List of Figures

Chapter 1 - Introduction

The aim of this thesis is to illustrate some of the properties of very small semiconducting crystals, which are often quite distinct from the properties of the corresponding bulk material. The nanometre sized structures studied here are prepared by a process of diffusive growth, occurring within a suitable doped glass matrix. In this introductory chapter the intention is to describe the material being investigated, the motivation underlying its original development and the reasons why it still attracts the attention of researchers worldwide.

1.1 The Material

The material is a glass which is initially doped with a few weight percent of compounds containing cadmium, selenium and sulphur. These materials initially form isolated ions within the glass matrix, however, under suitable thermal conditions, these ions may migrate by means of diffusion and cluster together to form microscopic crystals of $CdSe_xS_{1-x}$ within the glass host (see Figure 1.1, below).
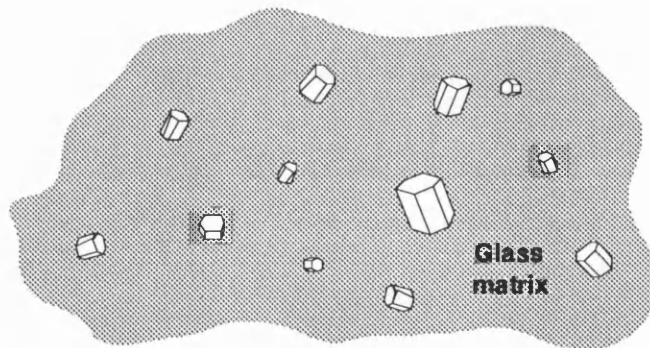
Figure 1.1   Schematic illustration of crystallites in CdSeS microcrystallite doped glass [1.3,1.4].

The clustering results from the Cd, Se and S species attempting to minimise their free energy. Due to the crystal structure of $CdSe_xS_{1-x}$ (hexagonal wurtzite) these crystal tend to grow in the form of small hexagonal columns [1.1,1.2]. Since the host glass is an amorphous material, the positions and orientations of the crystallites are random and the nature of the fabrication process (diffusive growth) tends to result in a significant distribution in the sizes of the crystallites.

Although the glass matrix has been referred to as a mere "host" material it is not an entirely passive host. Therefore, although of primary interest in this thesis are the properties of the crystallites, the glass host will be briefly discussed. The host material is usually a borosilicate glass or occasionally a soda-lime glass. Typical chemical compositions of such glasses are given in Table 1.1, below, together with a typical composition of $CdSe_xS_{1-x}$ doped glass.

Borosilicate Glass

Component	Relative Concentration
SiO_2	80.5%
B_2O_3	12.9%
Na_2O	3.8%
Al_2O_3	2.2%
K_2O_3	0.4%

Soda-Lime Glass

Component	Relative Concentration
SiO_2	71-73%
Na_2O	12-15%
CaO	10-12%
MgO	1-4%
Al_2O_3	0.5-1.5%

CdSeS Microcrystallite Doped Glass

Component	Relative Concentration	Component	Relative Concentration
SiO_2	68.9%	CdO	0.59%
B_2O_3	11.5%	Se	0.07-0.23%
ZnO	11.3%	S	0.019-0.044%
Sb_2O_3	1.1%		
Al_2O_3	1.0%		

Table 1.1 Typical compositions of borosilicate, soda-lime and microcrystallite doped glasses [1.3,1.4].

The components of silica glasses are usually chosen for a variety of reasons. The most important reason for adding other oxides to SiO_2 is to lower the softening temperature of the mixture (SiO_2 only softens above 1600C [1.5]). Other constituents are often added to make the molten glass easier to work with or to give it some desired thermal, mechanical or optical property. The glass host is therefore an extremely complex material capable of interacting with the semiconductor crystallites in a number of ways, both during and after the crystallite growth process. An obvious method by which the glass host can affect the properties of the crystallites is by supplying impurities during the stages of crystallite formation. One common constituent of glass is zinc oxide of which, it is believed, the zinc can be easily incorporated into the crystallites to form CdSeZnS [1.4]. Researchers have also suggested that the crystallite surface may be of importance in determining its properties. If this is so, the nature of the glass host, which is in close contact with the crystallite surface, is of obvious relevance. The manner in which the semiconductor/glass interface affects a crystallite's properties is, however, speculative.

In order to study finite size effects using such crystallites it is important to be able to control, in some manner, the sizes of the crystallites within the sample. In the case of such semiconductor doped glasses this can be done relatively easily by altering the crystallite growth conditions. As might be expected, a longer growth period or higher growth temperature (within

certain limits, see chapter three) produces larger crystallites. By altering the sample preparation parameters the crystallites can be varied from a few nanometres up to a several hundred nanometres in size.

From the above discussion it is probably difficult to visualise what such a material, containing nanometre sized crystallites, would look like. The material can be produced in the form of large pieces of coloured glass. The colour, ranging from yellow through orange to deep red (almost black), being determined largely by the absorption edge of the crystallites (which depends upon the crystallites' stoichiometry).

1.2 Historical Summary

The motivation which originally prompted researchers to develop materials of this type was simple: "to produce a most excellent red glass"[†] for its intrinsic beauty and its commercial value ([†] Johann Kunckel, 1679, see reference later in this section [1.6]). Although the history of $CdSe_xS_{1-x}$ doped glass only dates from the second half of the nineteenth century, the technique of colouring a transparent glass by producing within it a colloid-like suspension of microscopic particles or crystallites is considerably more ancient. Such a composite material, containing microscopic gold particles, can be produced by adding small amounts of gold to a glass melt and results in a brightly coloured red glass known as "gold-ruby" [1.7].

The problem of preparing a translucent red glass, by adding small quantities of gold to a glass melt, was one to which both glassmakers and alchemists devoted much of their research during the seventeenth century. Although later glass technologists often developed coloured glasses for purely ornamental purposes, these early researchers were motivated by much more serious considerations. They believed that drinking from a vessel made of such a material would provide protection against all manner of ills. It was the medicinal powers associated with these glasses which justified the considerable research necessary to develop them and the high prices for which they sold. Developing glass processing techniques was then, and to a large extent remains, a process of trial and error. This, coupled with the product's great commercial and mystic value, prompted researchers to attempt to protect the secrecy of their production process. Johann Kunckel, who was the first to produce such a gold-ruby glass on a commercial scale and who is generally recognised as its inventor, was understandably anxious to protect his discovery :-

> "I have devoted much time to this subject, and can now, thank Heaven, as well as the finest ruby, produce a most excellent red glass: since it has cost me so much time and trouble, and since it is a very rare product, no-one will object to my keeping it secret this time."
>
> Johann Kunckel in his book
> "The Complete Art of Glassmaking"
> published in 1679 (Frankfurt and Liepzig).

3

The "secret" of making large pieces of gold-ruby glass died with Johann Kunckel in 1703 and was not rediscovered until the nineteenth century[§] [1.6-1.8].

Although earlier seventeenth century researchers were able to produce gold-ruby glass on a very small laboratory scale it was Kunckel who made it commercially viable. However, the first use of microscopic gold particles to produce colour in a glass-like substance possibly predates these researchers by over two thousand years. R.C. Thompson interprets the records on some Assyrian tablets of the seventh century B.C. as a recipe for a red glaze made by melting 7200 parts powdered glass with 1 part gold, along with some tin and antimony[‡] [1.7,1.11].

When the art of producing large pieces of gold ruby glass was rediscovered in the nineteenth century the material was no-longer regarded as possessing great medicinal properties and was reduced to a mere substance with which to make ornamental glassware. Since all that was required from such a material was beauty it was no-longer necessary to prepare it from the mystic metal gold and other types of translucent red glass began to compete with gold-ruby.

In the second half of the nineteenth century a yellow glass was developed in Bohemia which was known by the trade name of "Kaiser Yellow". This glass, like the gold-ruby of Kunckel, could, by quite rapid cooling of the melt, be made in a transparent form which only assumed its bright yellow colour upon reheating (a process known as "striking").

Like gold-ruby, "Kaiser Yellow" assumed its colour upon striking by allowing the "dissolved" dopants to migrate and form a suspension of small particles within the glass matrix. In the case of "Kaiser Yellow" the particles were tiny crystals of cadmium sulphide. A more complete discussion of the striking process can be found in chapter three. The application of CdS doped glass was mainly in the production of commercial artware. The next part of this historical summary will show how this "Kaiser Yellow" led to the development of a red glass at least as "excellent" as Kunckel's.

In 1865 J.T. Pelouze observed that selenium produced a faint pink colour when added to a transparent glass melt. Several decades later, selenium was added to a CdS doped glass and produced a material whose colour could be varied, by altering the quantity of selenium, from deep red to almost any shade of orange. F. Welz of Klostergrab, Bohemia, obtained a patent for such a glass in 1891.

---

§ The precise year of Kunckel's death is uncertain. Although Kunckel was an alchemist, believing it to be "gross ignorance" to deny that base metals could be transformed into gold, he exposed several false claims of success made by other alchemists. However, he did not believe the more extreme claims of some alchemists that it was possible for alchemy to create living creatures from inanimate objects: "There are in chemistry separations, combinations, purifications, but there are not transmutations. The egg hatches by the heat of the hen. With all our art, we cannot make an egg. We can destroy it and analyse it but that is all." [1.9,1.10]

‡ At Ninevah, Assyrian tablets have been discovered which describe in detail glass making furnaces and processing techniques which represent the state of the art of seventh century B.C. glassmaking. To put this into the perspective of the history of glassmaking, one of the oldest known pieces of man-made glass was found in Egypt and is dated at about 7000 B.C. [1.3]

This glass, like gold-ruby and "Kaiser Yellow", could also be produced in a transparent form which would only assume its deep colour upon striking. During the striking of this glass, which later became known as "selenium-ruby", small crystallites of $CdSe_xS_{1-x}$ are formed, with the glass colour being largely determined by the sulphur to selenium ratio. This material, although originally developed for ornamental glassware, soon began to attract the attention of researchers, with the first scientific papers relating to it dating from 1911 [1.12].

Of these early experiments the one of most relevance to this thesis was carried out by G.A. Suckstorff around 1930. Suckstorff, while studying the striking of CdS glass, exposed a 55cm long strip of the glass, in its clear, unstruck, condition, to a temperature gradient. He found that the colour of the annealed glass varied long its length (and hence with striking temperature) from pale yellow to deep yellow [1.13]. In the light of recent work it is difficult not to conclude that Suckstorff was observing the effects of quantum confinement of electrons and holes in all three dimensions. (It is now known that decreasing the striking temperatures of such glasses results in the growth of smaller crystallites and, for sufficiently small crystallites, a shift in the absorption edge towards longer wavelengths resulting from the confinement of the carriers) It seems likely that manufacturers of "Kaiser Yellow" or selenium-ruby, while producing material for ornamental glassware, would occasionally, and quite unintentionally, have grown crystallites in which the carriers were confined in all three dimensions in order to obtain a particular shade of yellow, orange or red. It is probably reasonable to refer to these pieces of glassware, manufactured over a century ago, as engineered quantum mechanical devices which operated at room temperature and had a commercial application, several decades before the development of quantum mechanics.

Microcrystallite doped glass, as well as its original artistic use and the attention it attracted from scientific researchers, also found engineering applications. It has, in the past, been used as a red filter in front of a white light source to serve as a warning on railway networks, but today it is usually found in the form of long pass optical filters used in scientific and engineering optical systems. For example, it can be used within optical spectroscopy systems to pass the light emitted by a sample while blocking the shorter wavelength radiation from the excitation source (in chapter four it will be described how this property is utilised within a photoluminescence excitation spectroscopy experiment). The next section will discuss why this material, first produced over a century ago, has, in recent years, attracted considerable research attention from theorists, experimental scientists and engineers.

1.3 Recent Research Interest

The recent, and considerable, research interest which microcrystallite doped glasses have attracted can be viewed as part of the current investigation into the physics and technology of low dimensional semiconductor systems.

The advent of crystal growth techniques such as metal-organic chemical vapour deposition and molecular-beam epitaxy have made possible the precision growth of semiconductor structures containing layers of material only a few atoms thick. By suitable choice of the semiconductor which forms such a layer "quantum wells" can be created in which the electrons and holes are confined in the dimension perpendicular to the layer. The study of these quasi-two dimensional systems has allowed several novel physical phenomena to be investigated. Technologically these structures have also proved to be important, allowing, for example, semiconductor lasers with reduced threshold currents to be constructed [1.14]. The quantum confinement within such structures offers engineers an additional variable with which the effective bandgap of the material can be engineered to suit a particular device application.

An obvious extension of this work is to produce structures in which the carriers are confined in two or three dimensions. This increases the number of adjustable parameters which can be used to engineer the band-structure of the system [1.15]. These "quantum wires" (two dimensional confinement) and "quantum dots" (three dimensional confinement) offer the opportunity to investigate physical phenomena not observable in quantum wells and, if the theorists are to be believed, may prove to be of great technological importance. Experimentalists have endeavoured to produce quantum dots, the topic of this thesis, by a variety of techniques, some of which are summarised below.

(i) High Resolution Lithography

Lithographic techniques, utilising electron beams or x-rays, can be used to produce a mask on top of a sample of quantum well material. The areas not protected by this mask can be damaged or removed, by wet or dry etching, in order to create barriers which confine the carriers in the dimensions parallel to the quantum well [1.16,1.17].

(ii) Precipitation from a Liquid Solution

This type of process synthesises clusters of semiconductor atoms (eg CdS, PbS, InAs) by means of chemical reactions within a liquid solution. The properties of these crystallites can be investigated while they are suspended in solution or they can be filtered from the solution [1.18,1.19].

(iii) Evaporation and Sputtering Techniques

This method of crystallite preparation, which involves the evaporation or sputtering of the crystallite material onto a substrate, has been used to prepare crystallites of semiconductors including Si, Ge, GaP and CdS [1.20-1.22]. In this process the atoms, or groups of atoms, evaporated or sputtered onto the substrate cluster together to form crystallites and a polycrystalline layer is created. Samples of microcrystalline silicon have been prepared by these techniques with properties which have been interpreted as resulting from three dimensional carrier confinement [1.23].

(iv) Precipitation from a Solid Solution

This method of crystallite preparation involves "dissolving" at high temperature the components of the crystallites within a host "solute". When the temperature is reduced the solubility of these components within the host material is reduced and crystallites are precipitated from the now over-saturated solution. Often an amorphous glass forms the "solute" material. This method, which will be discussed in greater detail in chapters three and five, is the means by which crystallites are prepared within semiconductor doped glasses. In addition to the interest associated with the fundamental physical properties of quantum dots, semiconductor doped glasses have also attracted attention from researchers interested in optical switching [1.24].

Precipitating crystallites within a glass matrix, requiring only the raw materials, an appropriate crucible and a suitable furnace, is amongst the least equipment intensive of the methods currently available for the production of quantum dots. Despite the relatively crude equipment necessary to prepare these materials they offer researchers a unique system in which to study the most extreme conditions of three dimensional quantum confinement and, in this respect, are yet to be matched by samples produced by other methods.

Subsequent chapters will discuss the properties which microcrystallites might be expected to possess (chapter two), the principles governing their preparation in glass (chapter three) and some of the optical techniques available for their characterisation (chapter four). Chapter five will then present the results of an experimental investigation into the optical properties of semiconductor crystallites in glass. The electronic states of such structures were investigated by absorption and photoluminescence spectroscopies. Vibrational states of the finite crystal were investigated using Raman spectroscopy and results were obtained which are consistent, both qualitatively and quantitatively, with three dimensional phonon confinement. The proper interpretation of some of these measurements necessitated an understanding of the crystallite growth process. A study of the growth process was therefore undertaken and the results of this investigation are also discussed in chapter five. As well as the work on $CdSe_xS_{1-x}$ crystallites in glass the thesis will also present preliminary results of an investigation of other systems of crystallites, such as InAs crystallites prepared in an aqueous solution.

Overall, the aim of this thesis is to elucidate some of the fundamental physical properties of semiconductor crystallites. If small semiconductor structures are to play a role in future electronic systems it will be necessary to obtain a degree of understanding of the fundamental behaviour of particles (electrons, holes and phonons) within such structures. It is hoped that the work presented here, in some small measure, advances this understanding.

Chapter 2 - Predicted Properties of Quantum Dots

This chapter will discuss some of the physical properties which quantum dots might be expected to possess. This discussion will partly take the form of a literature review, briefly describing the models used by various researchers to predict the properties of quasi-zero dimensional systems. In addition to this general review a discussion will be presented of properties which might be expected to be specific to small crystallites embedded within a glass matrix.

In order to illustrate the properties peculiar to zero dimensional systems, it is appropriate to present a brief summary of the relevant characteristics of bulk, three dimensional semiconductors, in particular the II-VI material cadmium selenium sulphide. This will be followed by a short discussion of the properties of semiconductors as the carriers within the structures become confined in first one then two and, finally, in all three dimensions. The properties specific to zero dimensional systems will then be discussed more fully, in particular those properties relevant to the experimental results presented in chapter five. Theoretical calculations will also be presented which, in chapter five, will be used to analyse experimental measurements made on real microcrystallites.

2.1 Properties of Bulk Semiconductors

2.1.1 Crystal Structure

Bulk $CdSe_xS_{1-x}$ usually occurs with a hexagonal wurtzite structure, although CdS is quite commonly found with a cubic structure [2.1]. Figure 2.1 illustrates the atomic arrangement for a binary compound with such a hexagonal wurtzite structure.

Figure 2.1
Atomic arrangement for a binary compound (CdS) with a hexagonal wurtzite structure [2.1].
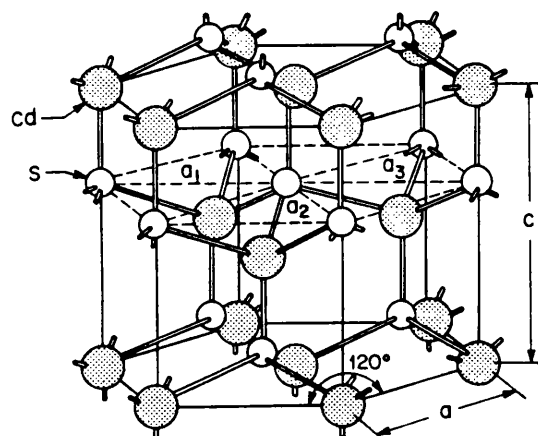
This, as will be seen later, has relevance for the shape of the crystallites studied in this thesis. Several researchers have shown, by means of transmission electron microscopy, that the crystallites occur in the form of hexagonal columns. This is, of course, consistent with the above crystal structure.

2.1.2 Energy States

A hexagonal wurtzite crystal structure results in an energy band structure of the type illustrated schematically in Figure 2.2, below [2.2].
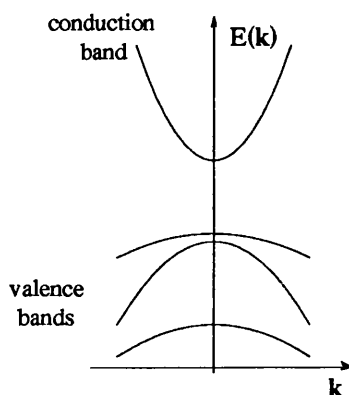
Figure 2.2   Schematic diagram of the energy band structure for a material with a hexagonal wurtzite crystal.

The energy gaps for common II-VI materials are tabulated in Table 2.1, together with some of their other physical properties [2.3,2.4].

Material	Crystal Structure	Energy Gap	Type of Transition	Melting Point
CdS	wurtzite	2.42eV	direct	1475C
CdSe	wurtzite	1.73eV	direct	1239C
CdTe	wurtzite	1.43eV	direct	1092C
ZnS	wurtzite	3.66eV	direct	1830C
ZnSe	wurtzite	2.67eV	direct	1520C
ZnTe	wurtzite	2.25eV	direct	1295C

Table 2.1   Minimum energy gaps at 300K and melting points of various II-VI compounds.

For ternary II-VI alloys of the form AB_xC_{1-x} the energy gap is given by [2.4]:-

9

$$E_g(x) = xE_g^{AB} + (1 - x)\,E_g^{AC} - x(1 - x)\,b \qquad \text{Equation 2.1}$$

where E_g = Energy gap of AB_xC_{1-x}

E_g^{AB} = Energy gap of AB

E_g^{AC} = Energy gap of AC

b = Bowing parameter

The values for the bowing parameter for several II-VI ternary systems are given in Table 2.2, below [2.4].

Material	b
$ZnSe_xS_{1-x}$	0.41
$ZnSe_xTe_{1-x}$	1.27
$CdSe_xS_{1-x}$	0.31
$CdSe_xTe_{1-x}$	0.85
ZnS_xTe_{1-x}	3.00
CdS_xTe_{1-x}	1.70

Table 2.2 Bowing parameters (b) for several II-VI ternary compounds.

Thus for the $CdSe_xS_{1-x}$ system the energy gap at 300K, as a function of x, is given by :-

$$E_g = (1.73\,x + 2.42\,(1 - x) - 0.31\,x\,(1 - x))\ eV \qquad \text{Equation 2.2}$$

If crystallites within a semiconductor doped glass are believed to be sufficiently large for quantum confinement effects to be negligible, Equation 2.2 can be used to estimate the stoichiometry of the ternary semiconductor. This is subject to the usual errors associated with determining the exact energy gap from absorption or photoluminescence measurements.

In the experimental results presented in chapter five microcrystallites will be investigated with a range of sulphur to selenium ratios. This stoichiometry variation alone, neglecting finite size effects, results in a variation of the absorption edge at 300K between ~1.73eV (~720nm) and ~2.42eV (~512nm). It also shifts the positions of the CdSe-like and CdS-like LO phonons. As will be discussed later, in chapter five, it was at times found necessary to completely separate effects due to stoichiometry variations from those arising from the finite sizes of the crystallites. For this reason some experiments were performed on CdSe crystallites, with negligible sulphur content.

Assuming a simple parabolic band structure, with no interaction between electrons and holes, the well known result for the density of states in a bulk semiconductor is given by [2.5]:-

$$D(E) = \frac{1}{2\pi^2}\left(\frac{2m^*}{\hbar^2}\right)^{\frac{3}{2}} E^{\frac{1}{2}} \qquad \textbf{Equation 2.3}$$

where D(E) = Density of states
        m = Effective mass
        $\hbar$ = (Planck's constant)/2π
        E = Energy

Later we will discuss schematically the manner in which the density of states alters as the dimensionality of the system is reduced from three to two to one and finally to zero. The density of states of a system of quantum dots will then be discussed in terms of a simple model as a function of the dot size, the carrier's effective mass and a broadening parameter.

2.1.3 Light Absorption

Here the light absorbing properties of II-VI semiconductors will be briefly reviewed in order that the differences between the absorption of bulk material and microcrystallites might be more fully appreciated in chapter five. At temperatures such as 300K the absorption edge of II-VI materials has been found to vary exponentially with photon energy (see Equation 2.4, below) [2.6,2.7].

$$\alpha(h\nu) = \alpha^\circ \exp\left(\frac{b(h\nu - h\nu_o)}{kT}\right) \qquad \textbf{Equation 2.4}$$

where α = Absorption coefficient
        ν = Frequency of absorbed light
        α°, ν_o = Constants
        h = Planck's constant
        k = Boltzmann's constant
        T = Absolute temperature

This relationship is known as "Urbach's Rule". At low temperatures structure is visible in the absorption edge associated with exciton absorption. The exponential absorption edge evident at high temperatures and the excitonic structure present at low temperatures are illustrated in Figure 2.3, below, for CdS.

Figure 2.3
The absorption of bulk CdS at various temperatures [2.8,2.9].
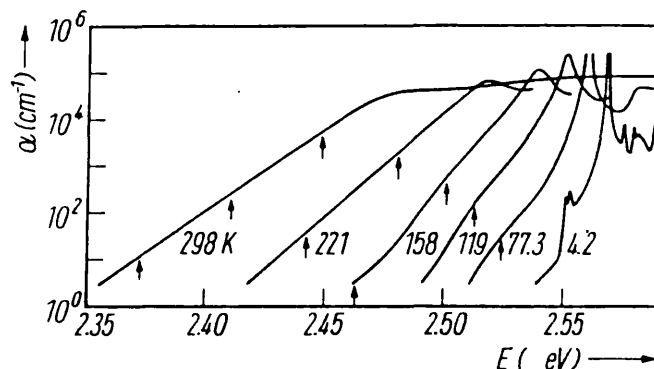
2.1.4 Carrier Recombination and Light Emission

Common methods by which light can recombine radiatively in bulk direct band gap semiconductors include:-

(a) Direct band to band recombination.

(b) Formation of a free exciton of which the electron and hole, after some characteristic lifetime (for example 10^{-8}s in CdS [2.10]), recombine radiatively.

(c) Recombination via states within the energy gap associated with impurities or defects.

Some of these processes are illustrated schematically in Figure 2.4.
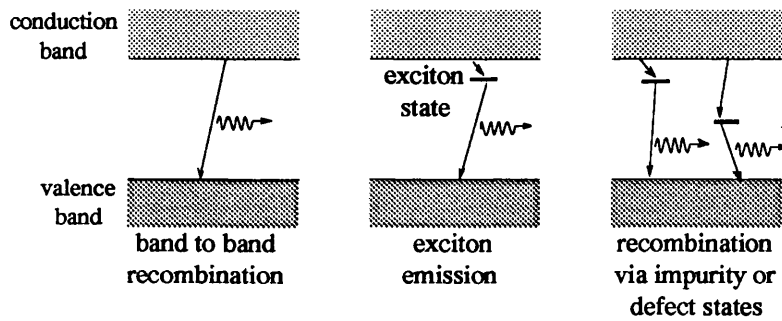
Figure 2.4   Examples of possible light emission processes.

Other typical radiative recombination mechanisms include the recombination of excitons bound to impurities within the semiconductor and recombinations involving the emission of phonons. Photons emitted along with phonons possess an energy lower than the energy lost by the electron, with the energy difference being that carried by the phonons [2.10]. The properties of phonons in bulk semiconductor crystals will be discussed in the following section. Figure 2.5, below, illustrates a typical emission spectrum from bulk GaAs, in which the features have been identified as resulting from some of the recombination processes mentioned above.
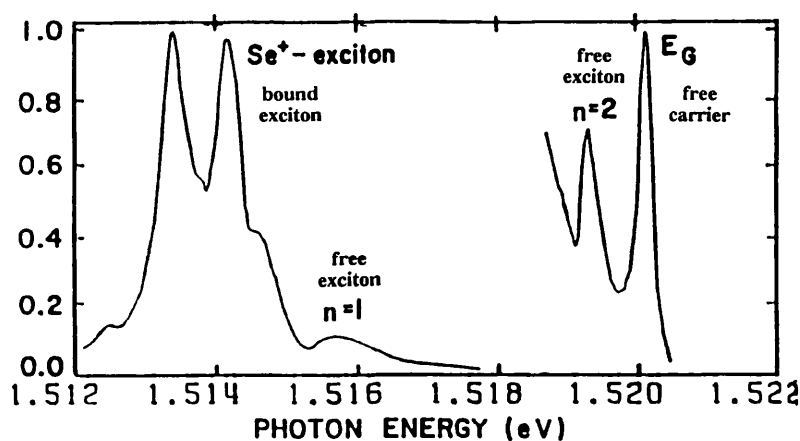
Figure 2.5   Example emission spectrum illustrating features associated with a Se bound exciton, a free exciton (n=1 and n=2 states) and free carrier recombination [2.10,2.11].

12

2.1.5 Light Scattering from Phonons in Bulk Semiconductors

The scattering of light from lattice vibrations (phonons) in bulk semiconductors requires the conservation of energy and wavevector, as specified by the following equations [2.12,2.13].

$$\omega = \omega' \pm \omega_p \quad \textbf{(a)}$$

Equations 2.5

$$q = q' \pm q_p \quad \textbf{(b)}$$

where ω = Frequency of incident radiation
ω' = Frequency of scattered radiation
ω_p = Frequency of phonon
q_p = Wavevector of incident radiation
q' = Wavevector of scattered radiation
q = Wavevector of phonon

The positive and negative signs in the above expressions refer respectively to the destruction (anti-Stokes scattering) and the creation (Stokes scattering) of a phonon in the interaction. These equations refer to Raman scattering from a single phonon, higher order interactions involving scattering from more than one phonon can also occur. Since scattering from multiple phonons involves additional particles it is less probable than single phonon scattering. The wavevectors of phonons which satisfy the above equations are very small compared with those at the edge of the first Brillouin zone, hence Raman scattering occurs from approximately zone centre phonons.

Figure 2.6, below, illustrates diagrammatically the manner in which the interaction between photons and phonons can occur. The diagram has been drawn for the Stokes component of the scattered radiation.

Process (a), in Figure 2.6, dominates the other two processes in scattering intensity, thus the Raman scattering observed in this thesis represents an interaction between light and phonons through the intermediary of the electrons. The electronic states in the above process may be real or virtual. Other, more complicated, diagrams may be constructed to link ω_i to ω_s and ω. These, however, involve a greater number of interaction processes and are, consequently, less probable.
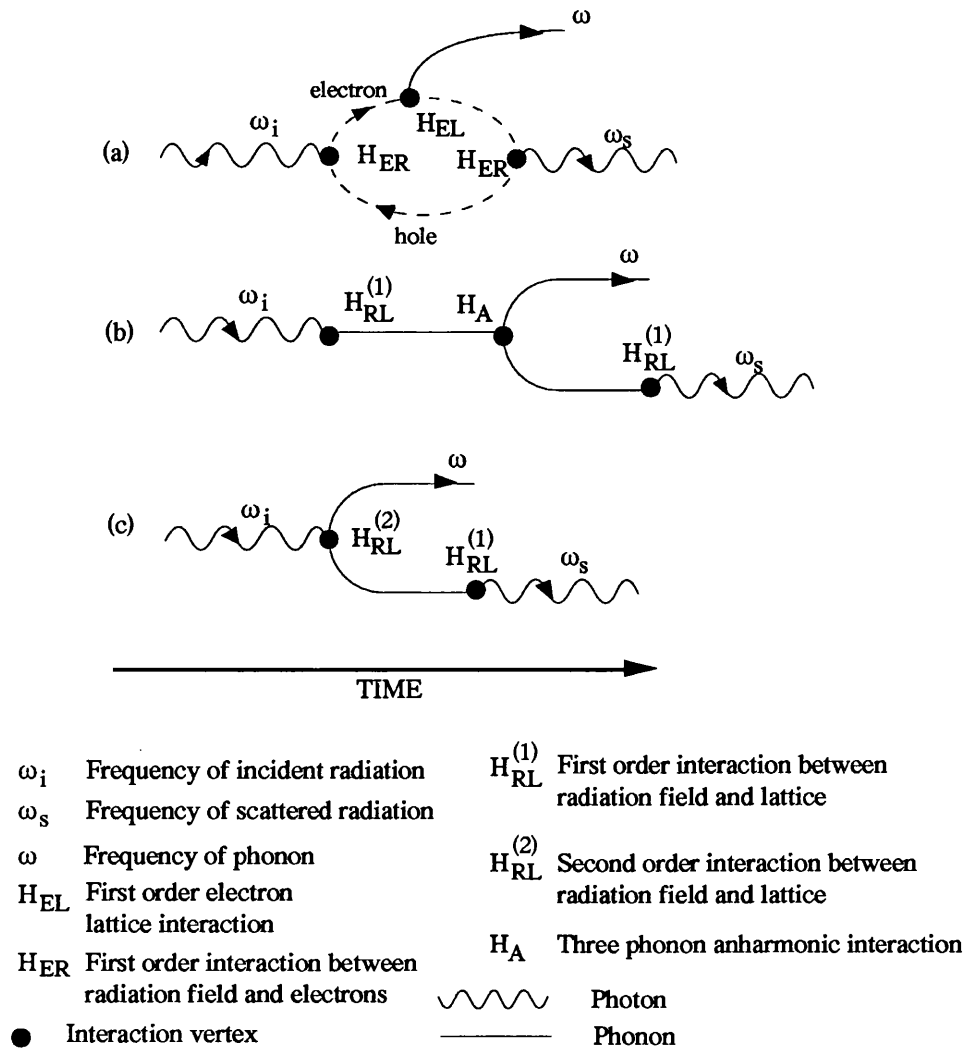
Figure 2.6   Interaction processes resulting in first-order
Raman scattering [2.13].

Also, of relevance to some of the Raman scattering work presented in this thesis are resonant
effects. If, under the excitation conditions being used, the electronic states are real and long
lived then a resonant enhancement of the Raman scattering cross-sections will occur. Often of
great importance in Raman scattering from bulk semiconductors are the selection rules which
determine the scattering allowed for a particular polarisation of the incident light and the type
and orientation of the crystal being investigated. In the case of microcrystallite doped glass, the
crystallites are randomly orientated within the glass matrix. Since, during a Raman scattering
experiment, scattering will occur from a large number of crystallites, the overall orientation of
the sample of semiconductor doped glass is irrelevant to the scattering which will occur. For
this reason the selection rules resulting from crystal orientation will not be discussed.
Properties of Raman scattering in bulk crystals of particular relevance to this thesis include its
sensitivity to crystal disorder and the composition of ternary materials such as $CdSe_xS_{1-x}$.
Figure 2.7 shows typical examples of Raman scattering spectra which illustrate its use as a

probe of disorder and stoichiometry.
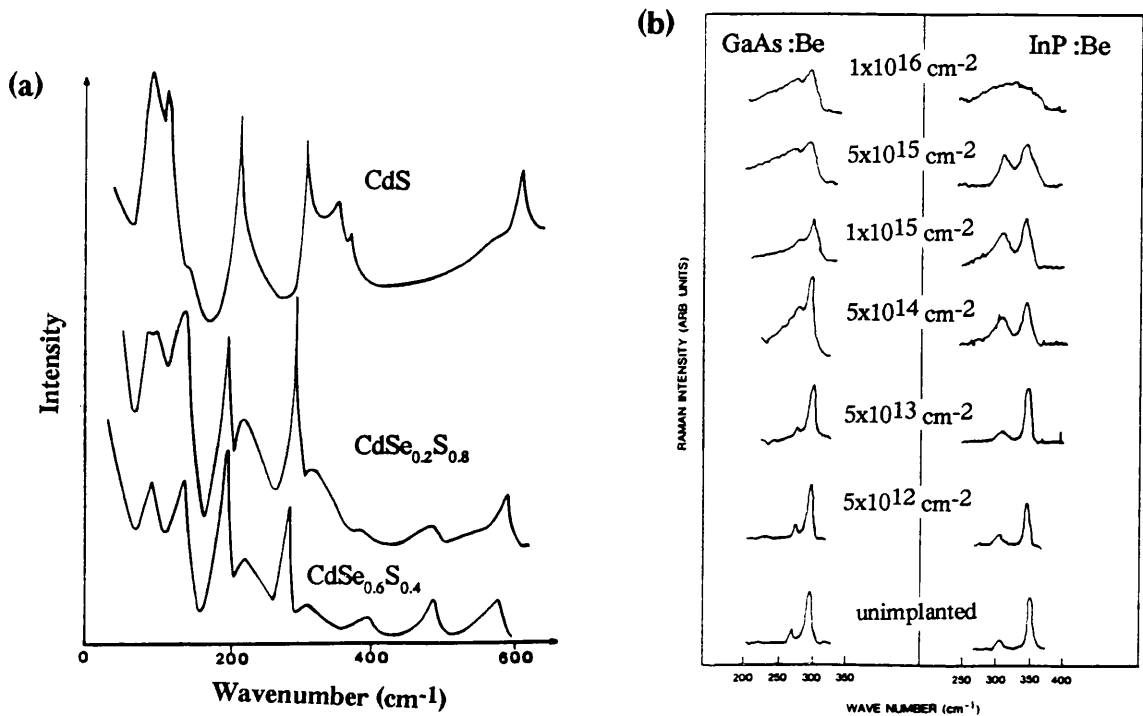
Figure 2.7 (a) Raman scattering as a probe of stoichiometry [2.14].
            (b) Raman scattering as a probe of disorder [2.15].

In Figure 2.7(a) the features are attributed to scattering from combinations of zone centre and zone edge phonons. The spectra considered in chapter five contain fewer features with only the CdSe-like and CdS-like LO phonons being observed (these are the intense features at around $200cm^{-1}$ and $280cm^{-1}$ respectively in Figure 2.7(a)). Both the wavenumbers at which these features occur and their relative intensities contain information about the stoichiometry of the crystal. Figure 2.7(b) illustrates the effect of disorder upon the Raman spectra of GaAs and InP which have been damaged by Be implantation. As the implantation dose is increased the material is damaged to a greater extent and the Raman spectrum becomes broader, as the selection rules which apply in crystalline material are relaxed.

2.2 Effects of Reduced Dimensionality

This section will present a brief discussion of the effects of reducing the dimensionality of a semiconductor system. A short comparison of the properties of bulk material with those of two, one and zero dimensional systems will be presented, followed, in section 2.3, by a more detailed discussion of zero dimensional systems, the topic of this thesis.

15

2.2.1 Density of States

Assuming a parabolic dispersion relation for the carriers, the density of states for systems of reduced dimensionality can be easily calculated by the same method used for bulk material. The form of these functions are given below [2.16].

Equations 2.6

Three Dimensional System

$$D(E) = \left(E - E_g\right)^{\frac{1}{2}} \quad \text{(a)}$$

Quasi-two Dimensional System

$$D(E) = \sum_n H(E - E_g - E_n) \quad \text{(b)}$$

H = Step function
n labels the sub-band

Quasi-one Dimensional System

$$D(E) = \sum_{nm} (E - E_g - E_{nm})^{-\frac{1}{2}} \quad \text{(c)}$$

n,m label the sub-band

Quasi-zero Dimensional System

$$D(E) = \sum_{lmn} \delta(E - E_g - E_{lmn}) \quad \text{(d)}$$

δ = Dirac delta function
l,m,n label the energy state

These density of states functions are illustrated diagrammatically in Figure 2.8.
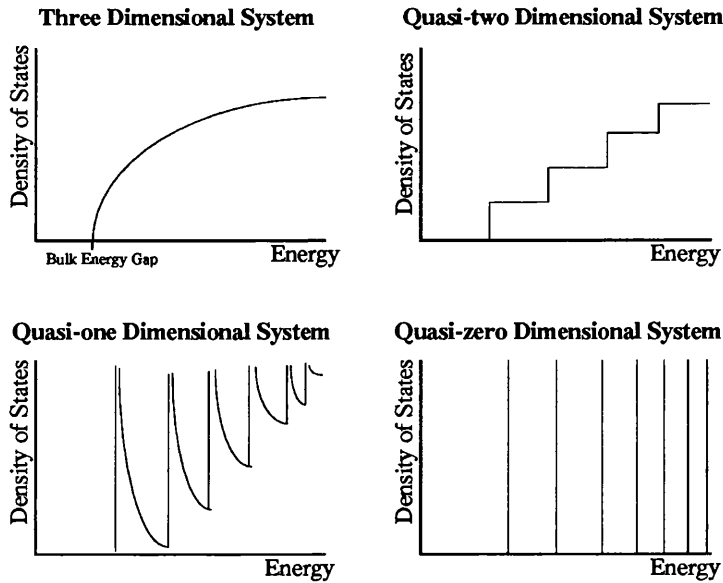
Figure 2.8 Idealised density of states for bulk and low dimensional systems.

Figure 2.9, below, schematically illustrates the effect of broadening upon the density of states of a quantum dot system. It can be seen that such broadening results in a density of states in which the features associated with reduced dimensionality are "smeared out" giving a more

16

"bulk-like" system. Such broadening also affects the features of two and one dimensional systems. This broadening will be discussed later on a more quantitative basis, with particular reference to microcrystallites.
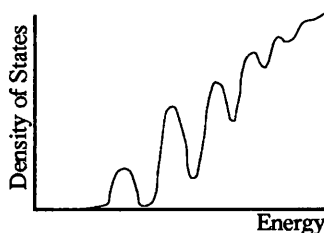
Figure 2.9   Density of states for a quasi-zero dimensional system with broadening.

2.2.2 Carrier Confinement and Light Emission

Carrier confinement can have a variety of effects on the light emitting properties of low dimensional systems compared with bulk material. The most obvious effect is a change in the emission wavelength due to the carrier confinement in one or more dimensions. Other effects include an increase in the exciton binding energy in two dimensional systems, allowing the excitons to exist and emit light at room temperature. In three dimensions the excitons, with a low binding energy, can be thermally ionised easily and, consequently, are unlikely to participate in the emission of light. Confinement in a low dimensional system can also alter the relative importance of various carrier recombination mechanisms. For example, surface recombination may be of great importance in such structures. Reduced dimensionality also has implications for laser emission. It is well known that quantum well lasers have a reduced threshold current compared with simple diode lasers and it is suspected that confinement in additional dimensions may result in further enhancement of laser action in semiconductors [2.17,2.18]. Some of these effects will be mentioned later in this thesis, particularly those of relevance to microcrystallites.

2.2.3 Phonons in Systems of Reduced Dimensionality

There are several features of low dimensional systems which can effect phonons in a manner which can be observed experimentally using Raman scattering. The most important of these effects are discussed below.

(i) Surface Modes

The existence of surfaces within such systems can result in vibrational modes which are confined around the surfaces or interfaces. The amplitude of these vibrations often decay with distance away from the surface or interface. When these modes exist they have properties and

frequencies which are distinct from those of vibrations occurring within the volume of the structure. Of course, in order for such modes to exist the surfaces must be free to vibrate and must not be "clamped" or heavily damped surfaces [2.19,2.20].

(ii) Phonon Confinement

When a phonon is confined in any dimension its localisation in space necessarily results in an "uncertainty" in its wavevector. Thus, the nearest phonon to a $q=0$ phonon contains a range of wavevectors around $q=0$. When light scatters from such a phonon the resulting Raman spectra will be broadened showing a relaxation in the $q \approx 0$ selection rule. A model for this selection rule relaxation in quasi-zero dimensional systems will be discussed later in this chapter and, in chapter five, applied to the analysis of experimental spectra from microcrystallites.

(iii) Zone Folding

If the phonon confinement is only partial and the partially confining potential is periodic an effect known as zone folding can occur (a superlattice is an example of such a system). In such a structure the phonon travelling through the periodic, partially confining potential will experience a Brillouin zone of width $2\pi/d$, where "d" is the system's periodicity, rather than the Brillouin zone of the corresponding bulk crystal which is of width $2\pi/a$ ("a" is the lattice parameter) [2.21]. This results in phonons with wavevectors $2\pi/d$, $4\pi/d$, etc being physically identical to $q=0$ phonons. This "folding back" of the Brillouin zone is illustrated in Figure 2.10, below.

a = Period of lattice
d = Period of low dimensional structure
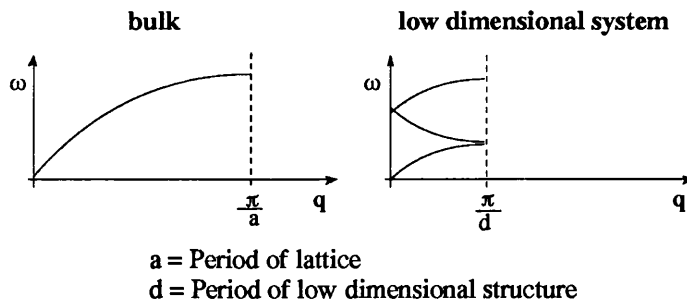
Figure 2.10   Effect of a periodic low dimensional structure on a phonon travelling through it.

In such a system, the folded acoustic modes of the bulk material can now be observed by Raman scattering, since at $q=0$ they now possess a non-zero energy. For a system of microcrystallites within a glass matrix the confinement is strong and the crystallites are widely spaced, causing phonons to be completely localised around individual crystallites. The crystallites are also randomly distributed and do not form a periodic system. Hence, this zone folding effect will not occur in microcrystallite doped glass.

18

2.3 Properties of Zero Dimensional Systems

2.3.1 Energy States

Several authors have constructed models to calculate the energy levels within zero dimensional structures. These models are based on the "envelope function" approximation. Within this approximation the periodic variation in potential from atom to atom within the crystal is neglected and the properties of this periodic potential are incorporated within the effective masses of the carriers and the electric constants of the bulk material. A mathematical justification of this approximation can be found in reference [2.22]. With the properties of the periodic crystal contained within the effective masses and the material's electric constants, the Hamiltonian for a microcrystallite can be written in the form of Equation 2.7 (see for example [2.23-2.25]).

Equation 2.7

$$H = -\frac{\hbar^2}{2\,m_e^*}\,\nabla_e^2 - \frac{\hbar^2}{2\,m_h^*}\,\nabla_h^2 - \frac{e^2}{\varkappa\,|r_e - r_h|} + V_e(r_e) + V_h(r_h) + V_D(r_e, r_h)$$

where H = Hamiltonian
e = Electronic charge
$\hbar$ = (Planck's constant)/2π
m_e, m_h = Effective masses of electrons and holes respectively
$\varkappa$ = Dielectric constant = $4\pi\varepsilon_r\varepsilon_0$
V_e = Confining potential for electrons
V_h = Confining potential for holes
V_D = Dielectric interaction between crystallite and host material
r_e, r_h = Positions of electron and hole

The first two terms describe the kinetic energies of the electron and hole respectively. The third term represents the Coulomb interaction between an electron and hole. V_e and V_h are the confining potentials of the electron and hole respectively, which need not necessarily be the same. The final term results from the dielectric interaction between the crystallite, containing charges (electrons and holes), and the host material. Whenever an electron-hole pair is created within the crystallite this dipole will induce a polarisation in the dielectric host material (see Figure 2.11). The energy required to induce this polarisation is described by this final term.
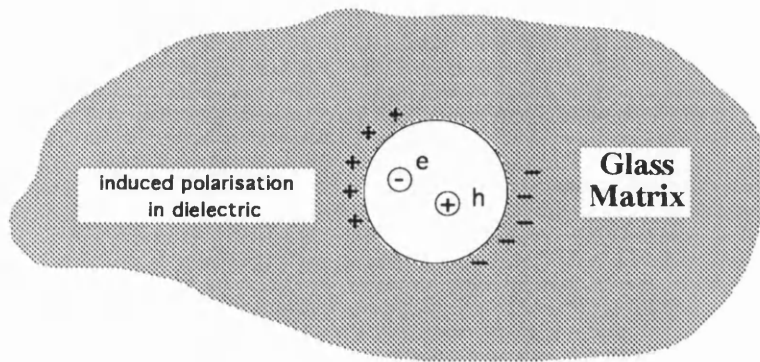
Figure 2.11   Carriers in a crystallite causing a polarisation in the
surrounding dielectric.

Estimates of the magnitude of this contribution can be made by considering the energy
required to move elements of charge from infinity into the crystallite to form the electron or
hole, which for the purpose of this calculation must be given finite radii rather than considered
as point charges [2.26]. This term is significantly less important than the others and is often
neglected. The "wavefunction" obtained using this method represents an envelope function
which modulates the Bloch functions for the corresponding bulk material.

The confining potentials (V_e and V_h) are usually assumed to be infinitely high potential
barriers at the crystallite surface. This approximation will usually be quite reasonable since the
energy gap of $CdSe_xS_{1-x}$ ranges from 1.73eV to 2.42eV (at 300K), while that of silica (the
main constituent of glass) is 9eV [2.27], resulting in extremely deep potential wells (see Figure
2.12, below). Of course, this approximation will become less valid for higher energy states,
where the confinement energies approach the well depth.
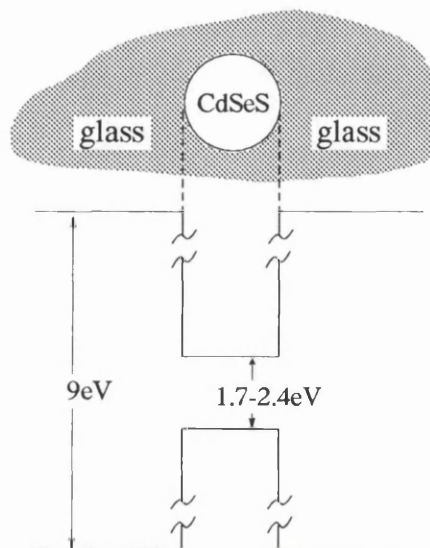
Figure 2.12   Energy band diagram for a CdSeS crystallite
embedded within a silica based glass.

In order to understand the behaviour of confined electrons and holes it is instructive to consider the relative contributions which the first three terms within the Hamiltonian make to the total energy of the system. It can be easily seen that these contributions can be crudely estimated according to the following expressions [2.28,2.29].

$$\text{Kinetic energy of electron} \sim \frac{\hbar^2}{2 m_e^* a^2} \qquad \textbf{(a)}$$

$$\text{Kinetic energy of hole} \sim \frac{\hbar^2}{2 m_h^* a^2} \qquad \textbf{(b)} \qquad \textbf{Equations 2.8}$$

$$\text{Energy associated}$$
$$\text{with Coulomb interaction} \sim \frac{e^2}{\varkappa\, a} = \frac{e^2}{4 \pi\, \varepsilon\, a} \qquad \textbf{(c)}$$

where a = Crystallite radius
m_e^*, m_h^* = Effective masses of electrons and holes
$\varkappa$ = Dielectric constant of crystallite
ε = Permittivity of crystallite
$\hbar$ = (Planck's constant)/2π
e = Electronic charge

From the above, it is evident that for very small crystallites the kinetic energies for the electron and hole will be much larger than the Coulomb interaction energy. For such crystallites the electron and hole will behave essentially independently and no exciton type structure will exist [2.30]. This condition applies when the crystallite radius "a" is such that a<<a_e,a_h, where a_e and a_h are the Bohr radii for the electron and hole respectively, which are defined by:-

$$a_h = \frac{4 \pi\, \varepsilon\, \hbar^2}{m_h^* e^2} \qquad \textbf{(a)}$$
$$\qquad\qquad\qquad\qquad \textbf{Equations 2.9}$$
$$a_e = \frac{4 \pi\, \varepsilon\, \hbar^2}{m_e^* e^2} \qquad \textbf{(b)}$$

where a_e = Bohr radius of electron
a_h = Bohr radius of hole
All other symbols are as defined above

Since a_h is often significantly smaller than a_e (ie m_e^*<m_h^*), three reasonably distinct situations can occur (see, for example, [2.28,2.29]):-
  (i) a<<a_e,a_h
  (ii) a_h<<a<<a_e
  (iii) a_e,a_h<<a
These three situations are briefly discussed below.

(i) a<<a_e,a_h

In this case, as mentioned above, the Coulomb energy of the electron hole pair is negligible

compared with the kinetic energy terms. In this situation the electron and hole will largely behave as independent particles, confined within an infinitely deep potential well, with envelope functions given by solutions of Schrödinger's equation (see the Hamiltonian of Equation 2.7 and Equation 2.10, below).

$$\Psi(r) \propto Y_{lm}(\theta,\phi)\frac{J_{l+1/2}(k_{ln}\,r)}{\sqrt{r}} \quad \text{(a)}$$

Equations 2.10

$$E_{lmn} = \frac{\hbar^2 k_{ln}^2}{2\,m^*} \quad \text{(b)}$$

where Y = Spherical harmonics
     J = Cylindrical Bessel function
     n = 1,2,...
   l, m = 0,1,2,...
   r, θ, ϕ = Spherical co-ordinates
    E_{lmn} = Energy of state labelled with numbers l, m, n
    m^* = Effective mass of confined particle

With boundary conditions requiring the envelope function to vanish on the crystallite surface the confinement energies of the carriers are given by:-

$$E_{lmn} = \frac{\hbar^2 \varphi_{ln}^2}{2\,m^* a^2} \quad \text{Equation 2.11}$$

φ = Zeros of Bessel function
All other symbols are as defined above

With the electron and hole independently confined the effective "energy gap" between the highest hole state and the lowest electron state is given by Equation 2.12.

$$\hbar\omega = E_g + \frac{\hbar^2 \pi^2}{2\,m_e^2 a^2} + \frac{\hbar^2 \pi^2}{2\,m_h^2 a^2} = E_g + \frac{\hbar^2 \pi^2}{2\,\mu\,a^2} \quad \text{Equation 2.12}$$

where $\hbar\omega$ = Effective energy gap of crystallite
     μ = Reduced mass of electron and hole
    E_g = Bulk energy gap of semiconductor
All other parameters are as defined above

(ii) $a_h \ll a \ll a_e$

For crystallites within this size regime the electron is confined as in case (i), above, with its energy shifted upwards according to Equation 2.11. However, the hole's kinetic energy is comparable with the Coulomb energy and, consequently, can not be considered as an independent particle. Since the electron has significantly more kinetic energy than the hole, the

hole can be considered to move in an average potential created by the faster moving electron (this is sometimes referred to as an "adiabatic approximation"). This average potential created by the electron is given by the energy associated with Coulomb interaction between the hole and the electron's charge density, described by its wavefunction (see Equation 2.10(a)). This is given by Equation 2.13, below [2.28,2.31].

$$V(r_h) = -e^2 \int_{Volume} \frac{|\Psi_e(r_e)|^2}{\varkappa|r_e - r_h|} \, d\tau_e \quad \textbf{Equation 2.13}$$

where V = Potential seen by hole due to electron
Ψ_e = Electron's wavefunction
$d\tau_e$ = Element of volume
All other symbols are as defined above

This potential, along with the confining potential of the crystallite itself, can then be used to calculate the energy levels of the holes. This is illustrated schematically in Figure 2.13, below.
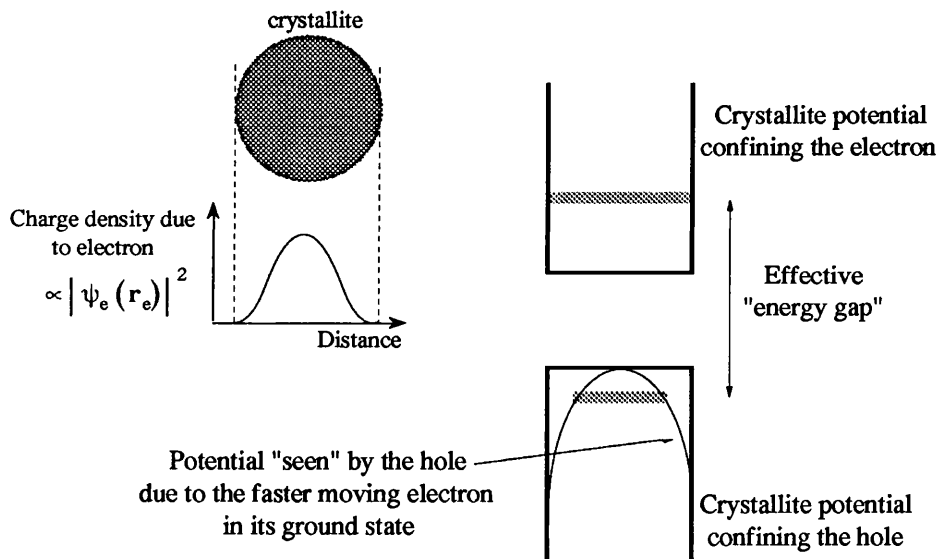
Figure 2.13   Hole moving in the adiabatic potential of an electron in its lowest energy state.

The electron's energy shift is greater than that of the hole and largely accounts for the "blue shift" observed in these crystallites. However, fine structure associated with a hole moving in the adiabatic potential of an electron in its lowest energy bound state has been identified in the absorption edge of CdS crystallites by Ekimov et al [2.31].

(iii) $a_e, a_h << a$

In this situation the exciton radius $a_{ex} = a_e + a_h$ is considerably smaller than the crystallite size and the exciton as a whole experiences confinement within an infinitely deep, spherical

potential well. The envelope function of this confined exciton is given by Equation 2.10(a) in case (i), however, the relevant particle mass is now the total mass of the exciton. The effective "energy gap" is then given by:-

$$\hbar\omega = E_g - E_{ex} + \frac{\hbar^2\pi^2}{2Ma^2} \qquad \textbf{Equation 2.14}$$

where E_{ex} = Exciton binding energy
M = Mass of exciton
All other symbols are as defined above

This equation assumes the exciton binding energy and its internal structure to be unaffected by the finite size of the crystallite. Although it might be expected that a reduced crystallite size would force the electron and hole closer together, increasing E_{ex} and producing a "red-shift" in the energy gap, the exciton confinement effect (a "blue-shift") appears to be more dominant in some cases. Experimentally such exciton confinement has been observed for CuCl crystallites [2.32].

It should be mentioned that the above equations strictly apply only when all the crystallites are the same size. The effect of a size distribution is to introduce a numerical factor into the energy shifts associated with the finite size effects, so, for example, Equation 2.12 would become:-

$$\hbar\omega = E_g + K\frac{\hbar^2\pi^2}{2\mu\bar{a}^2} \qquad \textbf{Equation 2.15}$$

where K = Constant dependent upon the form of
the crystallite size distribution function
All other symbols are as defined above

This equation corresponds to the energy gap between the peaks of the energy level distribution functions for the lowest electron and hole states. It is not a simple matter of replacing "a" in Equation 2.12 by the average crystallite radius. The numerical factor arises because the peak of the size distribution function need not necessarily occur at the mean radius position (see Figure 2.14, below).
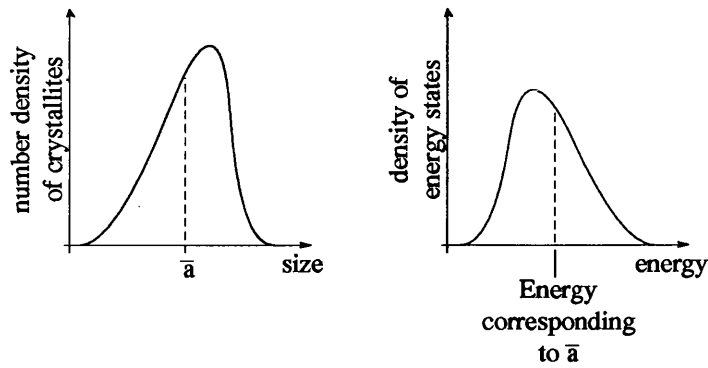
Figure 2.14 Effect of a size distribution on the "blue-shift".

The size distribution function predicted theoretically by Lifshitz and Slezov for particles formed by diffusive growth from a "supersaturated solid solution" results in a value for K of 0.71 (microcrystallite doped glass is such a system, see chapter three and [2.33]). This theoretical distribution function is asymmetric towards lower radii with the peak position occurring at a size greater than the mean crystallite radius (see for example Figure 2.14 and Figure 3.6 in chapter three). Consequently the peak of the energy level distribution function occurs at a lower energy than that corresponding to the mean crystallite radius. As a result of this, the "blue-shift" determined by, for example, measuring the position of a peak in an absorption spectrum associated with carrier confinement, can be smaller than that expected from knowledge of the mean crystallite radius alone.

The system of interest in this thesis is $CdSe_xS_{1-x}$ doped glass with crystallite sizes ranging from 1.5nm upwards. For this semiconductor the Bohr radii are:-

$$a_e(CdS) = 2.35nm \qquad a_e(CdSe) = 4.32nm$$
$$a_h(CdS) = 0.67nm \qquad a_h(CdSe) = 1.40nm$$
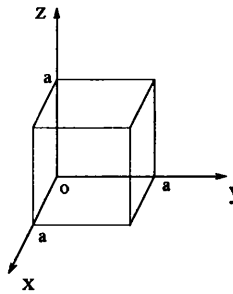
Thus, for the smaller crystallites studied in this thesis, case (ii) would represent the most appropriate of the approximations discussed, with the energy gap shift being largely determined by the electron's confinement energy.

Theorists have extended the above models to include effects such as non-parabolic and non-degenerate valence bands and spin-orbit splitting [2.34]. Also variational [2.35] and Monte Carlo [2.36] methods have been used by some researchers to model the energy levels of quantum dot systems.

2.3.2 Density of States

In this section, in order to illustrate diagrammatically the properties of quantum dots compared with bulk materials, a simplified version of the models discussed above will be used to calculate the density of states for microcrystallites. Consider a particle confined by infinite potential barriers within a cube of side length "a"; its energy levels will be given by Equation

2.16, below [2.37].

$$E_{n_x, n_y, n_z} = (n_x^2 + n_y^2 + n_z^2) \frac{\hbar^2 \pi^2}{2 m^* a^2}$$ **Equation 2.16**

where E = Energy of state (above the bulk energy gap)
n_x, n_y, n_z = 1,2,...

Figure 2.15 Particle confined within a quantum cube.

The density of states for this particle, neglecting all broadening effects, will be given by Equation 2.17, below.

$$D(E, a) \propto \sum_{n_x, n_y, n_z} \delta \left(E - E_{n_x, n_y, n_z} \right)$$ **Equation 2.17**

where D(E,a) = Density of states for a cube
of side "a"
δ = Dirac delta function

This density of states function, for a real system, will experience broadening. In this model it will be assumed that any experiment performed measures the properties of a large number of cubes and that the dominant broadening mechanism results from the size distribution of the "quantum cubes". Thus, the overall density of states for this collection of cubes will be given by Equation 2.18 [2.38].

$$D(E) \propto \int_a D(E, a) N(a) \, da$$ **Equation 2.18**

where D(E) = Overall density of states
N(a) da = Number of cubes with sizes in the range a - a+da

The size distribution function was chosen to be a Gaussian of width determined by the parameter Δa (see Equation 2.19).

$$N(a) \propto \exp\left[-\left(\frac{a - \bar{a}}{\Delta a} \right)^2 \right]$$ **Equation 2.19**

where $\bar{a}$ ≈ Average cube size
Δa = Size distribution parameter

Using this distribution function in Equation 2.18 gives:-

26

$$D(E) \propto \sum_{n_x n_y n_z} \frac{n}{m^{1/2} E^{3/2}} \exp\left(-\frac{\hbar\pi}{\Delta a} \sqrt{\frac{n^2}{2m^*E}}\right) \qquad \textbf{Equation 2.20}$$

$$\text{where} \quad n^2 = n_x^2 + n_y^2 + n_z^2$$

The sum in Equation 2.20 has been evaluated numerically for different values of mean cube size, size distribution parameter and particle mass. The calculations were performed using a computer program written in Turbo Pascal 3 and executed on an Opus Technology PCIV. These density of states functions are illustrated in Figures 2.16, 2.17, 2.18 and 2.19. Figure 2.16 has been calculated for a particle mass of $0.13m_0$ (m_0 is the free electron mass) corresponding to the effective mass of an electron in CdSe.
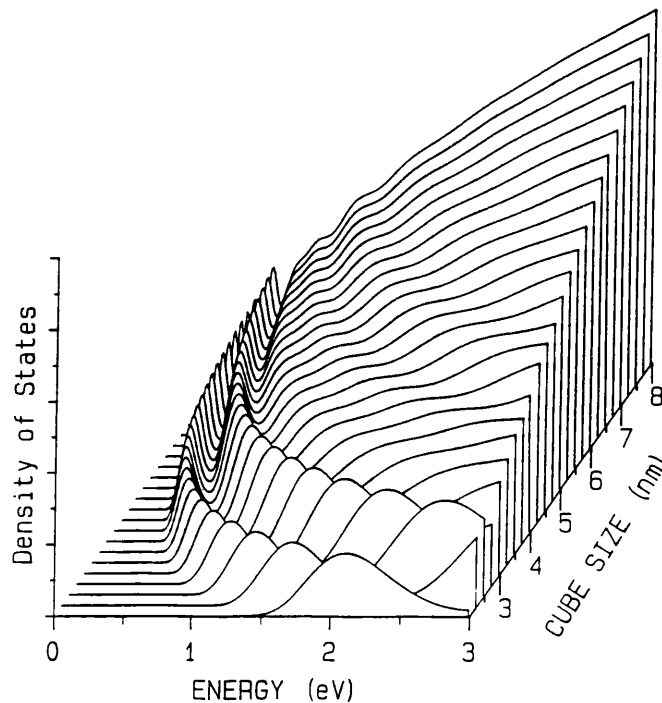
Figure 2.16 Density of states as a function of quantum dot size for $m^*=0.13m_0$ (corresponding to electrons in CdSe) and a size distribution of 20%.

This figure illustrates the density of states as a function of energy for mean cube sizes ranging from 2nm to 8nm, with a size distribution equal to 20% of the mean (measured between the 1/e points on the distribution function, Equation 2.19). The energy scale shows the shift in the particle's energy compared with bulk material. The figure clearly illustrates structure associated with the three dimensional confinement of the particle and the manner in which the broadened energy states become closer together and merge into a bulk-like continuum as the quantum boxes become larger.

Figure 2.17 is calculated for a particle mass of $0.13m_0$, again corresponding to the effective mass of an electron in CdSe.
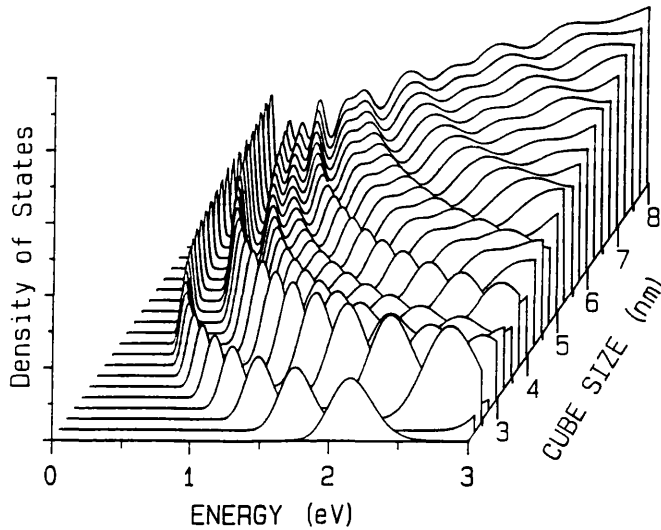
Figure 2.17 Density of states as a function of quantum dot size for $m^*=0.13m_o$ (corresponding to electrons in CdSe) and a size distribution of 10%.

This figure illustrates the density of states for the same effective mass and mean cube sizes as Figure 2.16, but with the size distribution reduced to 10% of the mean. The broadening of the energy states is significantly reduced and considerable structure is evident up to greater mean sizes than in Figure 2.16.

Figure 2.18 show the density of states for a particle with an effective mass of $0.2m_o$, corresponding to an electron in CdS. The mean sizes and size distributions are identical to those of Figure 2.16.
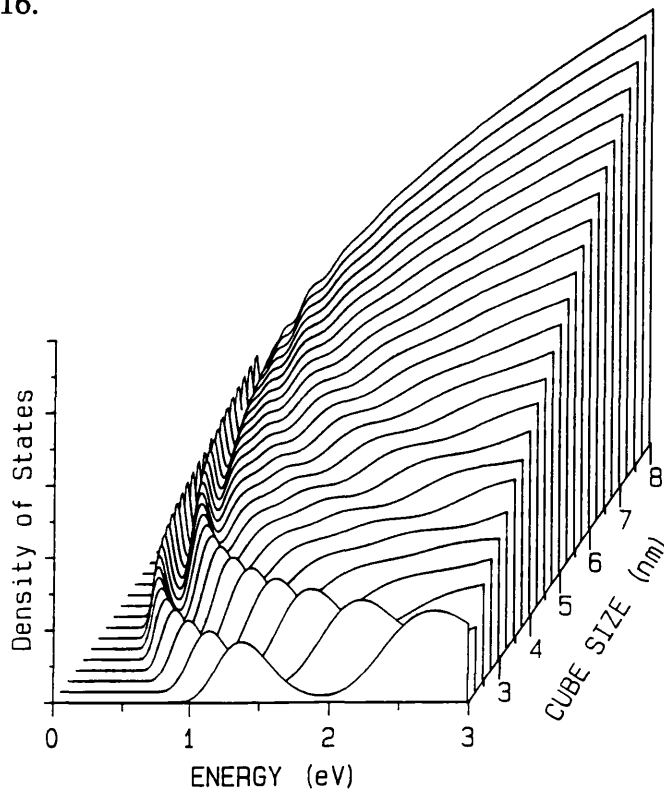
Figure 2.18 Density of states as a function of quantum dot size for $m^*=0.2m_o$ (corresponding to electrons in CdS) and a size distribution of 20%.

28

A comparison of Figures 2.16 (m*=0.13m$_0$) and 2.18 (m*=0.2m$_0$) illustrates the effect of a reduced effective mass in making zero dimensional effects more pronounced and, therefore, easier to observe experimentally. For this reason some researchers studying zero dimensional effects have preferred to work with semiconductors which have a small effective mass (see references [2.39,2.40], for example, where InGaAs/InP systems were chosen in preference to GaAs/AlGaAs systems).

Figure 2.19 shows the variation of the density of states, for a fixed mass and mean cube size, as the width of the size distribution function is varied.
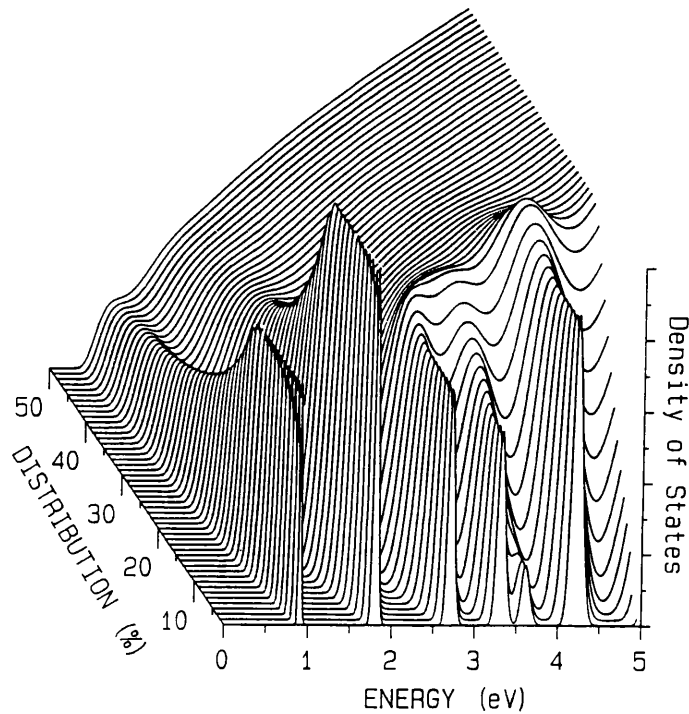
Figure 2.19   Density of states as a function of quantum dot
size distribution for m*=0.13m$_0$ and ā=4nm.

It can be seen that, as the size distribution is increased, the density of states becomes less like the sum of delta functions predicted by the idealised model (see Figure 2.8) and begins to resembles a bulk continuum (a parabolic function).

Although this model is in many respects unrealistic, it illustrates several of the factors which determine the properties of an idealised quantum dot system, such the average dot size, the size distribution of the dots and the effective mass of the carriers. Many of the expected effects which prompted researchers to study quantum dots arise directly from the more discrete-like features in the density of states function.

It is interesting to note that this model makes the same assumptions as those used to predict the density of states for three, two and one dimensional systems (see Equations 2.6). In fact, if one, two or all three of the dimensions of the cuboid in this model are allowed to become very large the resulting density of states will tend towards those given in Equations 2.6. Miller et al

[2.41] have used such an approach, incorporating a linear term within the Hamiltonian in order to model an electric field, to study electro-absorption effects in low dimensional systems.

2.3.3 Electro-absorption in Quantum Dots

It is not difficult to see why quantum dots might be expected to possess enhanced electro-absorption properties relative to the corresponding bulk material. Consider a device containing quantum dots possessing the idealised density of states depicted in Figure 2.8. Such a device would possess an absorption spectrum composed of truly discrete lines. Now consider perfectly monochromatic light, whose wavelength corresponds to one of the device's discrete absorption lines, entering the device. This light, for a sufficiently long device, will be totally absorbed in this idealised example. However, if the position of the device's discrete absorption line were shifted, no matter how slightly, by the application of an electric field the device would be switched to a totally transmitting state. The discrete nature of the device's absorption results in a perfect optical switching device even if the energy level shift per unit field is extremely small. Obviously, any broadening of the energy levels within the device will result in a degradation of its performance, with the electric field induced absorption change being dependent upon both the sharpness of the absorption feature and the energy by which it is shifted due to the applied field.

The amount by which an energy level is shifted by the application of an electric field can be modelled by including within the Hamiltonian (see equation 2.7) a term such as $\pm eFz$ (e=electronic charge, F=applied field, z=co-ordinate along the axis of the field), with the sign being dependent upon the polarity of the particle (ie whether it is an electron or a hole). The magnitude of the energy associated with this term is $\sim eFa$ (a=crystallite size). Thus, the magnitude of an electric field induced energy level shift would be expected to decrease as the crystallite size is reduced. This, together with considerable broadening (due to a size distribution, for example) could conceivably result in the electro-absorption properties of a quantum dot system being inferior to those of the corresponding bulk material. Miller et al [2.41], among others [2.42], have modelled the electro-absorption properties of quantum dots and, with their chosen degree of broadening, predict considerable enhancement of electro-absorption in quasi-zero dimensional systems. Experimental measurements of the electric field induced absorption change in $CdSe_xS_{1-x}$ microcrystallite doped glass have been carried out by a number of researchers without any great enhancement compared with bulk material being observed [2.42,2.43]. However, this experimental technique, of modulating the energy levels by the application of an alternating field, has proved useful in determining the energy levels within crystallites [2.44,2.45].

2.3.4 Nonlinear Optical Properties of Crystallites

The nonlinear optical properties of microcrystallites and small particles embedded within a dielectric host have been investigated theoretically by a number of authors. A method by which such composite materials may show enhanced nonlinear optical properties arises from a dielectric effect, unrelated to any modification of the structure's electronic levels associated with its finite size (see Figure 2.20, below).

Nonlinear particle embedded
within a linear host material

ε_h = Permittivity of host material

ε_p = Permittivity of embedded particle
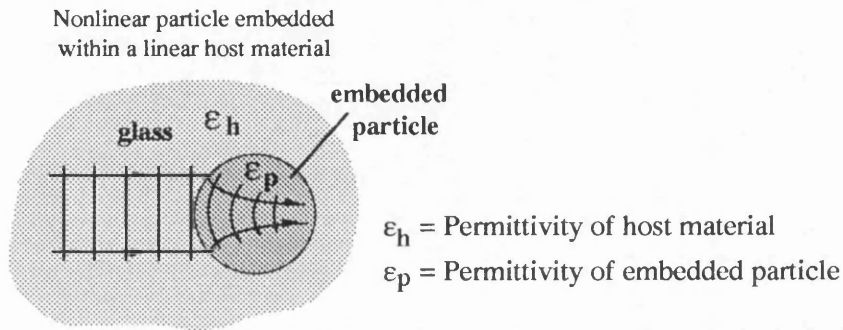
Figure 2.20   Light focused in an embedded particle.

The focusing of the light within the embedded particle produces a considerably higher intensity in the nonlinear material of which the particle is composed than would otherwise be the case in a bulk piece of the same nonlinear material. This increased intensity results in an enhanced nonlinear optical response. Of course, this effect relies upon the dielectric constant of the embedded particle being larger than that of the host material. This condition is satisfied for a semiconductor particle ($\varepsilon_r \sim 10\text{-}15$) embedded within a silica glass host ($\varepsilon_r \sim 2\text{-}4$). The effect does not depend upon the host material being nonlinear or the embedded particle being small enough to illustrate quantum confinement.

The modification of the density of states due to a quantum dot's finite size might also be expected to result in an enhancement of its nonlinear optical properties by several mechanisms. The nonresonant nonlinearity of such a system might be expected to be enhanced for essentially the same reasons discussed above for electro-absorption. In the case of the system's nonlinear optical properties the field modulating the structure's energy levels is provided by the light itself, with modulation of the energy levels resulting in a modulation of the system's refractive index. The discrete energy levels of quantum dots would result in an enhanced refractive index change at certain wavelengths for the same reasons that they result in enhanced electro-absorption (the induced refractive index change is related to the induced absorption change via the Kramers-Kronig relations). Such effects may have application in the fields of optical bistability and optical switching. Again any broadening of the energy levels of such a system would result in a degradation of the effect.

Another nonlinear optical effect possibly enhanced by three dimensional confinement, and of particular relevance to results presented in chapter five, is band (or state) filling. If a material is

strongly optically pumped at an absorbing wavelength the energy levels associated with the absorption can become filled, thus blocking further transitions to these energy levels by the exclusion principle. This results in a saturation of the material's absorption properties. At any given wavelength the absorption will be associated with the energy levels corresponding to the transition and with broadened adjacent energy levels, all of which need to be filled to completely saturate the absorption. In a quasi-zero dimensional system the energy levels of the confined particles are sufficiently separated that only the discrete energy levels associated with a single transition energy need be filled. It would therefore be expected that the absorption of quantum dots would saturate at a lower intensity than that of the corresponding bulk material. There are, however, some physical reasons why state filling nonlinearities might be expected to be reduced by three dimensional quantum confinement. If, for example, the recombination lifetime in quantum dots was significantly shorter than that in bulk material, due to an increased overlap of the electron and hole wavefunctions, state filling would be difficult and the resulting nonlinearity would be reduced rather than enhanced. Neglected in this idealised discussion is the possibility that the process which produces the quantum dot might introduce impurity, defect or surface states which could drastically change the lifetime and recombination dynamics of carriers within such zero dimensional systems (this will be discussed further in chapter five). The various mechanisms underlying nonlinear optical behaviour in quantum dots have been studied extensively by theorists [2.46-2.52].

2.3.5 Laser Action in Quantum Dots

Another theoretically predicted property of quantum dots which is of great technological importance is their enhanced ability to produce laser radiation, compared with bulk material. Again this enhancement largely derives from the more discrete nature of the density of states in zero dimensional systems. In bulk, two dimensional or one dimensional material there is a continuum of energy states in which a population inversion must be created, even though only a very small part of this continuum is involved in the transitions emitting the near monochromatic laser radiation. It would obviously be more efficient, and result in a lower lasing threshold, if it were possible to create a population inversion only between those states involved in laser emission. The nature of the energy states within quantum dots allows this to be done, with only the near discrete states involved in the emission of light being pumped. The properties of such devices have been investigated theoretically by a number of researchers [2.53-2.55].

2.3.6 Surface Phonons in Microcrystallites

The surface modes for a sphere have been calculated by Ruppin et al [2.20] and for pure phonon modes, as opposed to polariton modes, their frequencies are given by ω_n in Equation 2.21.

$$\frac{\omega_n^2}{\omega_T^2} = \frac{\varepsilon_o + \varepsilon_m (n + 1)/n}{\varepsilon_\infty + \varepsilon_m (n + 1)/n}$$ **Equation 2.21**

where ω_n = Surface mode frequency
n = 1,2,...
ω_T = Frequency of TO phonon
ε_o = Low frequency permittivity of crystallite
ε_∞ = High frequency permittivity of crystallite
ε_m = Permittivity of surrounding dielectric

The n=1 mode corresponds to a vibration with a constant amplitude over the whole volume of the sphere, including its surface. Higher order modes decrease in amplitude as r^{1-n} with increasing distance from the surface and are localised around the surface of the sphere. These surface modes have frequencies which lie between the transverse optical and longitudinal optical phonon frequencies. Experimental evidence for the existence of surface mode behaviour has been gathered in a number of different systems such as polycrystalline films [2.56] and etched GaAs cylinders [2.57]. Zhou et al [2.58] observed a shoulder on the low frequency side of the LO phonon peak in CdS and $CdSe_xS_{1-x}$ crystallites, which they attribute to such surface modes (see Figure 2.21).
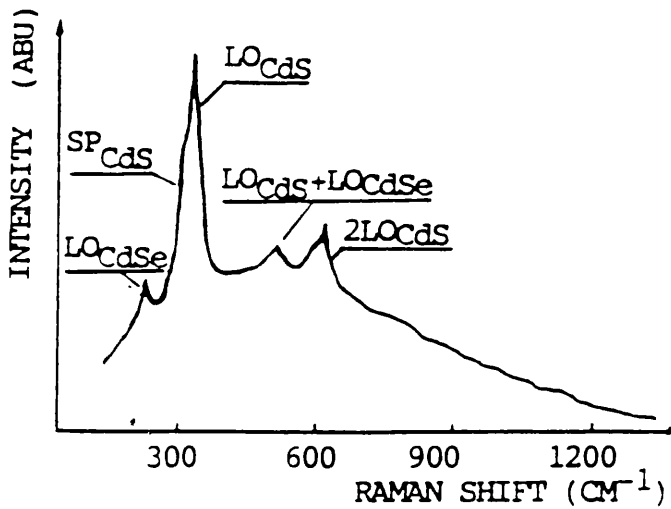
Figure 2.21   Surface mode behaviour in CdS crystallites.
SP is the surface mode [2.58].

As will be discussed in Section 2.4.4 and chapter five the existence of such surface modes has relevance to the interpretation of some of the spectra presented in this thesis.

2.4 Phonon Confinement in Microcrystallites

The theory outlined in this section is similar to that of a number of researchers (see the

references cited below) who have applied it with success to systems such as silicon crystallites prepared in polycrystalline films. In this section the theory will be applied to the $CdSe_xS_{1-x}$ system and a crystallite size distribution will be incorporated into the model.

2.4.1 Theory

A phonon confined within a microcrystallite is not characterised by a single wavevector within the first Brillouin zone, instead it contains a range of wavevectors determined by the function chosen to represent its spatial confinement. A bulk phonon of wavevector q_o would be described by a function of the form given in Equation 2.22 [2.59].

$$\Psi(q_o, r) = u(q_o, r) e^{j q_o \cdot r} \qquad \textbf{Equation 2.22}$$

where r = Position in space
q_o = Wavevector
u = Function with the same periodicity as the lattice

As for the case of electrons confined within a microstructure, Equation 2.22 is multiplied by an envelope function in order to localise the phonon in space, giving an equation of the form [2.59-2.61]:-

$$\Psi(q_o, r) = W(r) u(q_o, r) e^{j q_o \cdot r} = \Psi'(q_o, r) u(q_o, r) \qquad \textbf{Equation 2.23}$$

where W = Envelope function
Ψ' = Function replacing plane wave in Equation 2.22
All other symbols are as defined above

Possible forms of the envelope function, W, for spherical crystallites of radii "a" which have been used within models include [2.59,2.62]:-

$$W(r) = \frac{\sin(\alpha r)}{\alpha r} \qquad \textbf{(a)}$$

$$W(r) = \exp\left[-\frac{\alpha r}{a}\right] \qquad \textbf{(b)} \qquad \textbf{Equations 2.24}$$

$$W(r) = \exp\left[-\left(\frac{\alpha r}{a}\right)^2\right] \qquad \textbf{(c)}$$

The first of these functions is chosen by analogy with the ground state of an electron in an infinitely deep, spherical potential well (see Equation 2.10(a) with l=1,....), with α chosen to give an amplitude of zero at the crystallite surface (ie $\alpha=\pi/a$). In this discussion the Gaussian function (Equation 2.24(c)) will be used. Campbell [2.59] found this form of the envelope

function, with $\alpha=2\pi^2$, to give the best agreement with experimental results for thin silicon films and microcrystalline material created by ion implanting GaAs. This choice of α corresponds to extremely rigid confinement of the phonon within the crystallite. The notation used in this section has been chosen for greatest consistency with other parts of this thesis and differs slightly from that used in some of the references. Hence some expressions and the numerical value for α differ as a result.

For all the calculations performed in this thesis $\alpha=2\pi^2$ will be adopted rather than considering it as an adjusted parameter. This assumes that the phonon confinement conditions in microcrystallite doped glass resemble those studied in the systems for which $\alpha=2\pi^2$ was determined to give the best agreement with the experiments reported by the above researchers.

In order to determine the range of wavevectors possessed by the confined phonon it is necessary to express Ψ' in Equation 2.23 as a Fourier "sum" of "bulk-like" phonons.

$$\Psi'(q_o, r) = \int_q C(q_o, q) e^{j q \cdot r} d^3q \qquad \textbf{Equation 2.25}$$

where $C(q_o, q)$ = Fourier components

For a confinement function of the form given by Equation 2.24(c) (with $\alpha=2\pi^2$) the intensity of each Fourier component is approximately given by Equation 2.26, below.

$$|C(0, q)|^2 \approx \exp\left[-\left(\frac{qa}{2\pi}\right)^2\right] \qquad \textbf{Equation 2.26}$$

In Equation 2.25, q_o has been set equal to zero, since for Raman scattering we are only interested in zone centre phonons (or the nearest phonon to a zone centre phonon which can exist in a finite crystallite). It is assumed that each "bulk-like" phonon present in Equation 2.23 will scatter light to produce a Lorentzian spectrum. The total scattered light is then given by the sum of the Lorentzians produced by each wavevector present in Equation 2.23, weighted by the intensity of the Fourier component corresponding to that wavevector. This results in Equation 2.27 (see, for example, [2.63]).

$$I(\omega, a) = \int_q \frac{|C(0, q)|^2}{\left((\omega - \omega(q))^2 + (\Gamma_o/2)^2\right)} d^3q \qquad \textbf{Equation 2.27}$$

where $I(\omega,a)$ = Raman scattering intensity from
                crystallites of radius "a" at frequency ω
           $\omega(q)$ = Phonon dispersion relation
           Γ_o = Broadening parameter for Raman scattering spectra
All other parameters are as defined above

Equation 2.27 forms the basis of the following calculations. This equation was simplified by assuming an isotropic phonon dispersion of the form:-

$$\omega(q) = A + B\cos\left(\frac{qc}{\pi}\right)$$ **Equation 2.28**

where $\omega(q)$ = Dispersion relation

A, B = Constants

q = Phonon wavevector

c = Lattice parameter

With the appropriate values of A and B for CdSe being 194cm^{-1} and 12cm^{-1} respectively with c taken to be 0.7nm. These values of A and B are based upon a theoretical phonon dispersion curve for CdS (see Figure 2.22) [2.64,2.65].
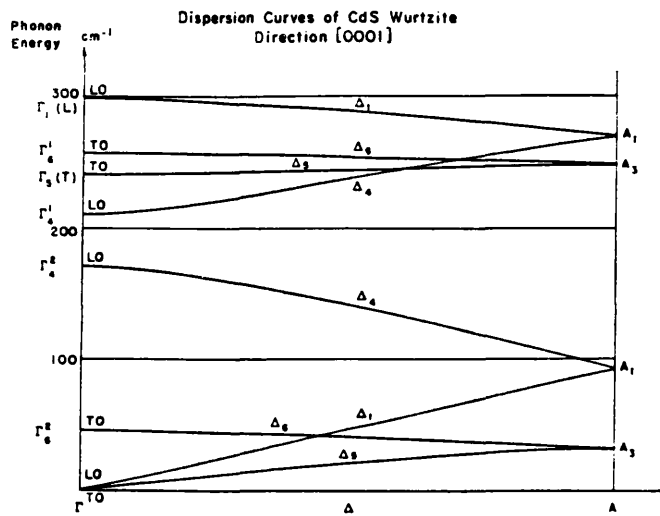
Figure 2.22   Theoretical phonon dispersion curves for CdS [2.65].

The phonon dispersion relation for CdSe is obtained by shifting the theoretical CdS curve towards lower energy to correspond to the zone centre phonons of CdSe [2.64], approximately according to Equation 2.29, below [2.14].

$$\frac{\omega(CdSe)}{\omega(CdS)} = \sqrt{\frac{2\,\omega_{TO}^2(CdSe) + \omega_{LO}^2(CdSe)}{2\,\omega_{TO}^2(CdS) + \omega_{LO}^2(CdS)}}$$ **Equation 2.29**

where ω (CdSe) = Phonon dispersion for CdSe

ω (CdS) = Phonon dispersion for CdS

ω_{LO} (XY) = LO phonon frequency at k=0 for material XY

ω_{TO} (XY) = TO phonon frequency at k=0 for material XY

This is reasonable because of the similarity of the crystal lattices and spring constants in CdSe

36

and hexagonal wurtzite CdS. Experimental measurement of the phonon dispersion curves of Cd containing compounds by neutron scattering is difficult because of the large neutron absorption cross-section of [113]Cd, which is present in natural cadmium. Γ_o was taken to be 7cm^{-1}, based upon the width of the first order Raman scattering peak from zone centre LO phonons in bulk CdSe [2.66]. The assumption of an isotropic dispersion relation allows Equation 2.27 to be simplified to a one dimensional integral.

In order to assess the effect of a crystallite size distribution, the Raman scattering from each size of crystallite within the sample can be "summed" to produce the total scattered intensity (see Equation 2.30, below).

$$I(\omega) = \int_a I(\omega, a) N(a) \, da \qquad \textbf{Equation 2.30}$$

where $I(\omega)$ = Raman scattering intensity from all crystallites
$N(a)$ = Crystallite size distribution function

For the purposes of the following calculations, $N(a)$ was chosen to be a Gaussian of the form given by Equation 2.19. The parameters that can be used to characterise the Raman spectra of microcrystallites are:-

    (i)   Shift from bulk position
    (ii) Broadening of Raman scattering spectra
    (iii) Asymmetry of spectra

These are illustrated in Figure 2.23, below.
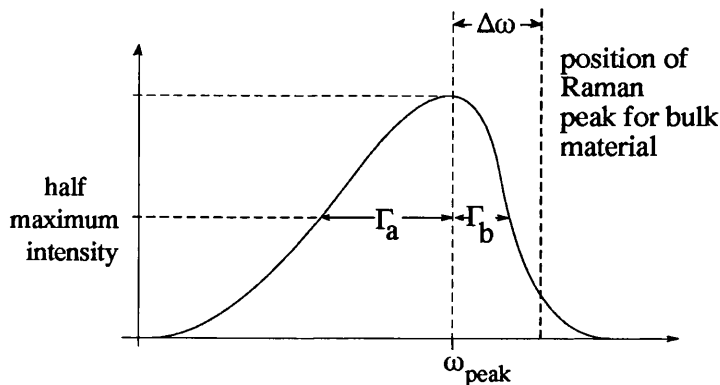
$\Delta\omega$ = Shift from bulk position
Γ_a = Low frequency half width half maximum
Γ_b = High frequency half width half maximum
$\Gamma = \Gamma_a + \Gamma_b$

Figure 2.23   Parameters used to characterise Raman scattering from microcrystallites.

2.4.2 Numerical Calculations

Graphs of $\Delta\omega$, or Γ, versus crystallite radius will be dependent upon the choice of α. Changing α is equivalent to rescaling the radius axis of the graph. However, graphs of $\Delta\omega$ versus Γ are independent of the choice of α and as such are possibly a more appropriate measure of the model's success.

For a given crystallite radius and size distribution Equations 2.27 and 2.30 can be used to calculate numerically a relative intensity Raman scattering spectrum. When calculating $\Delta\omega$ or Γ as functions of crystallite radius (or $\Delta\omega$ as a function of Γ), determining the whole spectrum is inefficient, since only the shift and broadening are required. A numerically more efficient method is now outlined.

To calculate the peak position (and hence $\Delta\omega$) efficiently a region formed between a lower limit ω_{min} and an upper limit ω_{max} is chosen within which the peak is known to lie (the peak will always lie within the range covered by the phonon dispersion curve for the LO phonon). The sign of the derivative $dI/d\omega$ (an expression for which can be derived analytically from Equation 2.27) is then examined at the mid-point of the region. If the derivative is negative then ω_{max} is set equal to the mid-point. If the derivative is positive then ω_{min} is set equal to the mid-point. This is illustrated in Figure 2.24, below.
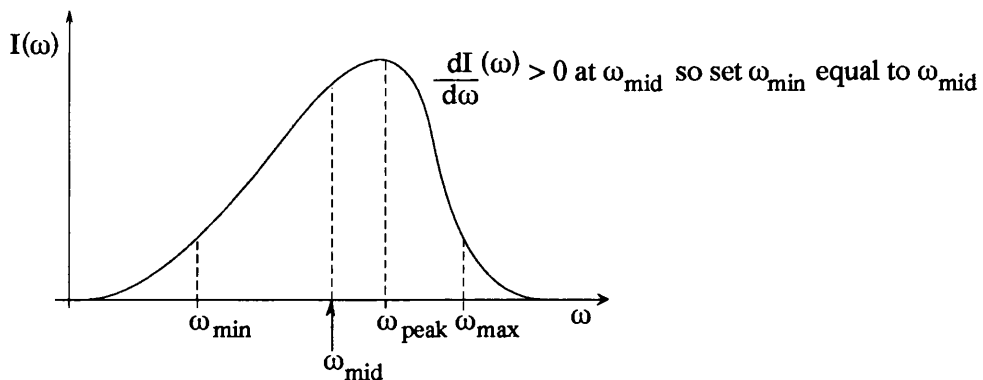
Figure 2.24 Method used to determine the peak position and half height points for a calculated spectrum.

This process is then performed repeatedly, with the range within which the peak is known to lie being halved after each iteration. This process is repeated until the peak position (somewhere between ω_{min} and ω_{max}) is known to the desired accuracy. A similar method can be used to determine Γ_a and Γ_b. In these cases $I(\omega)$ is compared with $I(\omega_{peak})/2$ (ω_{peak} has already been found) to determine whether to set ω_{min} or ω_{max} equal to the mid-point. In determining Γ_a and Γ_b, ω_{peak} forms ω_{min} and ω_{max}, respectively, with the other limit being sufficiently far from ω_{peak} to ensure that the inspected range contains the appropriate half height point. The above process was implemented using a program written in Turbo Pascal 3

running on an Opus Technology PCIV. The results of these calculations will now be discussed.

2.4.3 Theoretical Predictions

This model and the calculations presented will be used in chapter five to analyse experimental Raman spectra from CdSe microcrystallite doped glass. The reasons underlying the choice of CdSe rather than $CdSe_xS_{1-x}$ or CdS for the experimental investigation will be discussed fully in chapter five.

Figure 2.25 illustrates Raman scattering spectra for crystallites of different sizes. It can be seen that the spectra become broader as the crystallite size is reduced reflecting the relaxation of the q≈0 selection rule as the phonons become increasingly spatially confined. There is also a shift in the peak position towards lower wavenumbers which will be illustrated more clearly in subsequent diagrams.
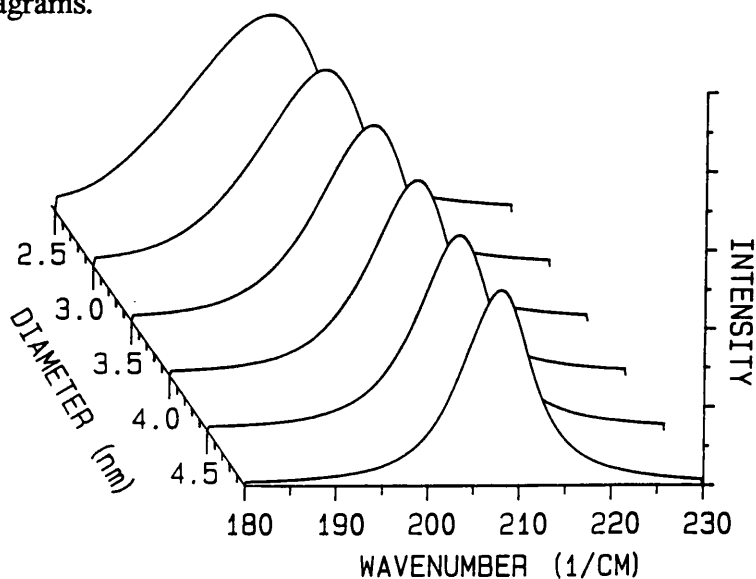
Figure 2.25 Calculated Raman spectra for crystallites of various sizes (assuming a uniform crystallite size).

Figure 2.26 shows the variation of the low frequency shift in the peak position of the Raman scattering spectra and its full width at its half height points as functions of crystallite radius. As the crystallite size is reduced, the q≈0 selection rule is relaxed resulting in an increased linewidth. These non-zone centre LO phonons, which for small crystallites participate in Raman scattering, have a lower energy than the q=0 phonon, resulting in a shift of the Raman peak towards lower energy as the crystallite size is reduced.

(a)   **(b)**
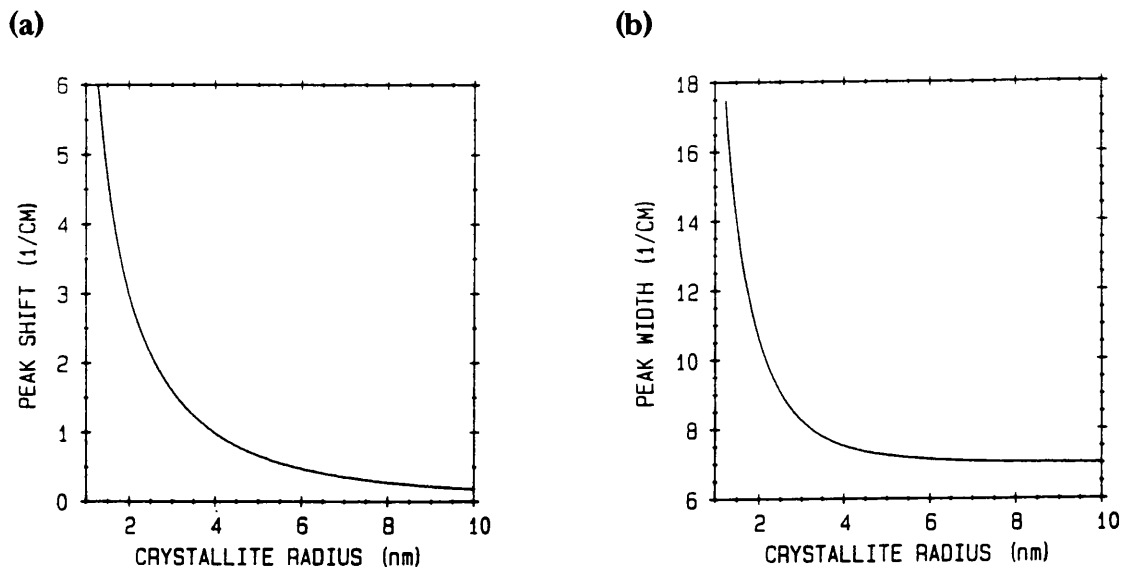
Figure 2.26 **(a)** Raman scattering peak position as a function of
                        crystallite size (uniform crystallite size).
                   (b) Width of Raman scattering peak as a function
                        of crystallite size (uniform crystallite size).

Figure 2.27 illustrates the shift in the phonon peak position as a function of the full width at
half maximum of the peak. This function is independent of the choice of α but does depend
upon the form of the confinement function. The crystallite sizes corresponding to points on the
graph are displayed on the right vertical axis. The sizes on this axis, are of course, dependent
upon the choice of α.
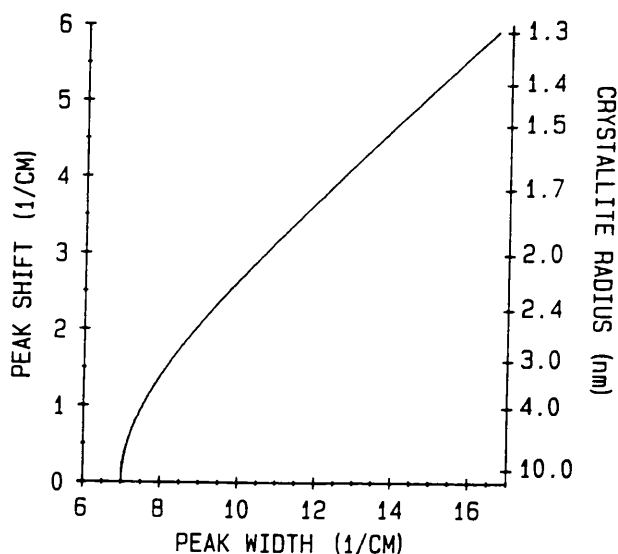
Figure 2.27 Variation of peak position as a function of peak width
                   as the crystallite size is varied (no size distribution).

40

The effects of a crystallite size distribution on the shift and broadening resulting from phonon confinement are illustrated in Figures 2.28 and 2.29. As expected a size distribution results in a broadening of the Raman scattering spectra (see Figure 2.28). Less expected is the effect of a size distribution in producing an increased confinement shift for a given average crystallite size. This can be understood by considering Figure 2.26. The shift in the peak position due to phonon confinement increases much more rapidly for small crystallites than for large crystallites. Hence, crystallites smaller than the mean size will have a larger effect in determining the phonon confinement shift than will crystallites larger than the mean. Also, if the size distribution function is not symmetric (in these calculations it is symmetric), with its peak position not occurring at the mean size, this will introduce a numerical factor into the result (see, for instance, section 2.3.1 and the discussion relating to shifts of the electronic energy states).

(a)   **(b)**
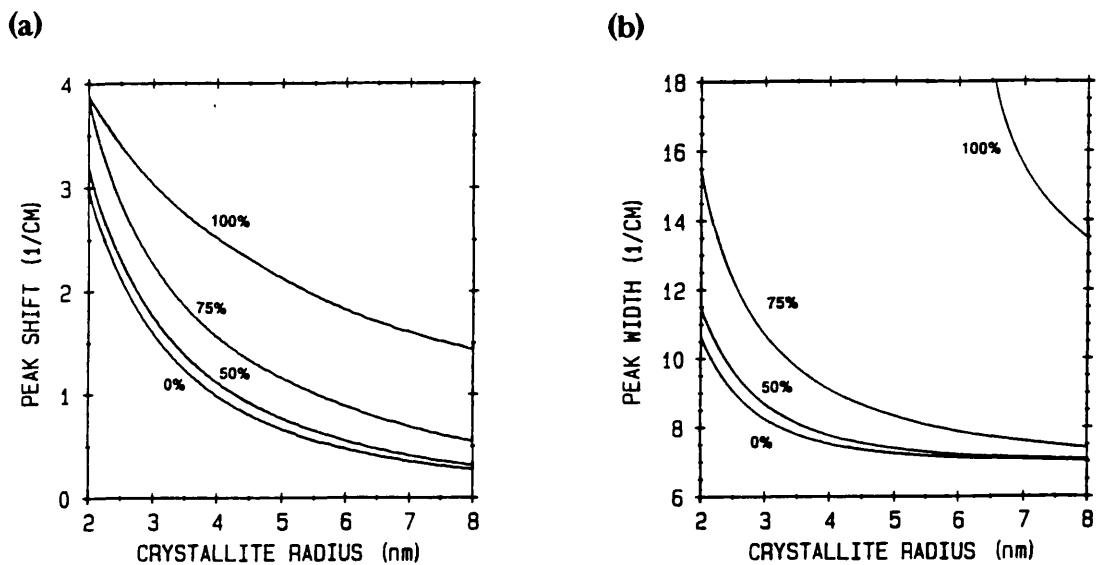
Figure 2.28 The size variations are the full width at half maximum of the distribution function expressed as a percentage of the mean radius.
(a) Peak position as a function of mean crystallite size for various size distributions.
(b) Peak width as a function of mean crystallite size for various size distributions.
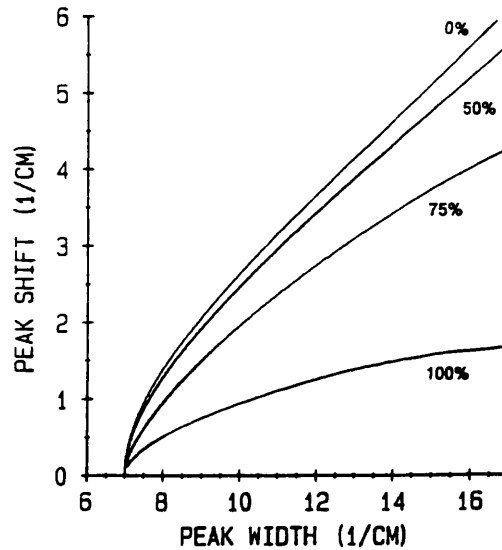
Figure 2.29 Peak position as a function of peak width for
various size distributions.

2.4.4 Comments on the Phonon Confinement Model

The most obvious weakness of this model is the existence of the "adjustable parameter", α. In the above calculations α has not been regarded as an adjusted parameter, but rather a value was adopted which was found by other researchers to produce the "best fit" to their experimental data. This choice of α was based upon measurements in systems very different from semiconductor doped glass (see above and reference [2.59]). However, microcrystallite doped glass, like these other systems, would be expected to exhibit very strong spatial confinement of phonons. The use of this value for α is, therefore, reasonable.

The assumptions regarding the nature of the phonon dispersion characteristics (see Equation 2.28 and Figure 2.22) at first appear to be unrealistic. However, the centre of the Brillouin zone, around q=0, is of greatest importance in determining the Raman scattering spectrum. Hence, the phonon dispersion relation used need only model accurately the actual dispersion characteristics of the semiconductor in this region. This, therefore, should not be regarded as a great failing of the model.

The model does not in any manner attempt to describe the interaction between the confined phonons and the confined electrons within the crystallites. Since scattering of light by phonons occurs via the intermediary of electronic states, a full model should attempt to describe the electron-phonon interaction within quasi-zero dimensional structures. The above model merely assumes any effect upon the Raman spectra to occur because of a simple "uncertainty principle" involving the phonon's wavevector and its spatial confinement. Tu et al [2.67] attempt to include the effect of quantised electronic states in their model.

The model also neglects the effects of surface phonons which might be expected to occur on the low frequency wing of the CdSe LO phonon (see Section 2.3.6). This will be discussed more fully when experimental spectra are compared with this model in chapter five.

Chapter 3 - Sample Preparation

In this chapter the preparation of semiconductor crystallites of controlled size within a glass matrix will be discussed. Initially the production of microcrystallites in a glass matrix will be discussed in a highly qualitative manner, in order to introduce and outline the methods employed in their growth. Subsequent sections will then describe the growth of these crystallites in a more quantitative manner, first by discussing the free energy of a system of crystallites within a glass matrix then by considering diffusion processes within the semiconductor doped glass. References will be given to work dealing with the general problem of particle growth from a highly saturated solution and finally a brief comparison will be made between the predictions of the various models and the measurements of crystallite growth rates and size distributions made by several research groups.

3.1 Growth of Crystallites

3.1.1 Growth of Crystallites - General Principles

Figure 3.1 illustrates in outline the method used by companies such as Corning, Schott and Hoya to prepare commercially available optical filter glass, which usually contains relatively large (10's of nanometres across) crystallites of $CdSe_xS_{1-x}$. The crystallites produced in these commercially available glasses are large, giving a sharp, featureless, "bulk-like" absorption edge, characteristic of long-pass optical filters.

The starting point in the preparation of these materials is a borosilicate glass melt into which is added a few weight percent of compounds containing cadmium, selenium and sulphur. This material is heated for typically several hours at 1450C and then cast by standard glass making techniques. At this stage the glass contains the cadmium, selenium and sulphur in the form of isolated ions. It does not contain crystallites of $CdSe_xS_{1-x}$ and is visibly transparent. The glass is then heated at a temperature typically between 600C and 700C for a time period ranging from several minutes to many hours [3.1,3.2]. During this heating ("striking") stage the mobile Cd, Se and S ions migrate to form small semiconductor crystallites. This process is illustrated schematically in Figure 3.1 (below).

```
                                                                      A few weight
    ┌─────────────────────────┐   ◄▓▓▓▓▓▓▓▓    percent of Cd, Se and S
    │  Borosilicate glass melt │                containing compounds
    └─────────────────────────┘
                 │  Heat at 1450C
                 │  for several hours
                 ▼
    ┌─────────────────────────┐
    │    Clear cast glass      │
    │ containing Cd, Se and S  │
    │  ions in "solid solution"│
    └─────────────────────────┘
                 │  "Striking" stage
                 │  Heat at typically
                 │  600C-700C for several
                 │  minutes to many hours
                 ▼
    ┌─────────────────────────┐   Glass with a colour characteristic
    │   Coloured filter glass  │   of the CdSeS crystallites within
    └─────────────────────────┘   the glass matrix
```
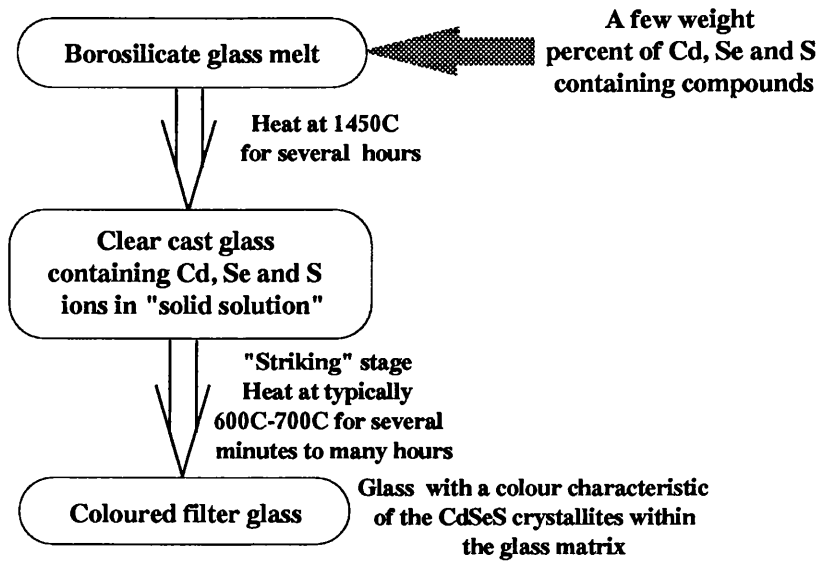
Figure 3.1 Schematic diagram illustrating the production of commercially available filter glasses.

The resulting glass is deeply coloured displaying the characteristic absorption edge of the "bulk-like" $CdSe_xS_{1-x}$ crystallites, which varies from ~490nm to ~700nm as x increases from zero to one. These crystallites are usually large enough to possess a sharp, featureless, essentially "bulk-like" absorption edge. Often the casting and striking stage are combined into one process. For the work described in this thesis the samples were usually not prepared from the basic starting point of an undoped glass melt. Instead commercially available optical filter glass was used as the starting material. This commercially available material, containing relatively large, "bulk-like" crystallites, was then subjected to further processing in order to produce crystallites small enough to display three dimensional confinement effects. The stages of this subsequent processing are illustrated schematically in Figure 3.2.
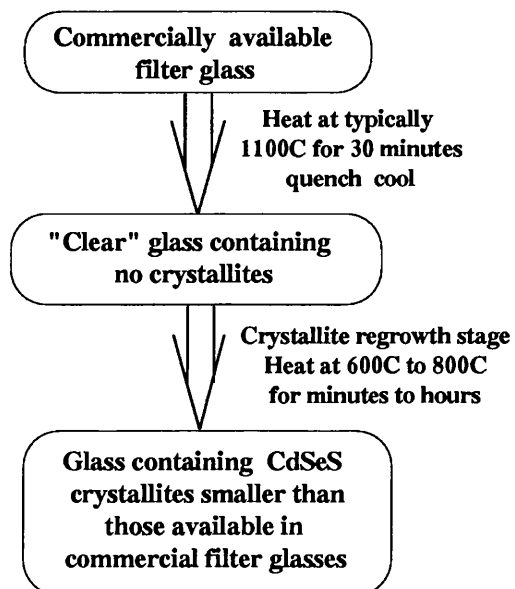
Figure 3.2
Schematic diagram illustrating the experimental preparation of quantum confined crystallites from commercially available filter glass.

```
    ┌─────────────────────────┐
    │  Commercially available  │
    │      filter glass        │
    └─────────────────────────┘
                 │  Heat at typically
                 │  1100C for 30 minutes
                 │  quench cool
                 ▼
    ┌─────────────────────────┐
    │  "Clear" glass containing │
    │     no crystallites       │
    └─────────────────────────┘
                 │  Crystallite regrowth stage
                 │  Heat at 600C to 800C
                 │  for minutes to hours
                 ▼
    ┌─────────────────────────┐
    │  Glass containing CdSeS   │
    │  crystallites smaller than │
    │    those available in      │
    │  commercial filter glasses │
    └─────────────────────────┘
```

The commercial filter glass, containing large crystallites, is heated to between 1100C and 1150C for typically 30 minutes. At these temperatures the solubility of Cd, Se and S in the glass increases and the crystallites within the glass matrix show a greater tendency to disperse into isolated ions. The material then contains no crystallites and is visibly transparent. The glass is then cooled rapidly to room temperature. At room temperature the ions within the material are immobile and are unable to migrate to reform crystallites. The material is thus "frozen" in a cleared condition containing no crystallites. The glass can be regarded as a highly saturated solution of Cd, Se and S within a solid "solvent" which, given the opportunity, will precipitate out small particles of $CdSe_xS_{1-x}$. The glass is then reheated to between 600C and 700C for a time period in order to regrow the crystallites. At these temperatures the Cd, Se and S atoms are mobile and tend to diffuse and cluster to form energetically more favourable microcrystallites. This nucleation and growth of crystallites can also be thought of as the result of the species' (Cd, Se and S) lower solubility at these temperatures, compared with the higher clearing temperatures, causing particles of $CdSe_xS_{1-x}$ to be "precipitated" out of the solid solution. Of course at room temperature the solubility of the species in the glass matrix is even lower, but they have such a low mobility that crystallite precipitation and growth cannot occur over normal time periods. Generally, within the temperature range of crystallite growth, a higher temperature or longer annealing period will result in larger crystallites. The physical origin of the "clearing" effect at 1100C and the crystallite growth in the typical range 600C to 700C will be discussed in the next section.

3.1.2 Growth of Crystallites - An Energy Model

A simple model to describe the formation of crystallites from a supersaturated solid solution will now be considered. Figure 3.3 illustrates the three conditions in which an atom or ion can exist within these samples.

$$\Delta F = -\beta r^3 + \gamma r^2$$

A : Atoms far enough within the volume of the crystallite for them to experience an essentially "bulk-like" potential.

B : Atoms at, or near, the crystallite surface. These have a lower binding energy than atoms within the crystallite's volume.

C : Ions isolated in the solid solution.
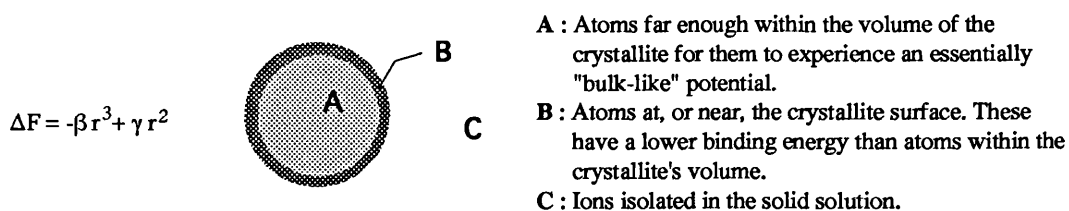
Figure 3.3 Schematic diagram illustrating the three conditions in which an atom can exist within the glass matrix. For an explanation of the equation consult the text.

If all the ions/atoms of the solute (in this case Cd, Se and S) were in state C, corresponding to a "cleared" sample containing no crystallites, then the free energy of the system would be α, say. If some of these ions leave the solid solution to form crystallites then the free energy of the system (in the first approximation) will decrease by an amount proportional to the number of

atoms in the crystallites. The number of atoms in the crystallites is proportional to their volume, which is proportional the cube of their radius (we will assume all the crystallites are the same size and are spherical), therefore the free energy of the system is now:

$$F = \alpha - \beta r^3 \qquad \textbf{Equation 3.1}$$

where   F = Free energy of system (Gibb's function)
      α = Free energy of system containing no crystallites
      β = Proportionality constant
      r = Radius of crystallites

This equation, however, neglects one important point; not all the atoms within the crystallites cause an equal reduction in the free energy of the system. Atoms at the surface are less tightly bound than atoms within the volume of the crystallites and so cause a smaller reduction in the free energy of the system than atoms near the centre of the crystallites. This effect can approximately be accounted for by adding a term to the free energy proportional to the number of atoms at or near the crystallite surface (ie, proportional to the surface area of the crystallites). The change in the free energy between the "cleared" condition and the state where it contains crystallites of radius r is then given by:-

$$\Delta F = -\beta r^3 + \gamma r^2 \qquad \textbf{Equation 3.2}$$

where $\Delta F = F - \alpha$ = Change in free energy during crystallite growth
      γ = Proportionality constant
      All other parameters as in Equation 3.1

At the bulk melting point of the material of which the crystallites are composed any increase in the radius of the crystallites above r=0 will result in an increase in the free energy of the system (this is the reason why the material melts). Therefore, at the bulk melting point of the crystallite material, β must be equal to zero (see Equation 3.2). β will increase as the temperature is reduced below this bulk melting point, allowing the free energy to be plotted as a function of r at various temperatures to give the series of curves shown in Figure 3.4 (see [3.3] or [3.4] for example).
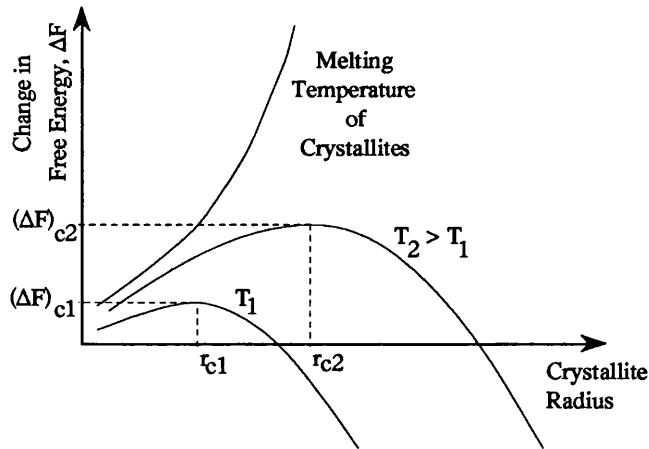
Figure 3.4 Schematic diagram of the variation of the free energy of a system of crystallites in a supersaturated solid solution of their component atoms.

Referring to this figure a number of interesting features can be observed.

(i) For any temperature below the bulk melting point, T_m, (T_1 for example) any crystallite smaller than a critical radius, R_{cr} (eg r_{c1} for $T=T_1$ in Figure 3.4), can only decrease the free energy of the system by becoming smaller. They could also decrease F by growing considerably larger than the critical radius, but this is prevented by an energy barrier, which forms an activation energy too large to be supplied thermally (see later discussion on the initial nucleation of crystallites, section (iii), below). Therefore, crystallites smaller than this critical radius will tend to disperse. If the temperature is raised to a value such that all the crystallites are smaller than the critical radius then all the crystallites within the glass matrix will "melt" into the solid solution. This corresponds to the "clearing" stage described earlier. It should be noted that it is not necessary for the temperature to be higher than the melting point of the corresponding bulk material (in this case $CdSe_xS_{1-x}$), only that the temperature be sufficiently high to ensure that the critical radius exceeds the radii of all the crystallites. Thus, small particles have a lower effective "melting point" than the corresponding bulk material. As an example, commercial filter glass can be "cleared" at 1100C which is lower than the melting point of $CdSe_xS_{1-x}$ (m.p. (CdSe)=1239C and m.p.(CdS)=1477C).

(ii) Crystallites greater in size than the critical radius will increase the free energy of the system by becoming smaller. They can only decrease the free energy by becoming larger and such crystallites will experience growth under these conditions.

(iii) In a supersaturated solid solution containing no crystallites the free energy of the system can only be decreased by first forming crystallites larger than the critical radius, R_{cr}, which will then decrease the free energy of the system by growing larger. In order to spontaneously form

47

crystallites of the critical size it is necessary to overcome an energy "barrier", $(\Delta F)_{cr}$. This activation energy can be thermally supplied, and the probability of this occurring is given by the Boltzmann factor:-

$$\exp\left(\frac{-(\Delta F)_{cr}}{kT}\right) \qquad \textbf{Equation 3.3}$$

where $(\Delta F)_{cr}$ = Activation energy required to spontaneously form a crystallite
of the critical size necessary to ensure its continued growth
k = Boltzmann's constant
T = Absolute temperature

At very low temperatures (ie room temperature) the critical radius, R_{cr}, and the activation energy, $(\Delta F)_{cr}$, are both small, but the Boltzmann factor is also very small and the spontaneous formation of crystallites larger than the critical radius is highly unlikely. Thus, when filter glass has been "cleared" at high temperatures (~1100C) then quenched to room temperature it remains "cleared".

(iv) At temperatures intermediate between room temperature and the "clearing" temperature there exists a crystallite growth regime. In this temperature range the critical radius, and $(\Delta F)_{cr}$, are small enough and the Boltzmann factor sufficiently large for crystallites larger than the critical size to form spontaneously. These crystallites will then continue growing.

From Equation 3.2, R_{cr} and $(\Delta F)_{cr}$ can easily be found to be given by:-

$$R_{cr} = \left(\frac{2\gamma}{3\beta}\right) \qquad \textbf{Equation 3.4}$$

$$\text{and} \quad (\Delta F)_{cr} = \left(\frac{4\gamma^3}{27\beta^2}\right) \qquad \textbf{Equation 3.5}$$

where R_{cr} = Critical radius which must be reached to ensure
continued crystallite growth

It can be seen that $(\Delta F)_{cr}$ and R_{cr} increase with temperature and become infinite at the semiconductor's bulk melting point (β decreases to zero at T_m). Using $(\Delta F)_{cr}$ in the Boltzmann factor gives:-

$$\exp\left(\frac{-4\gamma^3}{27kT\beta^2}\right) \qquad \textbf{Equation 3.6}$$

This has the value zero at T=0 and T=T_m (β=0 at T=T_m) and gives the probability of the formation of a crystallite of the critical size. This probability is shown schematically in Figure 3.5.

Rate of Nucleation of Crystallites of the Critical Size
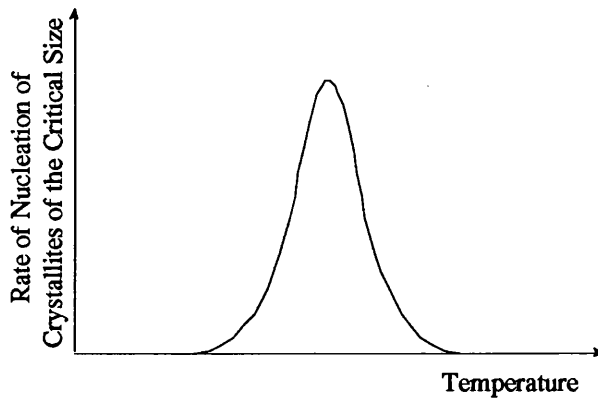
Temperature

Figure 3.5 Schematic diagram illustrating the probability of the available thermal energy causing the spontaneous formation of a crystallite of the critical radius as a function of temperature.

It can be seen that the probability of formation of a crystallite of the critical size will only be large within a relatively narrow range of temperatures. This range corresponds to the crystallite growth regime. Below this temperature range crystallites of the critical size are prevented from forming by the unavailability of thermal energy to overcome the activation energy, $(\Delta F)_{cr}$. This is equivalent to describing the lack of crystallites in terms of the low mobility of Cd, Se and S ions at low temperatures, since if the atoms are immobile they are unlikely to spontaneously form a cluster larger than R_{cr}. Above this temperature range R_{cr} and $(\Delta F)_{cr}$ are so large that even the readily available thermal energy cannot overcome the required activation energy, and crystallites will not nucleate. Since Figure 3.5 represents the probability of a successful nucleation (ie a crystallite larger than R_{cr} forming) it can be taken to represent crudely the density of crystallites formed as a function of temperature. At low temperatures there is a low density of very small crystallites (for a given growth period). As the temperature of nucleation and growth is increased the crystallite density will increase and they will grow more rapidly due to the enhanced mobility of the constituent atoms at these temperatures. At even higher temperatures the crystallites, once larger than the critical radius, would grow very quickly, however the probability of a crystallite of the critical size forming is very small resulting in an extremely low density of crystallites. In summary, examination of this simple model suggests:-

(a) A low nucleation and growth temperature results in a low density of slowly growing crystallites.
(b) An intermediate nucleation and growth temperature results in a higher density of quite rapidly growing crystallites.
(c) A very high nucleation and growth temperature results in rapid growth of the crystallites, however their density will be very small.

If the desired sample has a high density of large crystallites which can be grown over a normal time period (ie less than several weeks) the above discussion might suggest attempting to separate the nucleation and growth stages. This would involve an initial intermediate (case (b) above) temperature annealing to give a high density of "seed crystals" followed by a higher temperature annealing stage during which most of the crystallite growth occurs (case (c) above).

3.1.3 Growth of Crystallites - A Diffusion Model

In this section the growth of crystallites by precipitation from a supersaturated solid solution will be outlined in terms of a model developed by Lifshitz and Slezov [3.5,3.6]. Unlike the previous approach this model describes the growth (or dispersion) of crystallites using the rate of diffusion towards (or away from) a crystallite of radius R.

Suppose that initially there exists points within the glass matrix which act as "sinks" towards which atoms aggregate. This will give a flux of solute towards these nucleation centres given by **J** where:-

$$\nabla \cdot \mathbf{J} = - A \delta(r) - D \nabla^2 C \qquad \textbf{Equation 3.7}$$

where   J = Rate of flow of material (component material of crystallites)
            per unit surface
          A = Constant
          D = Diffusion coefficient
          δ = Delta function
          C = Density of material of which crystallites are composed
            (amount per unit volume)

In the steady state condition (when **J**=0) this results in an equilibrium concentration of solute, at the surface of a crystallite of radius R, of the form:-

$$C_R = C_\infty + \frac{\phi}{R} \qquad \textbf{Equation 3.8}$$

where C_R = Steady state concentration at a radius R from the "sink"
          C_∞ = Concentration at infinity
          ϕ = Constant

(Compare this with the electrostatic potential of a point charge, where the point charge acts as a sink (or source) of electric flux.)

If instead we have a supersaturated solid solution of supersaturation Δ so that the concentration is then $C = C_\infty + \Delta$ there will always be the possibility of crystallite growth as long as the supersaturation exists and an equilibrium will not be reached. If the actual concentration of the supersaturated solid solution ($C_\infty + \Delta$) exceeds the equilibrium value at the crystallite surface ($C_\infty + \phi/R$) then the crystallite will "attempt" to decrease the concentration at its surface

by absorbing material and growth will occur. If, however, the actual concentration is less than the equilibrium value the crystallite will attempt to increase the concentration at its surface by ejecting material, and will decrease in size. Crystallites which are small enough will attempt to reach a large equilibrium surface concentration ($C_\infty + \phi/R$, here R is small) which is greater than the actual concentration and will dissolve and eject material, in an attempt to increase the concentration at their surface, so becoming smaller. Larger crystallites will be heading towards a much smaller equilibrium surface concentration ($C_\infty + \phi/R$, here R is large) which is lower than the actual concentration and consequently will absorb material from the solution and increase in size. Thus there exists a critical radius, found by equating the actual concentration ($C_\infty + \Delta$) with the equilibrium concentration ($C_\infty + \phi/R$), below which crystallites will dissolve and above which they will grow in size. In terms of this diffusion model the critical radius, R_{cr}, is given by:-

$$R_{cr} = \frac{\phi}{\Delta} \qquad \textbf{Equation 3.9}$$

where Δ = Degree of supersaturation (see text)

As crystallite growth progresses, with a net removal of material from the solid solution, the supersaturation, Δ, will decrease with time and the critical radius will increase. However, the decrease in Δ will be slowed down by small crystallites dissolving, supplying material into the solid solution which will fuel the growth of larger crystallites. Lifshitz and Slezov [3.5,3.6] include a size distribution function in their model and predict a growth rate and size distribution of the form:-

$$\overline{R} = \left(\frac{4D\phi}{9}\right)^{\frac{1}{3}} t^{\frac{1}{3}} \qquad \textbf{Equation 3.10}$$

$$P(u) = \begin{cases} \dfrac{3^4 e}{2^{5/3}} \dfrac{u^2 \exp\left(-1/(1-2u/3)\right)}{(u+3)^{7/3}(1.5-u)^{11/3}} & u > 1.5 \\ \\ 0 & u \le 1.5 \end{cases} \qquad \textbf{Equation 3.11}$$

$$f(R, t) \propto P(u)/t^{4/3} \qquad \text{and} \qquad u = R/\overline{R}$$

where $f(R,t)$ = Density of crystallites with radii between
R and R+dR at time t
$\overline{R}$ = Mean crystallite radius

This distribution function is shown schematically in Figure 3.6. It can be seen that this distribution function shows a sharp decrease for large R but a slowly falling tail extending to

low R.
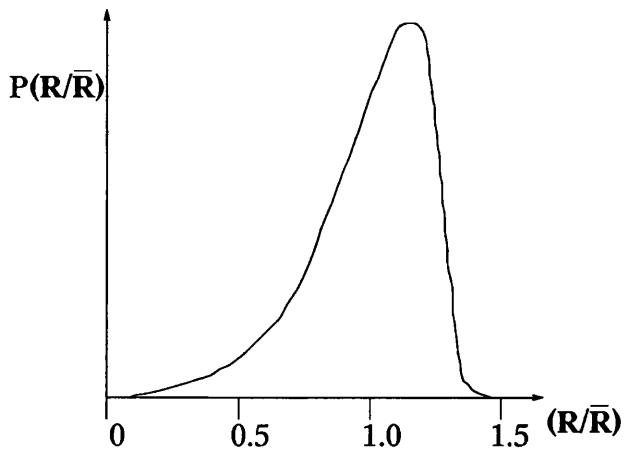
Figure 3.6   Size distribution function as calculated by Lifshitz and Slezov [3.5].

Other researchers have used numerical techniques to study the problem of particle growth from supersaturated solid solutions [3.7-3.9]. The next section will briefly review work done by researchers to measure the crystallite growth rate and size distribution.

3.2 Discussion of the Validity of the Models

In this section a review will be given of experimental measurements of growth rates and size distributions that have been presented in the literature by various research groups. Figures 3.7 and 3.8 show the variation of the crystallite diameter with annealing time as measured by Ekimov et al [3.10], with sizes determined using small angle x-ray scattering [3.11], (Figure 3.7) and Potter et al [3.2], using transmission electron microscopy, (Figure 3.8). It can be seen that the crystallite growth is well described by the $t^{1/3}$ power law predicted by Lifshitz and Slezov [3.6] with the exception of the growth of $CdSe_xS_{1-x}$ crystallites. Potter et al [3.2] attribute the failure of the Lifshitz-Slezov model to account for the growth of $CdSe_xS_{1-x}$ mixed crystals to a change in crystal stoichiometry as the heat treatment progresses. This, they suggest, results from a large difference between the diffusion coefficients of sulphur and selenium ions in glass.

Figure 3.7
Crystallite size as a function of time
as measured by Ekimov et al [3.10].
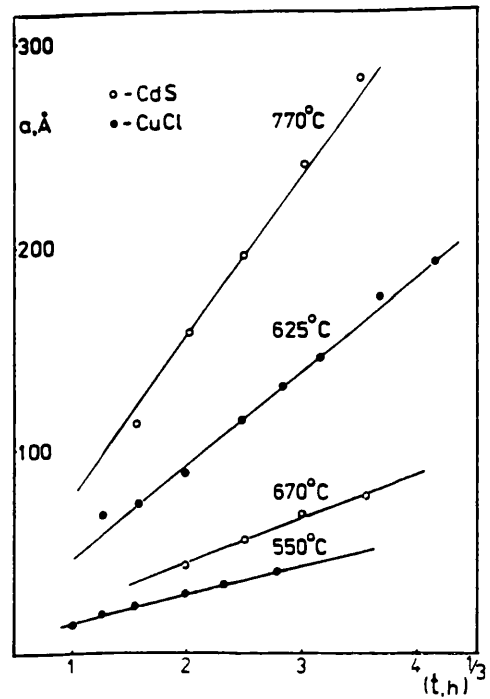
Figure 3.8
Crystallite size as a function of time
as measured by Potter et al [3.2].
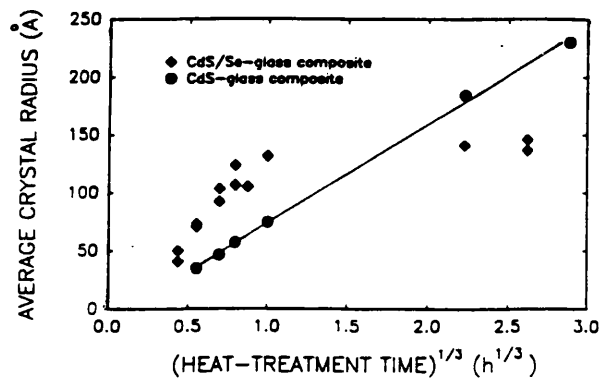
Figures 3.9 and 3.10 show measurements of the crystallite size distribution made by Borrelli et al [3.1] and Potter et al [3.2], both using transmission electron microscopy to determine the sizes of the crystallites. The agreement between these measured values and the Lifshitz-Slezov model is not as striking as in the case of the growth rate, however both figures show some asymmetry towards lower crystallite sizes as predicted by Lifshitz and Slezov. Potter et al (Figure 3.10) have superimposed the Lifshitz-Slezov distribution function on top of their measured data.

Figure 3.9
Crystallite size distribution as measured by Borrelli et al [3.2].
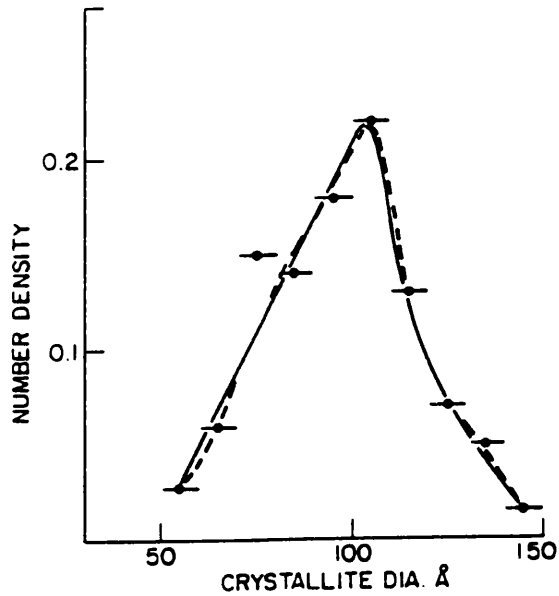
Figure 3.10
Crystallite size distribution as measured by Potter et al [3.2].
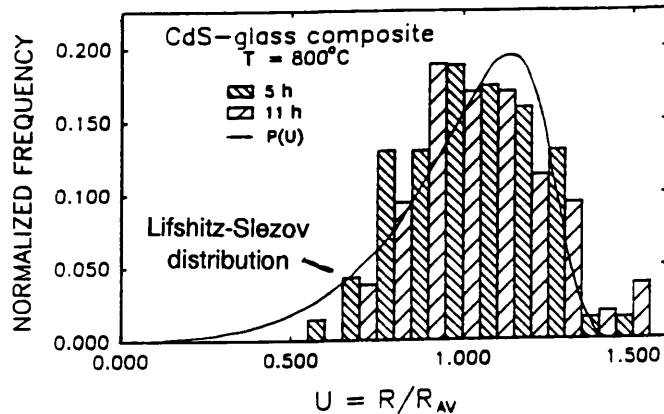
Figures 3.11 and 3.12 show the crystallite size distributions measured by Woggon et al [3.12] using small angle x-ray scattering. These measured size distributions clearly do not agree with that calculated by Lifshitz and Slezov. Woggon et al attribute this lack of agreement to the invalidity of the Lifshitz-Slezov calculation for the earlier stage of crystallite growth before smaller crystallites start to redissolve back into the glass matrix. The samples they measured were annealed at 580C for 80 hours (Figure 3.11) and 600C for 170 hours (Figure 3.12). They find that lower growth temperatures give a smaller size distribution for a given mean crystallite diameter. Figures 3.11 and 3.12 both show approximately the same mean crystallite radius but the sample prepared at lower temperatures shows a smaller size distribution.
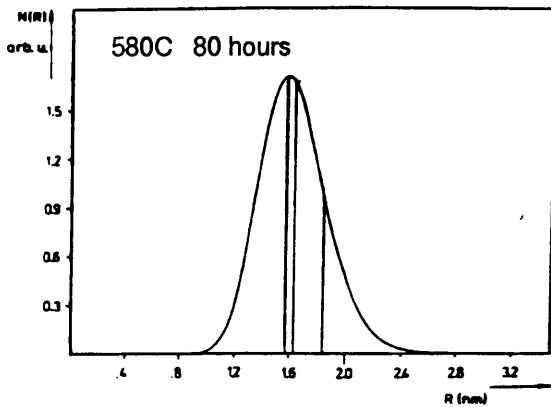
Figure 3.11
Crystallite size distribution as
measured by Woggon et al [3.12].
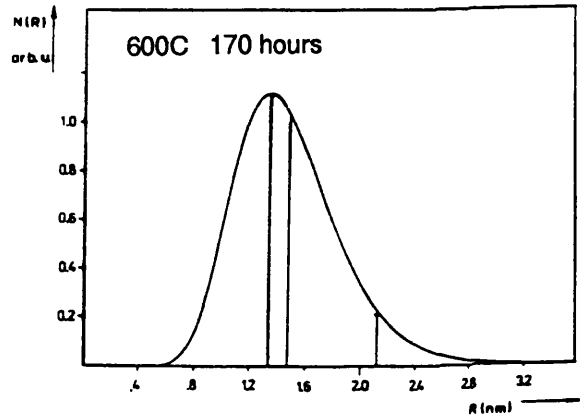
Figure 3.12
Crystallite size distribution as
measured by Woggon et al [3.12].

3.3 Summary

In conclusion, the growth of crystallites from a highly saturated solid solution of Cd, Se and S ions within a glass matrix can be qualitatively understood in terms of very simple models describing diffusion processes or the free energy of the system. All the stages of nucleation, growth and dissolving of crystallites can be understood by referring to these simple descriptions. More involved, quantitative modelling by Lifshitz et al and others have been shown by some groups to provide, within the assumptions of the models, an adequate description of crystallite growth.

This remarkable tendency of Cd, Se and S ions within a doped glass, under appropriate thermal conditions, to cluster and form sub-microscopic crystalline particles allows the production of semiconductor crystals whose dimensions range from a few nanometres, and contain only a few hundred atoms, to several hundred nanometres, and larger, which possess essentially bulk-like properties. Such materials form an almost unique system in which to study the transition between the properties of macroscopic crystals and the properties of large molecules.

Chapter 4 - Experimental Equipment

This chapter will describe the experimental equipment and methodology used in this project to characterise the optical properties of microcrystallite doped glass. The chapter will be subdivided according to the experimental techniques used, and within each sub-section there will be a description of the properties of the equipment.

4.1 Absorption Measurements

In this work most absorption measurements were made using a tungsten halogen lamp operating at 12V (4.25A) with an optical power output of approximately 0.8W. The spectral output of the tungsten halogen lamp closely approximates a black body radiator at 3200K (the lamp filament temperature). Light dispersion was performed using either a Jobin Yvon U1000 spectrometer or a Jobin Yvon THR1000 spectrometer with light detection using a photomultiplier tube. These pieces of equipment will be described in detail in subsequent sections. For these measurements white light from the tungsten halogen lamp was directed through the sample and the transmitted light analysed using the spectrometer and detector. The measurement was then repeated with the sample removed to obtain a reference spectrum and the two spectra divided to obtain the transmission of the sample. In addition some measurements were performed using an Elmer-Perkins spectrophotometer which directed dispersed light through the sample and a reference arm of the spectrometer simultaneously. Typical absorption coefficients up to which measurements were performed were ~400cm^{-1}.

4.2 Photoluminescence Measurements

These measurements were performed using a Spectra Physics model 2045 argon ion laser as an excitation source and a Jobin Yvon U1000 double spectrometer to analyse the emitted light. The emitted light was then detected using a Hamamatsu photomultiplier tube and standard photon counting techniques. In order to remove plasma lines from the argon ion laser beam a Spectrolab "Laserspec III" filter monochromator, with either visible or UV optics, was used. A schematic diagram of the equipment is shown in Figure 4.1, below.
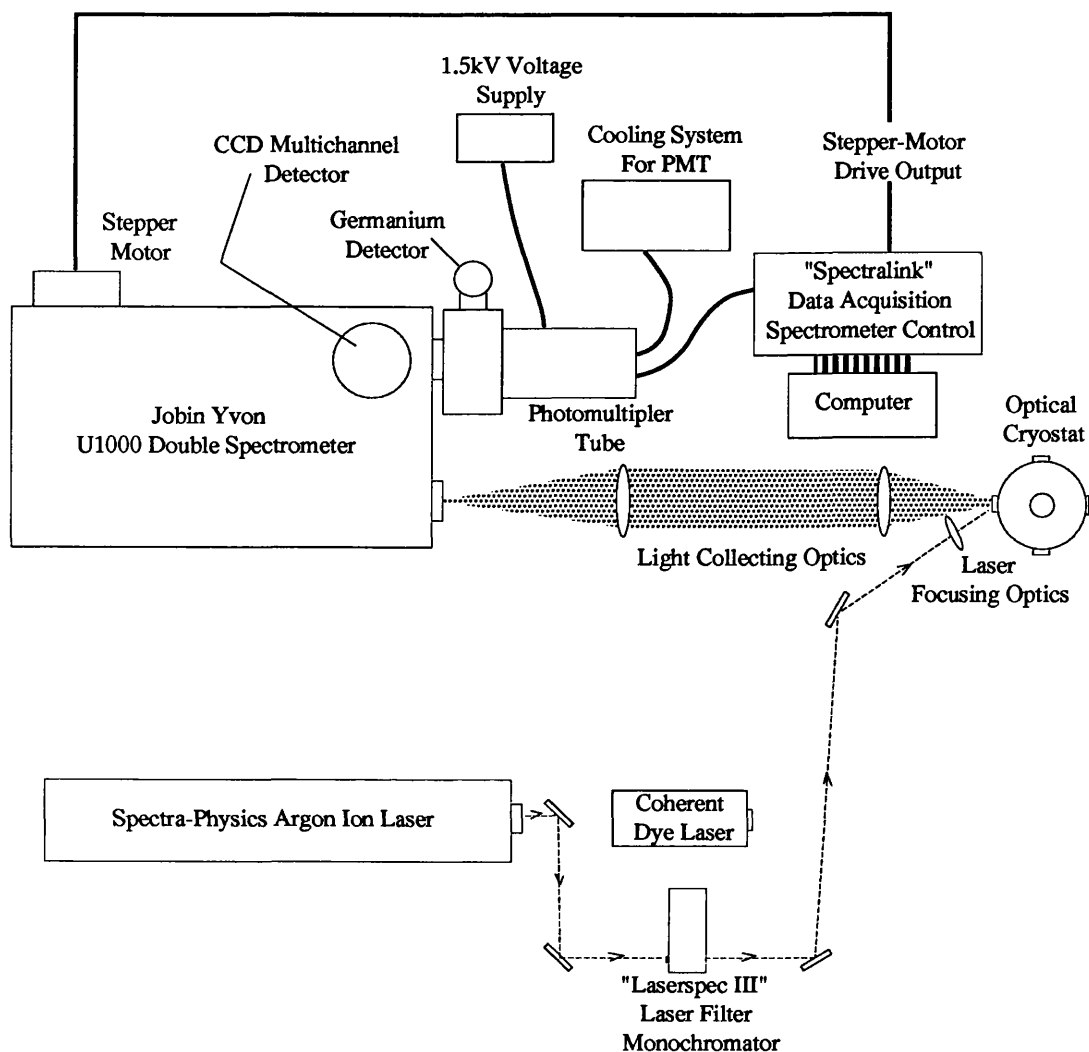
Figure 4.1 Schematic diagram of the experimental apparatus used for photoluminescence and Raman scattering measurements.

Figure 4.2 illustrates the spectral response of the U1000 system, consisting of light collecting optics, spectrometer mirrors, 1800 grooves/mm gratings and a Hamamatsu R943-02 photomultiplier tube cooled to -23C. This spectral response was measured as part of a previous project by passing light from a black body radiator into the spectrometer, measuring the spectrum of the source and then correcting for the known wavelength dependence of the emission from the black body radiator. In this case a piece of graphite placed in a stabilised oven and heated to 900C formed the black body radiator [4.1,4.2].
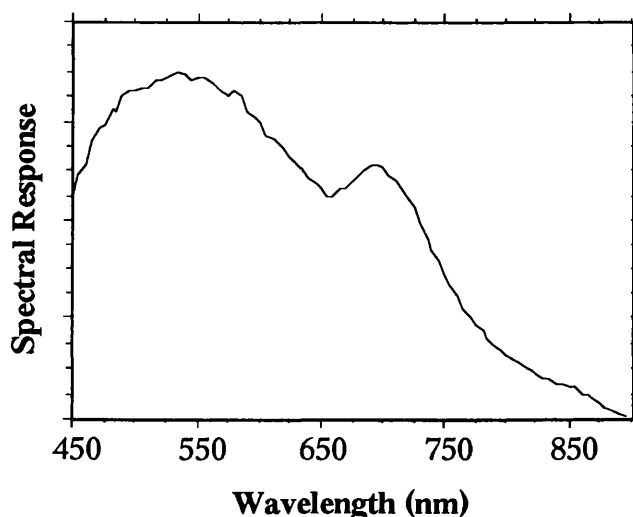
Figure 4.2 Spectral response of U1000 system.

As will be seen later (chapter five), it is important to know the spectral response of the photoluminescence system since the spectra of very broad emissions should be corrected for variations in the system's ability to detect light at different wavelengths. It also gives a representation of the useful spectral region over which the system can effectively operate.

4.2.1 Excitation source

In the earlier part of this project the excitation source was a Spectra Physics model 2030 argon ion laser which was later upgraded to a Spectra Physics model 2045 argon ion laser. The Spectra Physics model 2045 argon ion laser was provided with optics allowing single line operation in the visible and UV. During the course of this project more than one laser tube was used and the output powers varied between tubes. Typical powers available in single line operation are given in Table 4.1, below [4.3,4.4]. A knowledge of the powers obtainable on the available lasing lines is useful, since for Raman scattering there are, at times, specific reasons (such a resonant effects) for exciting the sample within a particular wavelength range.

Wavelength	Power	Wavelength	Power
4545 Å	480 mW	4880 Å	9.0 W
4579 Å	1.6 W	4965 Å	3.4 W
4658 Å	850 mW	5017 Å	1.8 W
4727 Å	1.4 W	5145 Å	8.9 W
4765 Å	3.3 W	5287 Å	1.1 W

Table 4.1 Output power available from the Spectra Physics model 2045 argon ion laser operating in single longitudinal mode.

58

4.2.2 "Laserspec III" Filter Monochromator

This prism filter monochromator with glass optics (type SF2) can operate with a transmission of over 75% from 350nm to 900nm. With silica optics anti-reflection coated for ultra-violet operation the monochromator gives over 75% transmission from 200nm to 400nm. The monochromator has a typical stray light rejection of 1×10^{-9}, although it does show a dependence upon the wavelength selected, with a transmission bandwidth of around 0.4Å [4.5,4.6]. A diagram illustrating the light path through the filter monochromator is shown in Figure 4.3, below.
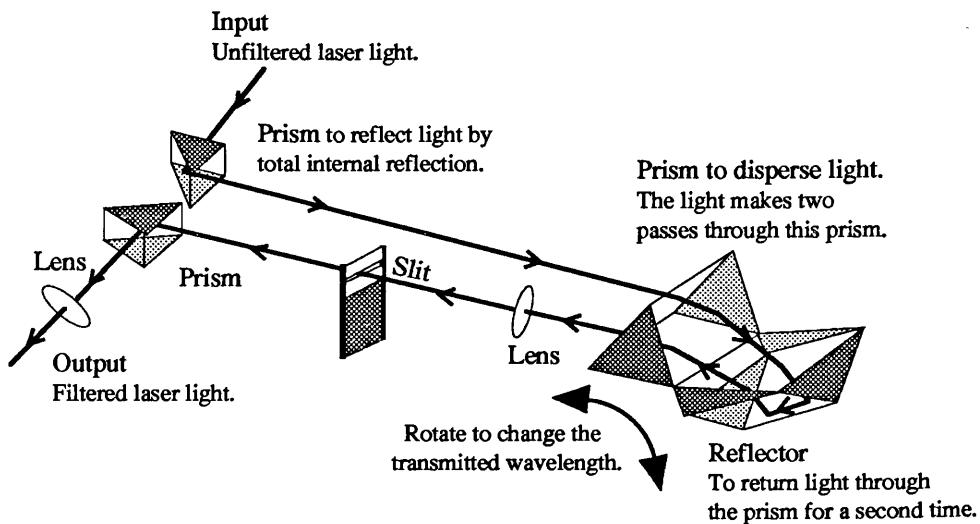
Figure 4.3   Schematic diagram of the light path through the "Laserspec III" filter monochromator.

4.2.3 "Spectralink" Spectrometer Controller

The "Spectralink" is a unit which can be used to control Jobin Yvon spectrometers. Appropriate modules installed within this unit allow computerised control of the spectrometer's movement and data acquisition. The functions of the "Spectralink" relevant to the work presented here are outlined below.

(a) Control of the Spectrometer's Stepper Motor.

The motor drive module of the "Spectralink" provides the appropriate pulse sequences to drive a four phase stepper motor. Internal switch settings allow the current to each phase, from the "Spectralink", to be varied between 3.8A/phase and 0.6A/phase. These outputs, supplying the stepper motor, can provide a maximum voltage of up to 20V.

(b) Data Acquisition.

The "Spectralink" acts as an interface between detecting elements and a computer. It is provided with two input channels allowing data from up to two detectors to be collected simultaneously.

(c) High Voltage Supply for Photomultiplier Tubes.

The "Spectralink", fitted with an appropriate module, can supply the necessary high voltage to a photomultiplier tube. The photomultiplier tube used on the THR1000 spectrometer (described below) was powered from the "Spectralink".

With appropriate computer software this unit will perform all the operations necessary to measure a spectrum. It will move the spectrometer to the start wavelength, stop, perform a measurement from a selected detector then move to the next wavelength and perform another measurement. This is repeated until the entire spectrum is obtained [4.7].

4.2.4 Spectrometer

The spectrometer used to analyse emitted light for most of the photoluminescence measurements and all of the Raman scattering measurements was a Jobin Yvon Ramanor U1000 double spectrometer with a one metre focal length. A schematic diagram of the spectrometer is shown in Figure 4.4 [4.8,4.9].
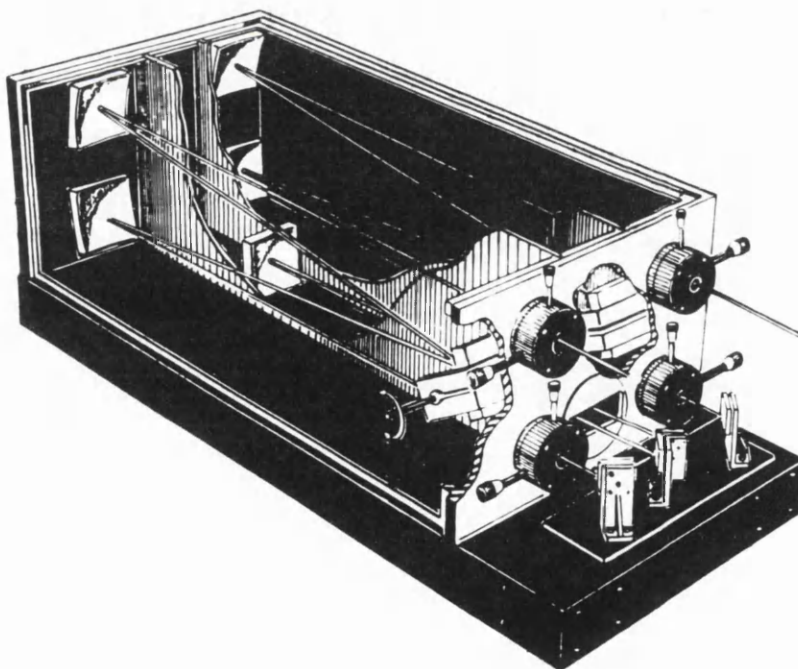
Figure 4.4(a) Schematic diagram of the U1000 double spectrometer.
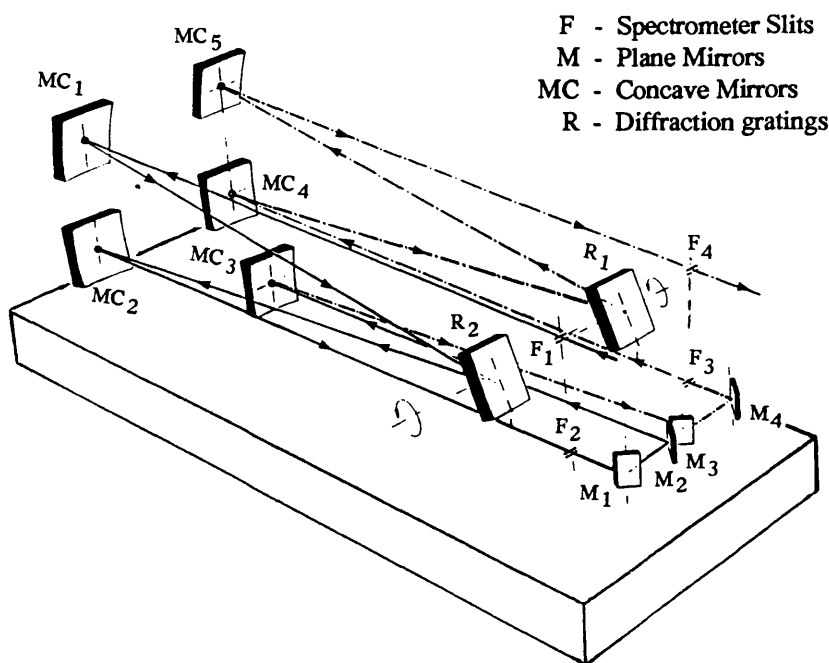
Figure 4.4(b) Light path through the U1000 double spectrometer.

This spectrometer utilises two gratings with additive dispersion [4.8]. For the work presented here two 1800 grooves/mm gratings were used giving a possible resolution of $0.15cm^{-1}$ at 579.1nm (Hg line). The actual resolution achieved during operation depends upon the slit widths chosen (F_1, F_2, F_3 and F_4 in Figure 4.4(b), above). The spectrometer, with these gratings, provides a dispersion of $9.2cm^{-1}/mm$ (0.243nm/mm) at 514.5nm and a stray light rejection of 10^{-14} at $20cm^{-1}$ from the Raleigh line [4.9]. Such high dispersion and resolution were not important for measuring the broad photoluminescence emission from semiconductor doped glass but were important, along with the stray light rejection, for the measurement of Raman scattering spectra, where, as will be seen later in chapter five, it was necessary to analyse the lineshape of a relatively narrow and weak spectral emission. The range the spectrometer can cover mechanically (with 1800 grooves/mm gratings) is 327.5nm to 910nm. The spectral range that can be effectively covered is determined by the efficiency required of the diffraction gratings. The broad photoluminescence emission from the microcrystallite doped glass investigated in this work necessitated the measurement over a spectral region in which the response of the gratings varied considerably. The grating efficiency as a function of wavelength is shown in Figure 4.5. This grating efficiency forms one of the components which determine the overall spectral response of the system (see above).
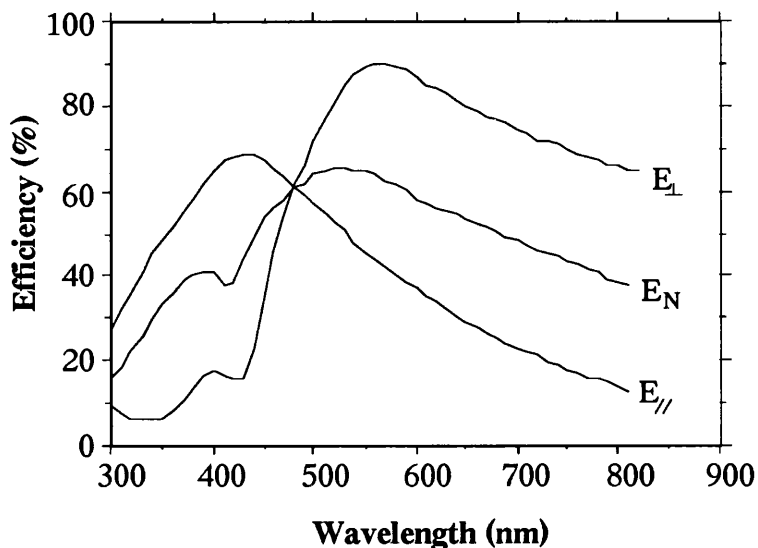
Figure 4.5 Grating efficiency curves for 1800 grooves/mm gratings for light polarised perpendicular to the grooves ($E_\perp$), light polarised parallel to the grooves ($E_{//}$) and unpolarised light (E_N).

The spectrometer gratings were rotated by a four phase, 200 step per revolution Superior Electric stepper motor. This stepper motor was controlled by a Jobin Yvon "Spectralink" spectrometer controller interfaced to an IBM compatible computer. Initially computer control was implemented using software written as part of a previous project [4.1], later the commercially written software package "PRISM" from ISA was used for data acquisition [4.10].

4.2.5 Light Detection

Light detection was performed using the method of photon counting with a Hamamatsu R943-02 photomultiplier tube with a Cs activated GaAs photocathode, with an approximate spectral range of 160nm to 930nm. In order to reduce the device's dark noise the tube was cooled to approximately -23C using a Pacific instruments PMT housing and temperature controller, utilising the Peltier effect [4.11,4.12,4.13]. The PMT was operated at 1.5kV, supplied by a Thorn EMI photomultiplier power supply (type PM 28B) [4.14]. A Pacific Instruments model 3470/AD6 amplifier discriminator was used to allow photon counting to be employed. The discriminated pulses from this unit then formed the input to one of the data channels of the "Spectralink", with internal switches in the "Spectralink" suitably set for pulse counting. The broad emission from the samples investigated in this work necessitated the measurement of spectra over a range where the quantum efficiency of the detector varied significantly. Figure 4.6, below, show a typical spectral response for this type of photomultiplier tube [4.15]. The radiant sensitivity is a measure of the photomultiplier's response per unit flux of energy (it is not its quantum efficiency).
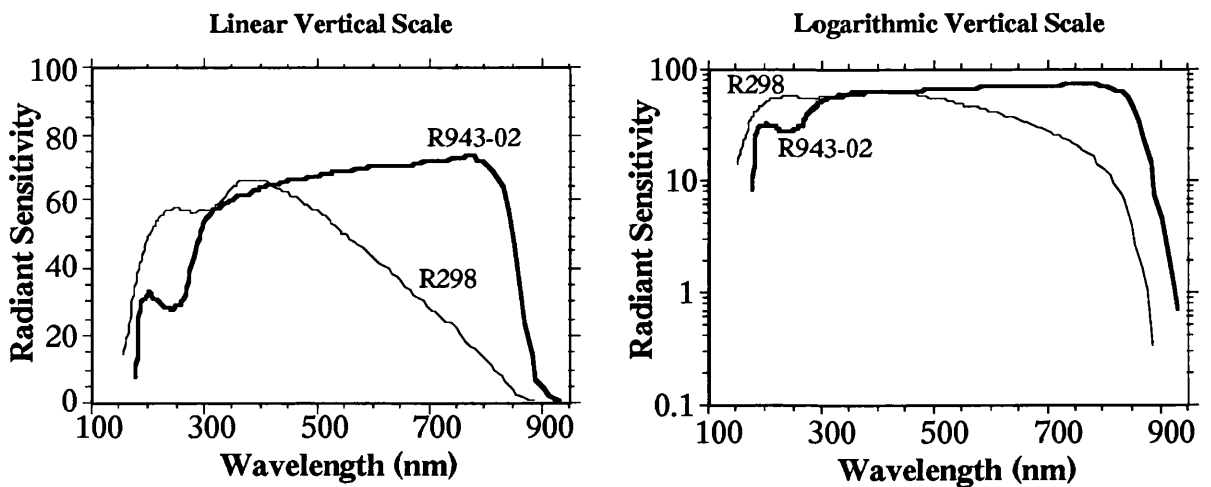
Figure 4.6 Spectral response of photocathodes in Hamamatsu photomultiplier tubes R943-02 (————), as used on the U1000 system, and R298 (————), as used on the THR1000 system.

The response of the detector with wavelength, along with the efficiency of the spectrometer's diffraction gratings, form the major components of the system's overall spectral response. Other less important factors (for the spectral region being considered here) include the transmission of the light collecting optics and variations, with wavelength, of the reflection coefficients of mirrors within the spectrometer.

4.3 Raman Scattering Measurements

The measurement of Raman spectra presented in this thesis were made using the above laser and spectrometer system. The measurement of Raman spectra, spectrally narrower and often very much weaker than the photoluminescence emissions investigated in this project, made full use of the double spectrometer's dispersion and stray light rejection capabilities. Light detection was either performed by photon counting, using the Hamamatsu R942-02 photomultiplier tube, as described above, or a CCD camera supplied by Astromed Limited. The properties of this detector relevant to the work of this thesis are presented below.

4.3.1 CCD Camera

The CCD (charge coupled device) camera consists of a two dimensional array of CCD light detecting elements with the light entering the spectrometer being dispersed parallel to one axis of the array. Thus detector elements along this axis of the array each measure the light intensity of a different wavelength, allowing many different points in the spectrum to be measured in parallel. This has the obvious advantage of allowing spectra to be measured much more quickly, which is important when detecting weak signals which require long integration times in order to achieve the desired signal to noise ratio. All the detector elements along an axis

perpendicular to the light's dispersion direction measure the same wavelength. Thus the measurements from all the elements in rows perpendicular to this dispersion direction can be summed to give an intensity at each wavelength with an improved signal to noise ratio. The quantum efficiency of the CCD camera, as measured by the manufacturers, at -40C is shown below in Figure 4.7. The CCD camera used in this work had an antireflection coated active area to extend its spectral response into the ultra violet. The quantum efficiency is, of course, not the same as the radiant sensitivity, which was shown earlier for the photomultiplier tubes used in this project. The quantum efficiency represents the device's response per unit flux of photons, while the radiant sensitivity measures the device's response per unit flux of energy. It is simple to calculate the relationship between the form of these two curves. Suppose R_P represents the device's response per unit flux of photons and R_E its response per unit flux of energy, both as a function of wavelength λ, then:-

$$R_E \propto R_P \lambda \qquad \textbf{Equation 4.1}$$

In order to allow a comparison with the data presented for photomultiplier tubes (see Figure 4.6) the variation of the radiant sensitivity as a function of wavelength, as calculated from Astromed's quantum efficiency data, is also shown below, in Figure 4.7.
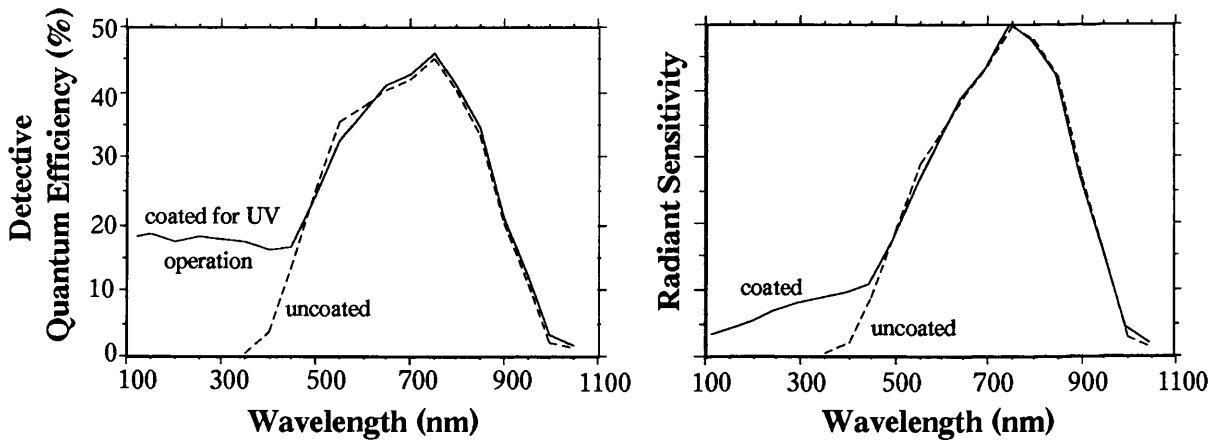
Figure 4.7   Quantum efficiency and radiant sensitivity of the CCD detector
with coated (———) and uncoated (-----) active area.

As can be seen from Equation 4.1, and the above graphs, the maximum quantum efficiency will occur at a wavelength shorter than the maximum in the radiant sensitivity (see section 4.4.6, below). The spectral range which can be covered by the CCD array depends upon the dispersion of the spectrometer. With two 1800 grooves/mm gratings the dispersion of the U1000 was such as to allow the CCD to cover a range of approximately 2nm (or approximately 120cm^{-1} at a centre wavelength of 488nm). In order to obtain a spectrum covering a larger range the spectrometer can be moved to various wavelengths and a separate "frame" taken at each of these wavelengths. Provided the spectral range covered by each "frame" overlap at the

appropriate edges, the "frames" can be joined together to give the complete spectrum. However, due to slight variations in sensitivity of individual CCD elements across the array it is inadvisable to join together a very large numbers of "frames", since the precise lineshape of spectral features covering many frame will not be accurately represented. If it is necessary to obtain a spectrum covering a wide spectral range it is preferable to use gratings which give a lower dispersion, D, which corresponds to gratings with a lower groove density (ie of larger period). See Figure 4.8 for an example of the operation of a simplified plane grating spectrometer, with a grating period of d.

For Constructive Interference
$$d \sin \theta = n \lambda$$

Incident Light

$d \sin \theta$

θ

d

Diffraction Grating

f

dθ

$f \, d\theta = dx$
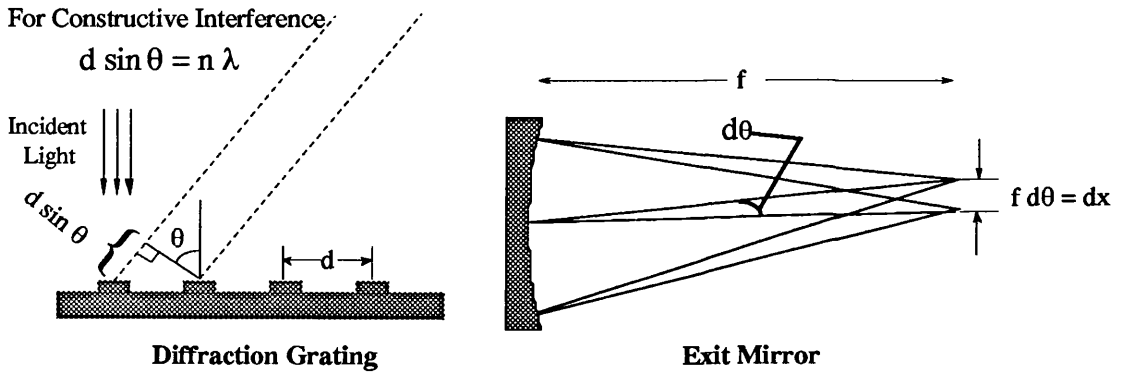
Exit Mirror

$$D = \frac{dx}{d\lambda} = f \frac{d\theta}{d\lambda} = \frac{n \, f}{d \cos \theta} \qquad \textbf{Equation 4.2}$$

where   D = Spectrometer's dispersion
x = Distance in the direction of dispersion
λ = Wavelength of incident light
f = Focal length of exit mirror
n = Order in which diffraction grating is used
d = Period of diffraction grating
θ = Angle of diffracted light with the normal to the diffraction grating
     Also this is the angle at which the light from the diffraction
     grating is incident with and reflected from the exit mirror

Figure 4.8   Diagram illustrating the operation of a single
grating spectrometer.

Of course, the directions of incident and diffracted light in the above diagram do not represent the geometries of the spectrometers discussed here. The actual spectrometers used in this work employ Czerny-Turner type geometries (see Figures 4.4, 4.12 and 4.13) [4.8,4.16]. Since the CCD measures many different wavelengths in parallel it is necessary to allow a range of wavelengths through slits F_2 and F_3 (see Figure 4.4(b)). Thus these slits must be opened much wider (approximately 10mm) than during the normal operation of the spectrometer, using for example a photomultiplier tube. Slit F_1 can be narrow as normal, since the light passes through this before being dispersed, and slit F_4 is not used; the light is reflected into the CCD, using a mirror, before it reaches slit F_4. Of course, the stray light rejection capability of the

spectrometer suffers seriously as a result of having slits F_2 and F_3 so wide. This results in a significant amount of stray laser light being detected as far as 200cm^{-1} from the laser line. The CCD camera was provided with a liquid nitrogen dewar allowing the detector to be cooled, giving an improved noise level. The detector element, which is slightly removed from the liquid nitrogen space, can reach temperatures of 130K to 140K. Data acquisition with the CCD camera was made using the "PRISM" software supplied by ISA.

4.4 Photoluminescence Excitation Spectroscopy Measurements

As part of this project a system was set up to perform photoluminescence excitation measurements. A schematic diagram of the experimental set-up is shown in Figure 4.9(a). With this technique the sample is excited by light of a variable wavelength while the light emitted by the sample at a fixed wavelength is measured as a function of the wavelength of the excitation light. The excitation source was a tungsten halogen lamp used in conjunction with a small Jobin Yvon HR25 spectrometer to produce a highly tunable monochromatic light source. This light source was chosen because of the width of the spectral features of the sample being investigated, which required a light source tunable over several hundred nanometres. The intensity of light transmitted by the HR25 spectrometer (for the experimental slit widths of 2mm) and the short pass filter as a function of the selected wavelength was measured using a Coherent Labmaster E power meter with a silicon detector head (type LM-2). This meter has an internally stored spectral calibration with respect to which it automatically corrected the measured power. This measured power output is shown in Figure 4.9(d), below. The reasons necessitating the use of the short pass optical filter are discussed below. The broad spectral emission of the samples being investigated did not require a highly monochromatic excitation source. The HR25 slit widths were chosen to give a transmission spectrum with a full width half maximum of ~5nm, which is considerably narrower than the features in the measured PLE spectrum (see chapter five). This light was then focused onto the sample using a microscope objective. The light emitted by the sample was collected using a camera lens and dispersed using a Jobin Yvon THR1000 1m single spectrometer. Light detection was performed using a Hamamatsu R298 photomultiplier tube operating at room temperature in current mode. It was found necessary to place a short pass optical filter after the HR25 spectrometer in order to remove the background white light from the tungsten halogen lamp which was not rejected by the HR25. This filter removed the background light which occurred at approximated 700nm-750nm, the typical wavelength range within which the photoluminescence was observed, while allowing the excitation wavelength to be transmitted (typically 400nm-600nm). Although the intensity of this background light was extremely small compared with the intensity transmitted at the selected wavelength it was found to be large enough to completely mask the weak PLE signal being detected at 750nm. The long pass filter placed

before the THR1000 spectrometer was used to filter out the excitation wavelength (eg 400nm-600nm) and prevent it from reaching the detector in the form of stray light passing through the THR1000 spectrometer (compare the stray light rejection capabilities of the U1000 and THR1000 spectrometers). A brief description of the various system components will be given below.
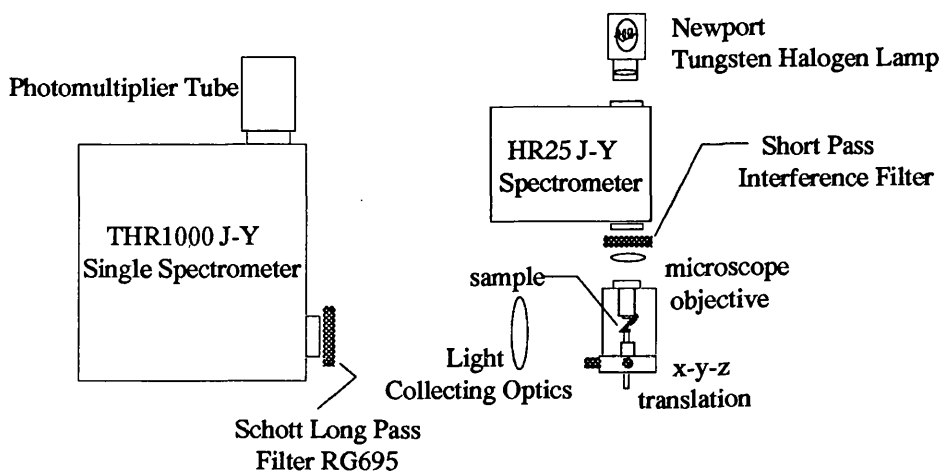
Figure 4.9(a) Schematic diagram of photoluminescence excitation spectroscopy apparatus.
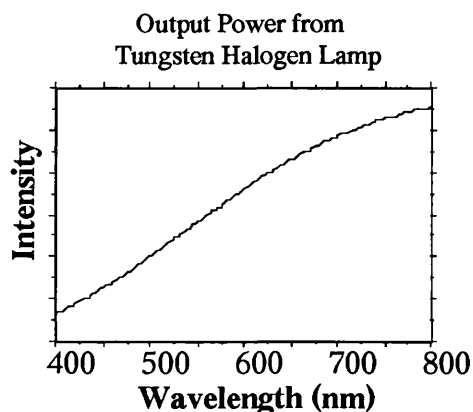
Figure 4.9(b)

Figure 4.9(c)

Figure 4.9(b) Power output of tungsten halogen lamp.
   (c) Transmission of short pass interference filter.
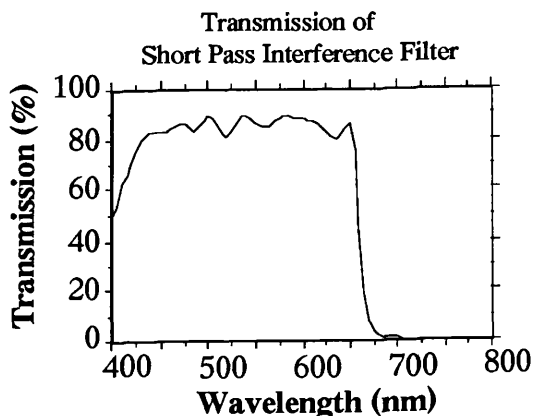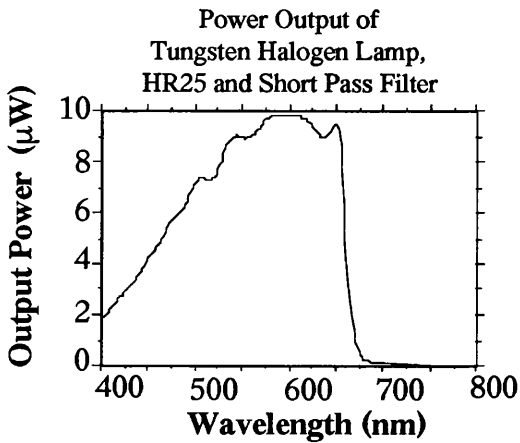
Figure 4.9(d)
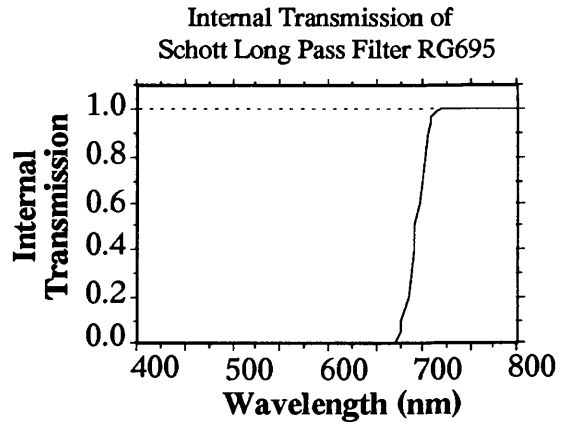
Figure 4.9(e)

Figure 4.9(d) Power output from tunable light source (tungsten halogen lamp, spectrometer and short pass filter).

(e) Transmission of Schott filter glass RG695.

4.4.1 White Light Source

This lamp was a Newport Corporation Model 780 tungsten halogen lamp which operates with a voltage of 12V at a current of 4.25A (ie consumes approximately 50W of electrical power) and produces an optical output power of 0.8W. It produces an output closely approximating a black body radiator at 3200K (the lamp's filament temperature) [4.17]. The output from such a black body radiator is given by Equation 4.3 [4.18] and a schematic diagram of the lamp is shown in Figure 4.10, below.

$$P \propto \frac{\lambda^{-5}}{\left(\exp\left(\dfrac{hc}{kT\lambda}\right) - 1\right)} \qquad \textbf{Equation 4.3}$$

where P = Energy emitted per unit time between wavelengths λ and $\lambda + d\lambda$
  λ = Wavelength (m)
  h = Planck's constant
  c = Speed of light
  k = Boltzmann's constant
  T = Absolute temperature

68
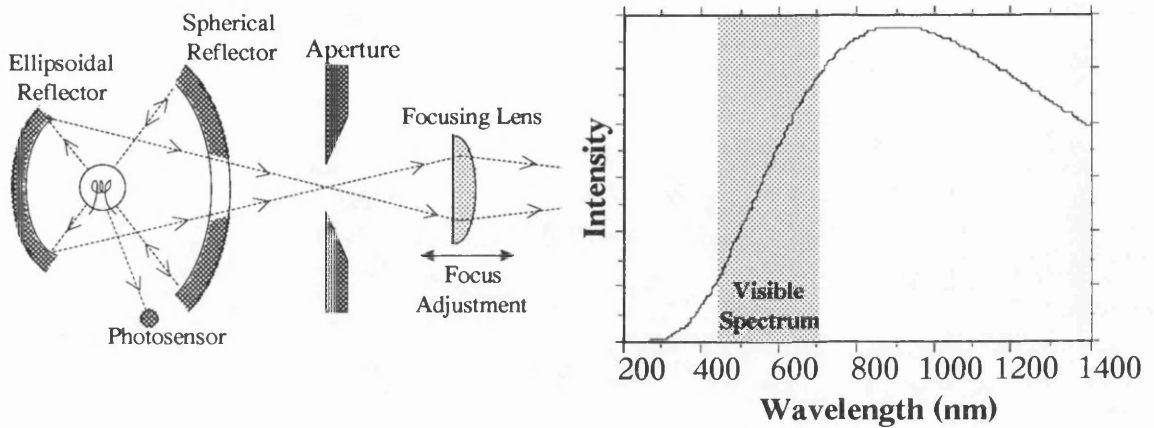
Figure 4.10 Schematic diagram of Newport tungsten halogen lamp
and its spectral output as given by Equation 4.3.

As can be seen from the above diagram, the lamp incorporates a photosensor forming part of a feedback loop which regulates the current flow through the lamp filament in order to keep the lamp's optical power output constant to within 0.05% over a ten minute period. The lamp's output is focused by a fused quartz lens with a focal length of two inches. Axial motion of this lens allows the aperture plate to be imaged at a distance of eight inches to infinity from the end of the lens assembly [4.17]. The spectral output of this lamp over the region of interest in this PLE experiment is shown in Figure 4.9(b).

In order to achieve higher excitation powers a second white light source was constructed from a 150W (electrical power) bulb with a parabolic reflector and a transformer. The transformer used came supplied with a wound primary but an empty secondary part of the bobbin, allowing the secondary windings to be chosen for the particular application. The number of secondary windings being determined by the required secondary voltage and the load at the secondary (a 1% increase in the number of secondary turns being required for every 25VA loading) [4.19]. This white light source was found to produce an optical output power of 20W, as measured by a Coherent Labmaster E power meter with a calorimeter sensor head (type LM45), with a flat spectral response from $0.3\mu m$ and $10.6\mu m$ [4.20]. Such a detector will accurately measure the power from a white light source, such as this lamp, without the need to correct for its spectral response. This light source is illustrated schematically in Figure 4.11, below.
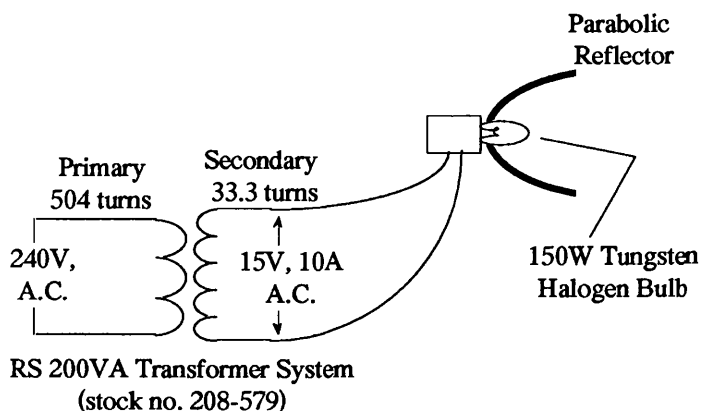
Figure 4.11 Lamp used to obtain higher excitation powers than those obtainable with the Newport lamp.

The parabolic reflector brought the light to a beam waist of 1cm at a distance of 2cm from the output end of the reflector. This lamp lacks the power stabilising feedback loop of the commercial lamp, however, its power output was found to be stable to within less than 2% over a period of two hours, which was considered adequate.

4.4.2 Jobin Yvon HR25 Spectrometer

This is a 25cm single spectrometer which was used with a 600 grooves/mm diffraction grating and is shown schematically in Figure 4.12, below.
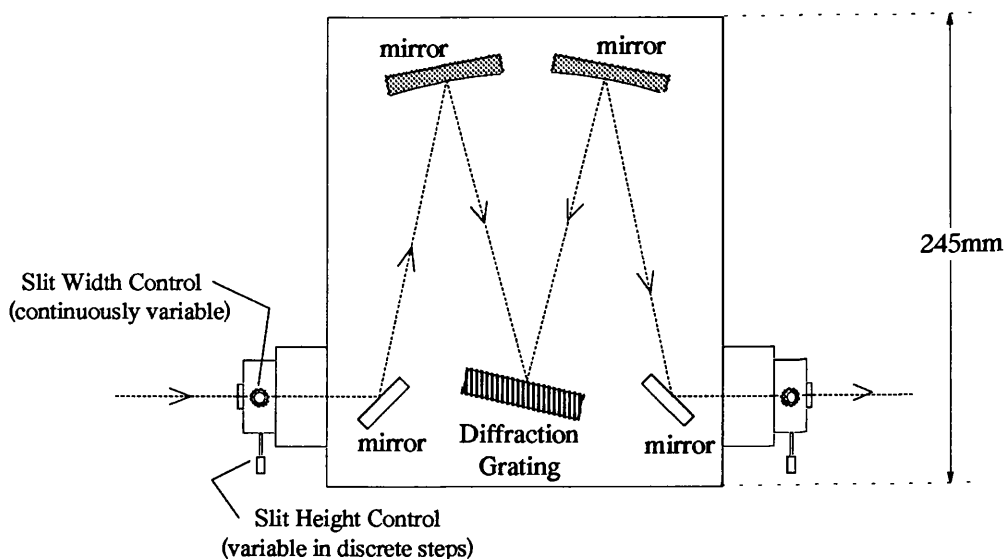
Figure 4.12   Schematic diagram of Jobin Yvon HR25 spectrometer.

The spectrometer was supplied with a RS 4-phase stepper motor (model 332-947) with a 7.5° step angle which was stepped down to a 0.03° step angle by a gearbox (model RS 336-416).

70

This motor operated at 12V (100mA) [4.21] which are lower than the voltage and current supplied by the Jobin Yvon "Spectralink". The "Spectralink" operates as a current source supplying either 3.8A/phase or 0.6A/phase, depending upon internal switch settings, up to a maximum supply voltage of 20V [4.7]. Although this output supplied the correct pulse sequences to drive the HR25's stepper motor, operating above its specified voltage caused it to heat up considerably. This problem was overcome by putting a resistance of 195Ω (two 390Ω resistors in parallel) in series with each phase of the stepper motor (the "Spectralink" was also operated in its 0.6A/phase mode). In addition to these current limiting resistors a suitable calibration of the HR25 was made, relating the spectrometer's transmission wavelength to the stepper motor position. The wavelength change is proportion to the number of steps moved by the stepper motor for this spectrometer, which incorporates a sine bar drive [4.22].

4.4.3 Short Pass Optical Filter

This was a Newport Corporation interference filter which was supplied by the manufacturers with a measured transmission spectrum, which is shown in Figure 4.9(c). The power available from the monochromatic light source, comprising the Newport lamp, the HR25 spectrometer and the short pass filter, for a bandpass of ~5nm is shown in Figure 4.9(d). This is the power with which the sample was excited.

4.4.4 Long Pass Optical Filter

This filter was a piece of polished Schott filter glass of type RG695 and its transmission characteristics are shown in Figure 4.9(e) [4.23]. As mentioned previously this filter was used to compensate for the THR1000's relatively poor (compared with the U1000) stray light rejection capabilities by filtering out the excitation wavelengths. Incidentally, Schott filter glass RG695 is a semiconductor doped glass containing CdSe microcrystallites (see chapters one and five).

4.4.5 THR1000 Spectrometer

The spectrometer used to analyse the emitted light was a Jobin Yvon 1m THR1000 single spectrometer (shown schematically in Figure 4.13) with a possible resolution of 0.01Å and a stray light rejection of 10^{-5} measured 8 bandpasses of the spectrometer away from the 632.8nm HeNe laser line. It was used with a 600 grooves/mm diffraction grating, the spectral efficiency of which is shown in Figure 4.14, and light was detected using a Hamamatsu R298 photomultiplier tube (see the description below) in the "Detector #1" position shown in Figure 4.13 [4.24,4.25].
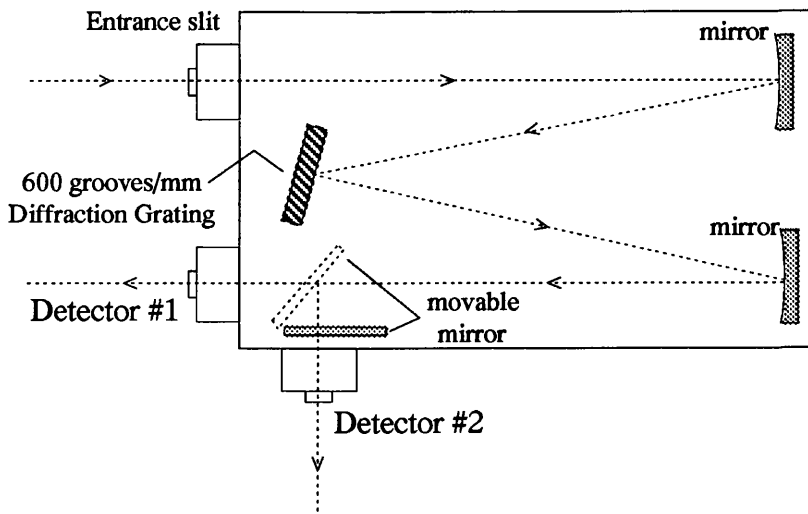
Figure 4.13 Schematic diagram of the THR1000 single spectrometer.
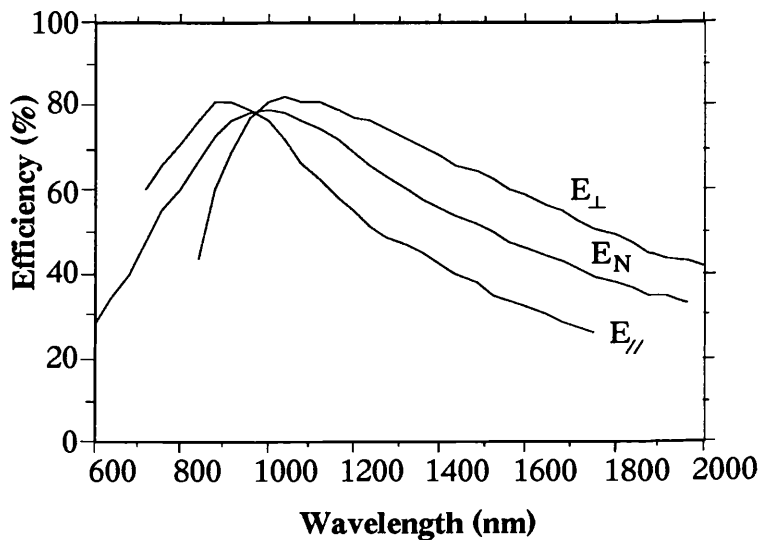
Figure 4.14 Grating efficiency curves for the 600 grooves/mm grating for light polarised perpendicular to the grooves ($E_\perp$), light polarised parallel to the grooves ($E_{//}$) and unpolarised light (E_N).

The spectral response of this system was measured using the Newport tungsten halogen lamp (see section 4.4.1) assuming its output to be that of a black body radiator at 3200K. Light from this source was directed into the spectrometer and a spectrum recorded, which was then normalised with respect to the output power of the white light source to obtain the response of the system. In order to avoid the measurement of second order diffracted light the spectrum was measured in various sections. Within each section long pass optical filters, with flat transmission characteristics over the region being measured, were used to remove the short wavelength component of the lamp output and so eliminate its second order spectrum. This measured spectral response is shown in Figure 4.15. It should, of course, be remembered that the measured spectral response is the response of the whole THR1000 system, consisting of light collecting optics (in this case a camera lens), the THR1000 (mirrors and grating) and the detector (see section 4.4.6, below).

72
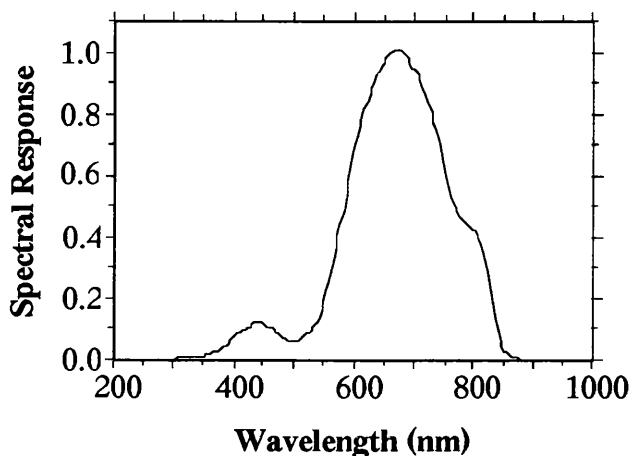
Figure 4.15(a)
Spectral response of THR1000 system (linear scale).
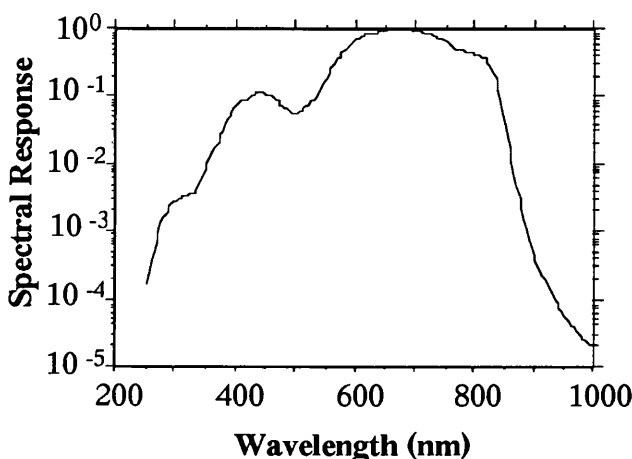
Figure 4.15(b)
Spectral response of THR1000 system (logarithmic scale).

4.4.6 Light Detection

The signal emitted by the sample was detected using a Hamamatsu R298 photomultiplier tube operating at room temperature in current mode, with its current output forming the input to the "Spectralink". The "Spectralink" also supplied the high voltage (1.0kV to 1.2kV) necessary to operate the photomultiplier tube. The radiant sensitivity of this device is shown in Figure 4.6. This device has a peak quantum efficiency at 260nm and a peak radiant sensitivity at 400nm.

4.5 PL Measurements Varying The Excitation Intensity

At times during the course of this project it was necessary to measure the intensity of the light emitted by a sample as a function of the intensity of the excitation source. To achieve this a continuously variable attenuator on a rotating mount made by the mechanical workshop at Glasgow University was used. The attenuator, supplied by Newport Limited, consisted of a disc with metal deposited on it. The thickness of this metal varied as a function of angle around the disc. The transmission of this attenuator is illustrated in Figure 4.16, below [4.26]. In order to rotate the attenuator, and hence vary the transmitted intensity, a stepper motor and gearbox

were fitted to the mount, as illustrated in Figure 4.16. The stepper motor was a RS 332-947, 7.5° stepper motor with a RS 336-416 gearbox to reduce the angle of rotation per step from 7.5° to 0.03° [4.21]. This stepper motor is the same model as supplied with the Jobin Yvon HR25 spectrometer and, as in the case of that spectrometer, could be turned by the "Spectralink" with the use of appropriate current limiting resistors (see section 4.4.2). This gearbox allowed a near continuous variation in transmitted intensity as the stepper motor rotated, although if reproducibility of the transmitted intensity with stepper motor position is required the 2° backlash in the stepper motor should be taken into account. This, of course, can be overcome by always approaching the start position from more than 2° away and in the same direction as the measurement rotation direction. The "Spectralink" was capable of recording data from two different detectors simultaneously. This allowed the intensity of the PL emission to be measured, using a photomultiplier tube connected to one of the "Spectralink's" data inputs, simultaneously with the corresponding excitation intensity, of which a fraction was split off using a beam splitter and directed to a power meter. The analogue output of this power meter (proportional to the measured intensity) was connected to the other "Spectralink" data acquisition channel. This allowed the emitted intensity to be measured as a function of the excitation intensity.
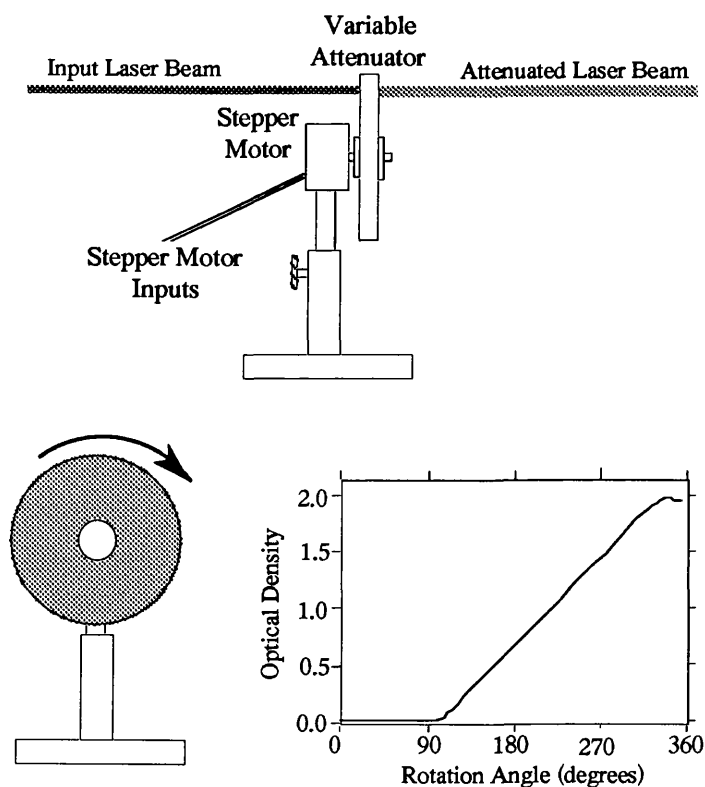
Figure 4.16   Variable attenuator used for intensity variation measurements.

As an alternative to using the "Spectralink" to drive the stepper motor, the circuit shown in Figure 4.17 was constructed. Using this circuit the measured PL intensity (from an analogue

output attached to the photon counting module) and the split off fraction of the excitation intensity, measured by a power meter, could form the inputs to a x-y recorder. This would then plot the PL intensity as a function of excitation intensity while the stepper motor was rotated using the circuit below. This allowed measurements of this sort to be made independently of the "Spectralink". As can be seen in Figure 4.17 the clock input to the stepper motor driver I.C., which produced one step per clock pulse [4.27], was connected to a variable frequency square wave generator. This was an op-amp circuit forming an astable multivibrator, whose frequency of oscillation could be adjusted by altering the value of the variable resistor in the feedback loop. With the component values indicated the frequency of the clock pulses could be varied from 0.5Hz up to 350Hz [4.28]. This (350Hz) corresponds to the maximum rate of rotation of this stepper motor [4.21], allowing the rate of rotation of the variable attenuator to be altered considerably.
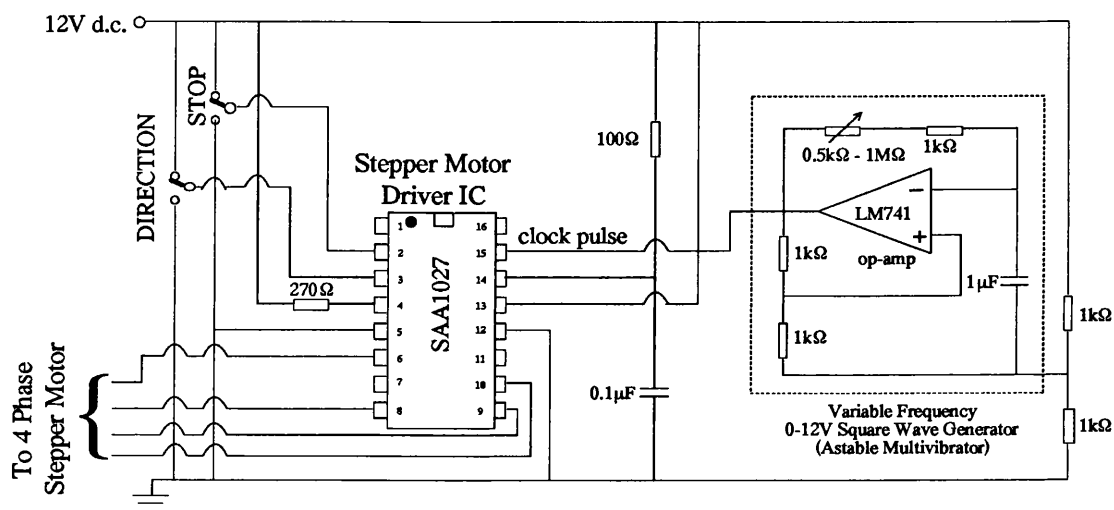
Figure 4.17   Circuit used to rotate the variable attenuator.

4.6 Low Temperature Measurements

Although most of the measurements performed in the work presented here were made at room temperature, it was occasionally found necessary to perform measurements at low temperatures. The low temperature measurements discussed in chapter five were made using the optical cryostat depicted in Figure 4.18, below. This cryostat was produced by Quantum Productions Limited and allowed optical access via inner and outer windows made from Spectrosil WF (water free) glass with a flat spectral response between 250nm and 2μm and a transmission of greater than 80%. The cryostat could be operated in either bath or gas flow

modes. In the bath mode helium was transferred to the sample space from the helium reservoir through a needle valve. It was then pumped to reduce its pressure and temperature below the lambda point, where it became a bubble free superfluid (temperature range 1.8K to 2.1K). In the gas flow mode helium gas was sucked through the needle valve and the temperature of the sample was controlled by balancing this flow against the heat dissipated in an electric heater, allowing the temperature to be varied from 4.2K to 300K, with a temperature stability of ~2K [4.1,4.2]. A Oxford Instruments Model ITC4 temperature controller with sensors attached was used to vary the power dissipated in the heater and hence control the sample temperature.
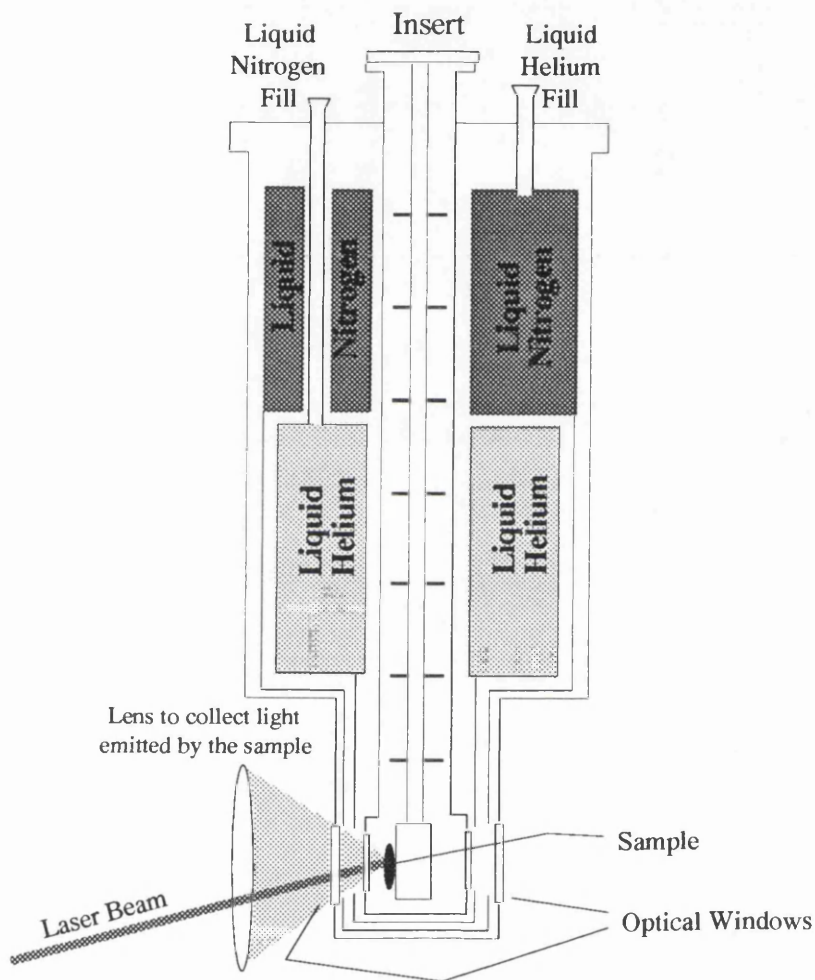
Figure 4.18   Schematic diagram of the optical cryostat used for the low temperature work presented in this thesis.

4.7 Pump Probe Measurements

Figure 4.19, below, illustrates schematically the equipment used for a pump-probe experiment carried out at British Telecom Research Laboratories.
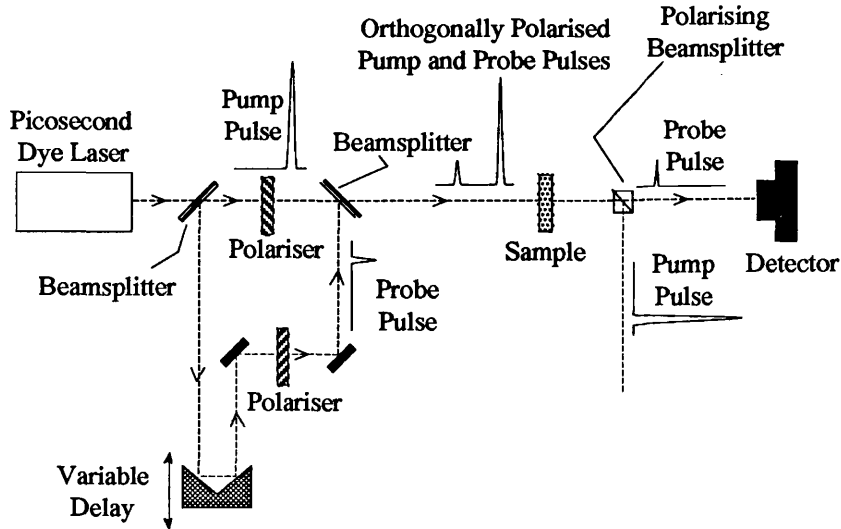
Figure 4.19 Schematic diagram of the pump-probe experiment, used to measure the material's relaxation time after being excited with an intense pump pulse.

As the above diagram illustrates, the pulses (~3ps duration) from the dye laser (pumped by the frequency doubled output of a Nd:YAG laser) are split into a pump pulse and a very much less intense probe pulse (typically a factor of ten lower in power than the pump pulse). The pump and probe pulses are then linearly polarised in orthogonal directions and a delay is introduced causing the probe pulse, when recombined with the pump pulse, to lag behind the high intensity pulse by a variable time period. The pump pulse and the delayed probe pulse, following the same path, are then directed through the sample. The orthogonally polarised pump and probe pulses are then separated and the intensity of the transmitted probe pulse monitored by a power meter. As discussed in chapter five, the intense pump pulse will bring about a partial saturation of the sample's absorption. This saturation will diminish with time until the material returns to its normal absorbing condition. By observing the intensity of the probe pulse transmitted by the sample, as a function of the time delay between it and the pump pulse, a measurement can be made of the relaxation of the material from its excited condition, with a partially saturated absorption, to its equilibrium condition.

Chapter 5 Results and Discussion

In this chapter results will be presented from a variety of optical experiments performed on microcrystallite doped glasses. The absorption, photoluminescence, Raman scattering and carrier relaxation properties of the samples will be related to the fundamental physical parameters of the crystallites, such as their size and stoichiometry.

However, prior to presenting the results of these measurements, it is instructive to consider exactly what these experiments are being performed on. All the experiments carried out for this project probed the combined properties of a very large number of crystallites. These glasses often only contain as little as 0.5% by weight of the semiconductor components. Assuming most of this material to be incorporated into the crystallites this corresponds, for a crystallite diameter of 5nm, to a crystallite density of $\sim 10^{13}/mm^3$. This should be regarded as an upper estimate, since not all the initial dopants will form crystallites. Some will remain as ions within the glass matrix and some of the relatively volatile sulphur and selenium will be lost from the sample during the thermal annealing processes. A typical absorption experiment, with light passing through an area 1mm in diameter of a 100μm thick sample, will measure the properties of possibly as many as 10^{12} crystallites. A typical photoluminescence experiment, with a laser spot size of 0.1mm on the sample and a penetration depth of 0.03mm (corresponding to an absorption coefficient of 300cm^{-1} at the laser wavelength), will measure the emission from $\sim 10^{10}$ crystallites.

For the experiments discussed in this chapter the glass matrix can be considered, to a large extent, as an passive host material[†]. For the wavelengths relevant to these experiments the light emission and absorption of the glass are negligible compared with those of the semiconductor. The optical properties of the glass can also be considered linear compared with the relatively large resonant nonlinearities of the crystallites.

[†] As was discussed in chapter three the host material clearly participates in the diffusive growth process and, as will be discussed in this chapter, the glass/semiconductor interface is often considered to be of relevance in determining the properties of the microcrystallites.

5.1 Determination of Crystallite Stoichiometry from Raman Scattering Measurements

In this section the preparation and Raman scattering properties of crystallites of $CdSe_xS_{1-x}$ will be considered. It will be shown how Raman scattering measurements can be used to estimate the stoichiometry of the embedded crystallites.

5.1.1 Sample Preparation

In this section three samples of $CdSe_xS_{1-x}$ doped glass will be considered. These samples were prepared at British Telecom Research Laboratories, Martlesham Heath by H.P. Girdlestone. The samples were produced from commercially available Hoya filter glasses which were heated to 1100C for 30 minutes then cooled quickly. This, as was explained in chapter three, produces a clear glass containing no crystallites. These glasses were then reheated to a temperature within the crystallite growth regime in order to regrow crystallites, the sizes of which depend upon the crystallite growth temperature and time. Table 5.1 details the Hoya glasses used and the thermal processing they were subjected to in order to produce the final samples.

Sample	Starting Glass	"Clearing"		Nucleation and Growth				Crystallite Diameter
		T	t	T_1	t_1	T_2	t_2	
B1	Hoya O-56	1100C	30 min.	600C	35 min.	750C	10 min.	6.6nm ±1.2nm
B2	Hoya O-58	1100C	30 min.	——	——	675C	30 min.	4.5nm ±0.9nm
B3	Hoya O-58	1100C	30 min.	——	——	650C	60 min.	3.6nm ±0.7nm

Table 5.1 Thermal processing conditions for samples B1, B2 and B3. These were prepared at British Telecom Research Laboratories by H.P. Girdlestone.

Transmission electron microscopy measurements were performed on these samples by K. Moulding of the Physics Department at Essex University, the results of which are also tabulated in Table 5.1. The values following the crystallite sizes represent the estimated precision of the measurement and do not represent the size distribution of the crystallites. The crystallites were found to be hexagonal columns, consistent with a hexagonal wurtzite crystal structure, with a size distribution of approximately 20%.

It should be emphasised that the stoichiometries of the final samples need not necessarily be the same as those of the original Hoya glasses from which they were prepared. As will be discussed later (section 5.9.1) the stoichiometry depends upon the growth conditions as well as the initial concentrations of Cd, Se and S in the original melt.

5.1.2 Raman Scattering Measurements

The Raman scattering spectrum of sample B3 is shown in Figure 5.1, below [‡].
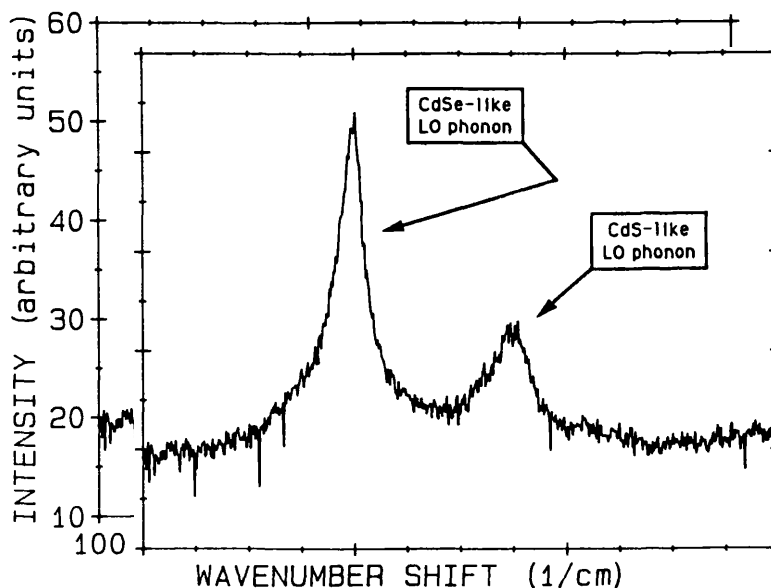
Figure 5.1   Raman spectrum of sample B3 illustrating the CdSe-like and CdS-like LO phonons. The Raman spectra of samples B1 and B2 are similar.

The features present in this spectrum correspond to scattering from CdSe-like ($\sim$200cm^{-1}) and CdS-like ($\sim$275cm^{-1}) zone centre LO phonons. No scattering was observed from TO phonons, although they are often observed in bulk $CdSe_xS_{1-x}$. Possibly such TO phonon scattering is present but too weak to be detected above the quite considerable background emission from the glass host (see the intensity scale in Figure 5.1). The width of the Raman scattering peaks compare well with values from bulk material. This suggests that the particles of $CdSe_xS_{1-x}$ within the glass are crystalline and do not contain a large number of internal defects. Defects limit the phonon's coherence length and result in a broadening of the Raman scattering peaks (see section 2.1.5). The effect of the finite sizes of the crystallites on the width of the Raman scattering peaks will be discussed fully in section 5.10. It is suggested that for these samples the widths of the Raman scattering features result from the inherent width associated with scattering in $CdSe_xS_{1-x}$ (determined by the phonon lifetime) and the phonon's coherence length being limited by the finite sizes of the crystallites rather than by internal defects. Another contributing factor to the width of the phonon peak is stoichiometry variations from crystallite to crystallite within the sample.

[‡] All the Raman spectra presented in this thesis represent the Stokes component of the scattered radiation.

As outlined in section 2.1.5, the position and intensity of the features present in the Raman scattering spectra of $CdSe_xS_{1-x}$ vary as the sulphur to selenium ratio is altered. Figure 5.2, below, illustrates the variation of the CdSe-like and CdS-like zone centre phonon energies as functions of the composition of the ternary material.
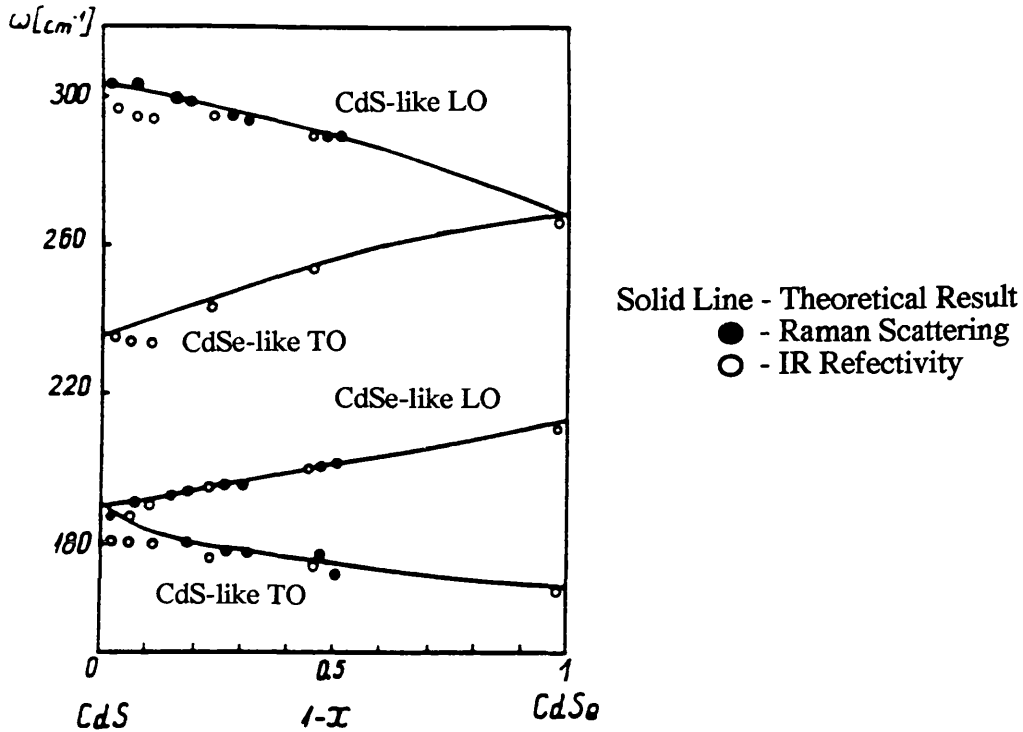
Figure 5.2 Variations of the energies of the CdSe-like and CdS-like LO and TO zone centre phonons with crystal stoichiometry for bulk material [5.1-5.3].

The solid lines in the above figure were calculated for bulk $CdSe_xS_{1-x}$. The full and open circles represent the results of experimental measurements on bulk material made using Raman scattering and infra-red absorption techniques respectively [5.1-5.3]. These curves can be used to determine the stoichiometry of the crystallites from their Raman scattering spectra. Since the absolute positions of the CdSe-like and CdS-like LO phonons also vary with the sizes of the crystallites (see section 2.4), a more acceptable estimate of the crystallite composition can be made by considering the energy difference between the two LO phonons.

Using the phonon separation to determine the composition will be more accurate since both the phonon energies will be shifted by comparable, although not strictly identical, amounts. Differences in the dispersion relations for the CdSe-like and CdS-like LO phonons will cause them to be shifted by slightly different energies as the crystallite size is reduced and will result in inaccuracies in the stoichiometries obtained by this method.

The relative intensities of the LO phonon peaks can also be used to estimate the crystal stoichiometry. The stoichiometries of crystallites can calculated using Equations 5.1, below [5.4,5.5].

$$R = \frac{I(CdS)}{I(CdS) + I(CdSe)} \qquad \textbf{(a)}$$

$$I(CdS) = \frac{I_m(CdS)\ (\omega_L - \omega)}{\omega\ (n(\omega) + 1)} \qquad \textbf{(b)} \qquad \qquad \textbf{Equations 5.1}$$

With a similar expression for I(CdSe)

$$n(\omega) = \frac{1}{\exp\left(\frac{\hbar\omega}{kT}\right) - 1} \qquad \textbf{(c)}$$

where   R = Sulphur content of the crystallites

I_m= Measured intensity of the Raman scattering peak

ω_L= Laser frequency

ω = Frequency shift

$n(\omega)$ = Bose factor

$\hbar$ = (Planck's constant)/2π

k = Boltzmann's constant

T = Temperature

The "intensities" appearing in Equation 5.1(a) are not the actual phonon intensities but rather the phonon intensities multiplied by factors to account for the proximity of the excitation frequency and the phonon density of states (Equations 5.1(b) and 5.1(c)). The stoichiometries determined by this intensity method are tabulated in Table 5.2 along with those determined from the relative positions of the CdS-like and CdSe-like LO phonons.

Sample	Crystallite Diameter	Composition Phonon Energies	Composition Phonon Intensities
B1	6.6nm ±1.2nm	45% ± 5% S	43% ± 4% S
B2	4.5nm ±0.9nm	28% ± 3% S	22% ± 2% S
B3	3.6nm ±0.7nm	31% ± 3% S	23% ± 2% S

Table 5.2   Crystallite compositions for samples B1, B2 and B3 as determined by the relative positions of the LO phonons and their relative intensities.

The estimated errors given in the above table are based on the accuracy of the experimental measurement and not on the intrinsic accuracy of the methods used to determine the stoichiometries. It is in such systematic errors that the discrepancies between the two methods are likely to be found. The method of determining the compositions from the energy differences between the CdSe-like and CdS-like zone centre phonons relies on the assumption

that any shift in the phonon energies, due to their confinement within a finite crystal, will effect both phonons equally. However, as will be discussed in section 5.10.1, the energy of LO phonons in CdS will be shifted (downwards in energy) by a greater amount than the LO phonons in CdSe. The same will apply respectively to the CdS-like and CdSe-like LO phonons in crystallites of $CdSe_xS_{1-x}$. Thus, as the crystallite size is reduced the confinement effect will tend to cause the two phonon peaks to become closer together causing the sulphur content of the crystallites to be overestimated by an increasing amount (see Figure 5.2). As Table 5.2 illustrates this is observed experimentally, with the energy difference method of determining the stoichiometry overestimating the sulphur content, compared with the intensity method of estimating the composition, by an increasing amount as the crystallite size is reduced. It should be remembered that the intensity method of determining the stoichiometry is free from this systematic error and will, therefore, be used in preference to the energy method to determine crystallite stoichiometries in subsequent sections. Thus, Table 5.2 presents some evidence for phonon confinement in three dimensions, which will be the subject of section 5.10.

It is also evident from Table 5.2 that samples B2 and B3 are of approximately the same stoichiometries while sample B1 contains considerably more sulphur. This is as expected since samples B2 and B3 were prepared from the same Hoya glass while sample B1 was prepared from Hoya glass with an absorption edge at a lower wavelength (the numbers "56" and "58" in the glass names "O-56" and "O-58" refer to the onset of significant absorption occurring at around 560nm and 580nm respectively, see Table 5.1) corresponding to a greater sulphur content (see Equation 2.1 in chapter two). However, it should be emphasised that the doping of the initial glass is not the only factor which influences the final stoichiometries of the crystallites (this will be discussed in section 5.9.1).

5.2 Absorption and Photoluminescence Measurements

Figure 5.3 illustrates the room temperature absorption and photoluminescence spectra of the three samples discussed above[§].

[§] All the measurements presented in this thesis, unless otherwise stated, were performed at room temperature. Other parameters, such as the excitation wavelength and the previous exposure of the sample to optical radiation, will be given when they are relevant to the discussion.
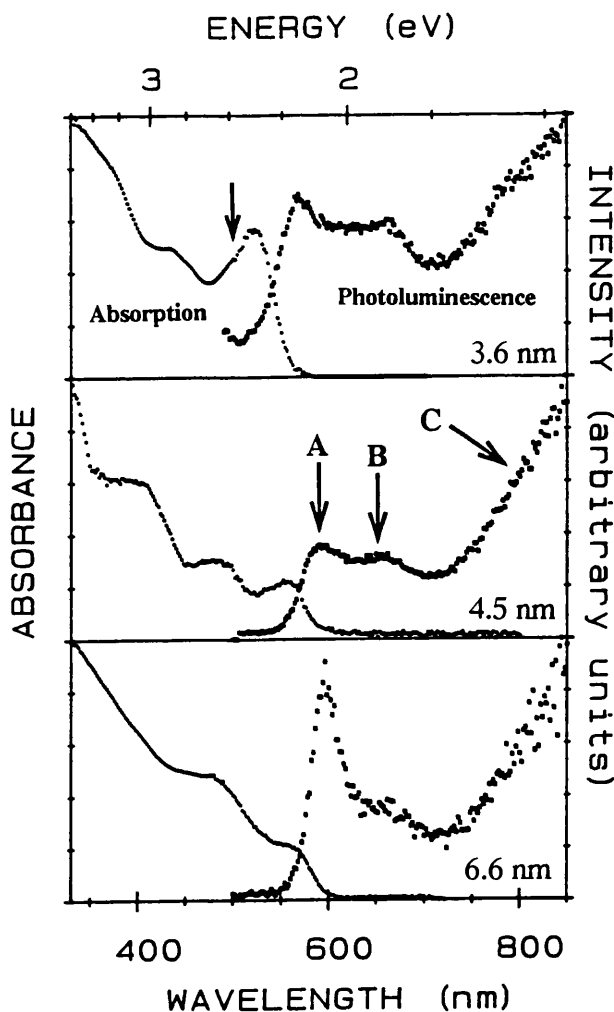
Figure 5.3 Absorption and photoluminescence spectra of samples
B1 (bottom), B2 (middle) and B3 (top).

These spectra have been normalised with respect to the maximum emission intensity for clarity. The photoluminescence spectra have also been corrected for the measured spectral response of the U1000 spectrometer system, the details of which can be found in chapter four.

These figures clearly exhibit the expected increase in absorption edge structure as the sizes of the crystallites are reduced. All three samples illustrate absorption edge structure associated with the lowest bound energy states of the carriers, with samples B2 and B3 showing clear evidence of higher energy bound states. The absorption spectrum of sample B3 also illustrates a shoulder (indicated by the arrow) on the high energy side of the prominent peak similar to that observed by Borrelli et al [5.6], who attribute it to spin-orbit splitting of the valence band.

The photoluminescence spectra illustrate two or possibly three distinct features (A, B and C in Figure 5.3). The high energy feature, A, is similar to that observed by several researchers investigating materials of this type and two possible recombination routes have been suggested to explain this peak.

(i) Recombination via impurity or defect states lying close to the conduction or valence band edges. This peak, as has been observed by several research groups, will be shifted to higher energies as the crystallite size is reduced because defects or impurities, whose effect in bulk

material extends over a range significant compared to the crystallite radius, will also experience a "quantum confinement" within the quantum dot. This is illustrated schematically in Figure 5.4, below [5.6-5.10].
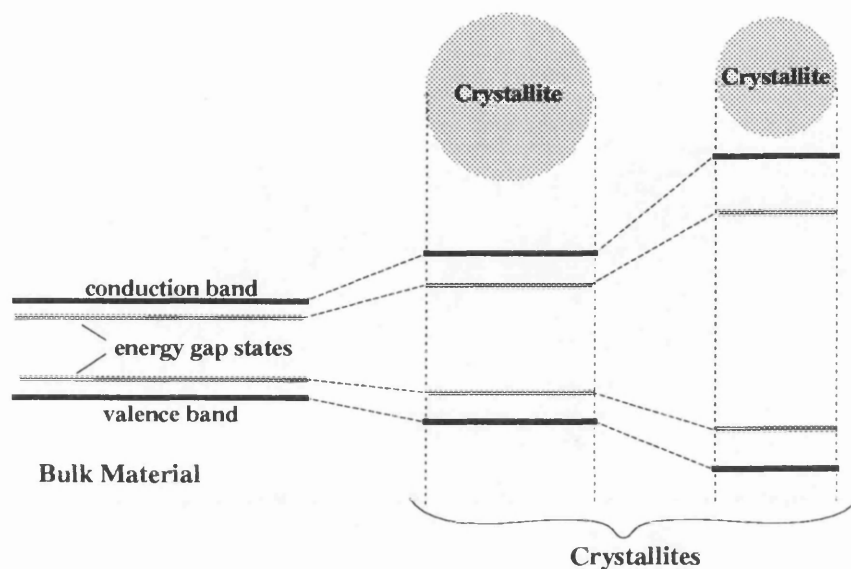
Figure 5.4   Schematic illustration of the energy levels in a crystallite as its size is reduced.

Although this peak may not represent "band to band" carrier recombination its position can still be used to study quantum confinement effects and it at least allows samples to be arranged according to the relative sizes of the crystallites they contain.

(ii) "Band to Band Recombination". This high energy peak has also been attributed, by some researchers, to direct electron-hole recombination between the lowest electron bound state and the highest hole bound state (see for example [5.1,5.9,5.11-5.15]). If this explanation is to be considered correct the large Stokes shift between this peak and the associated absorption edge feature must be explained. The Stokes shifts for the samples considered here are tabulated in Table 5.3, below.

Sample	Crystallite Diameter	Stoke's Shift
B1	6.6nm ±1.2nm	100meV
B2	4.5nm ±0.9nm	130meV
B3	3.6nm ±0.7nm	180meV

Table 5.3   Stokes shifts for samples B1, B2 and B3.

As can be seen from Table 5.3, the Stokes shifts are large compared with the LO phonon energy of ~40meV (the zone centre LO phonon energy in CdS, see Figure 5.2), requiring a

strong coupling between the lattice and the electronic states if the energy differences are to be accounted for by the emission of optical phonons. The Stokes shift also increases as the crystallite sizes are reduced. Uhrig et al [5.13,5.14] observed absorption and photoluminescence features very similar to those displayed in Figure 5.3 and attributed the large Stokes shifts to an enhanced coupling between the electronic states and the vibrational states of the lattice, which increases as the crystallite sizes are reduced. They measured this coupling and found it, together with its dependence on crystallite size, to be consistent with the observed Stokes shifts, justifying the association of feature A with direct electron-hole recombination. If this explanation is correct then emission band A corresponds to "band to band" transitions involving different numbers of phonons. These separate emission peaks are each Stokes shifted by a different number of phonon energies from the "band to band" transition energy but are not resolved due to homogeneous and inhomogeneous broadening and merge into a wide band. Of course, an increase in the shift between emission peak A and the lowest energy absorption feature as the crystallite size is reduced is also consistent with band A being associated with impurity/defect states (see Figure 5.4). If such an enhanced electron-phonon coupling exists between electronic and vibrational states, it would be expected that thermal broadening would increase with decreasing crystallite size. Uhrig et al measured a thermal broadening parameter for crystallites of different sizes and report such a size dependence.

Features similar to B and C in Figure 5.3 have also been observed by other researchers in $CdSe_xS_{1-x}$ doped glasses. It is not known whether B and C are of the same origin. It has been suggested that such low energy emissions, which are not observed to the same degree in bulk material, may be associated with surface related states (see [5.9,5.11,5.12]). These emission bands are generally stronger with respect to band A for smaller samples with a larger surface to volume ratio, which is consistent with the above interpretation. This will be discussed further in section 5.3 when the intensity dependence of the photoluminescence spectra will be investigated.

5.3 Intensity Dependence of Photoluminescence

The relative intensities of the features present in the photoluminescence spectra discussed above were found to be dependent upon the intensity of the light being used to excite the sample. Figure 5.5 illustrates the photoluminescence spectra of samples B1 (6.6nm diameter crystallites) and B3 (3.6nm diameter crystallites) as the intensity of the excitation light is varied.
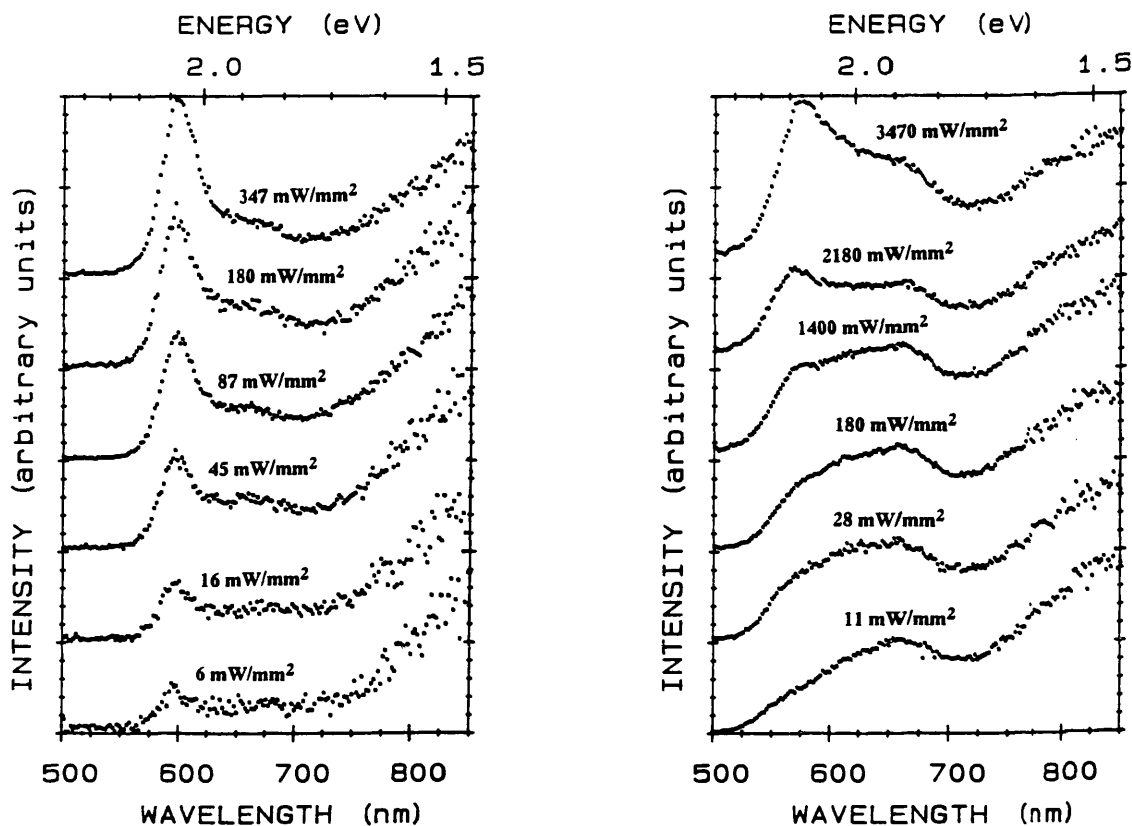
Figure 5.5 Photoluminescence spectra of sample B1 (left) containing 6.6nm diameter crystallites and sample B3 (right) containing 3.6nm diameter crystallites.

At low excitation intensities peak A (see Figure 5.3) is comparable in intensity with the lower energy emissions, while at higher excitation intensities peak A becomes more prominent relative to these lower energy emissions. This intensity dependence is attributed to a saturation of states within the effective energy gap of the crystallites as the excitation intensity is increased [5.16]. The carrier recombination routes involved are illustrated schematically in Figure 5.6, below.
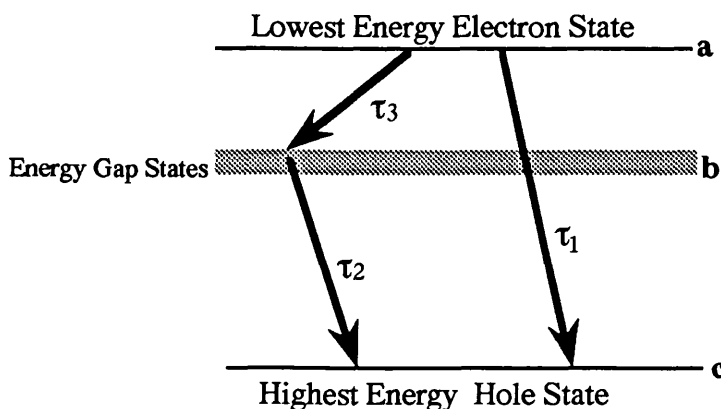
Figure 5.6 Schematic illustration of recombination mechanisms in a microcrystallite.

Of course, state **b** in the case of the samples being considered here should be a continuum of states to represent the broad low energy luminescence of Figure 5.5, but for simplicity it has been displayed as a discrete state. In this schematic model the time constants associated with the transitions (τ_1, τ_2 and τ_3) would be such that $\tau_3 < \tau_1 < \tau_2$. Under these circumstances, at low excitation intensities excited electrons in state **a** will be rapidly trapped by state **b** from which they will, after a relatively long period τ_2, make a transition to state **c**. Provided the excitation intensity is sufficiently low state **b** will remain relatively unoccupied and most carriers will recombine via this relatively slow two stage process, with the fast trapping time of state **b** preventing carriers recombining directly from state **a** to state **c**. However, under higher excitation conditions state **b** will become saturated and transitions to this state will be prevented by the exclusion principle causing more electrons to make the transition directly from state **a** to state **c**. In this model state **a** would represent either the lowest electron bound state or an impurity/defect state depending upon the origin of spectral feature A (see the discussion in section 5.2 and Figure 5.3). This description of the carrier recombination processes within microcrystallites will be considered further in section 5.6, when the carrier relaxation times are measured by a pump-probe experiment.

As can be seen from Figure 5.5 it becomes considerable more difficult to saturate the states corresponding to the low energy emissions (B and C in Figure 5.3) as the crystallite sizes are reduced. This size dependence indicates a greater density of these states within the effective energy gap for the smaller crystallites, possibly suggesting that they are surface related or that smaller crystallites contain a greater number of internal defects. Alternatively, this might also suggest that the relative magnitudes of the recombination times illustrated in Figure 5.6 are dependent upon the crystallite sizes with, for example, τ_1 increasing relative to τ_2 as the crystallite sizes are reduced. The effect of stoichiometry on the relative intensities of these spectral features will be considered in section 5.5.

5.4 Temperature Dependence of Photoluminescence

The relative intensities of the spectral features, A, B and C, were also found to dependent upon the sample temperature. Figure 5.7, below, illustrates the photoluminescence from sample B2 at a constant excitation intensity of ~100mW/mm^2 as the sample temperature is varied. Spectral feature A is less prominent in these spectra because of the relatively low excitation intensity chosen (see section 5.3). A low excitation intensity was chosen in order to minimise an "irreversible" light induced change in the light emitting properties of the microcrystallites, which will be discussed further in section 5.7.
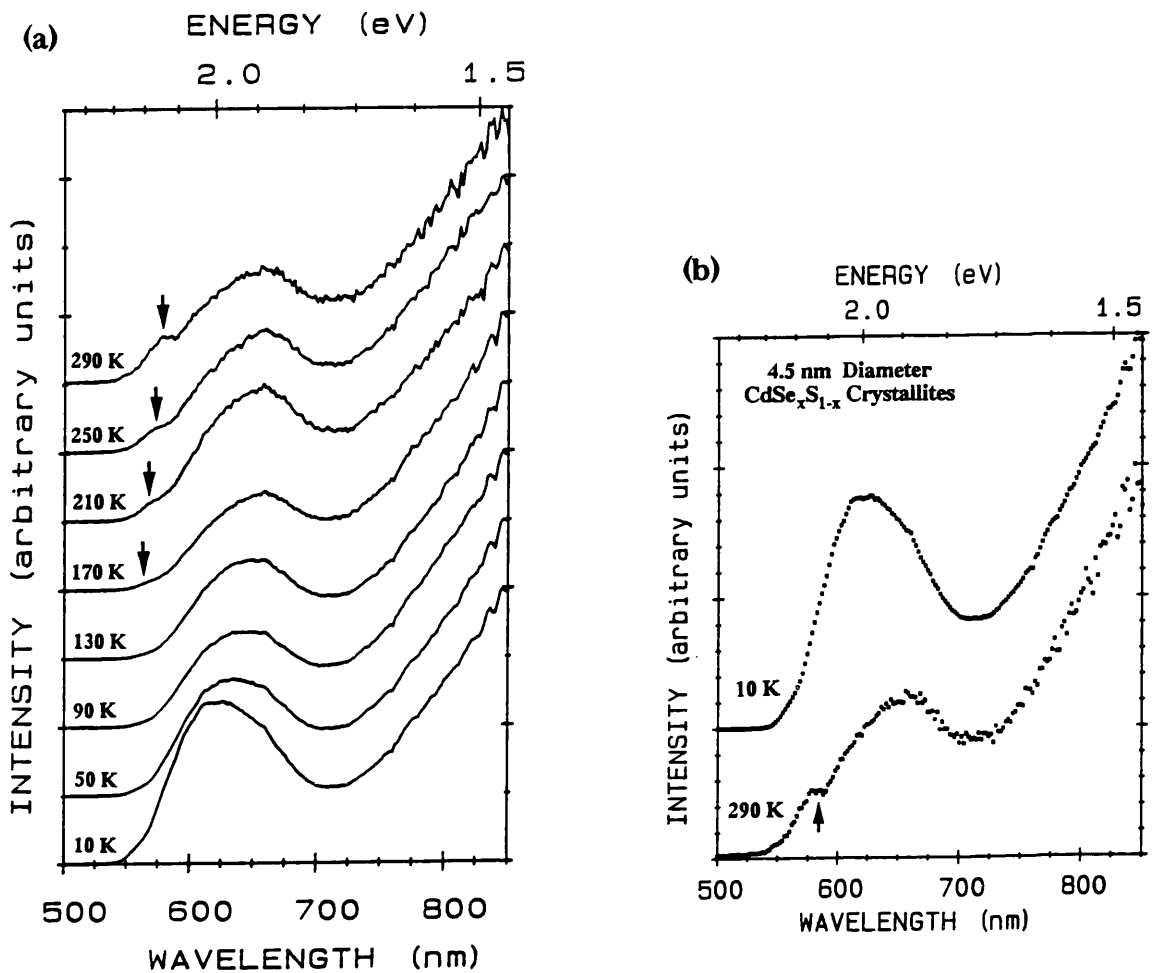
Figure 5.7 **(a)** Temperature dependence of the photoluminescence from sample B2.
(b) More detailed comparison of the low temperature and near room temperature emission from sample B2.

As can be seen from the above diagrams, the high energy spectral feature, A, becomes more prominent as the sample temperature is increased. This, it is suggested, results from carriers trapped in the energy gap states (modelled as **b** in Figure 5.6) being thermally excited out of these states into state **a** (see Figure 5.6) at higher temperatures, thus increasing the probability of a "direct" **a** to **c** transition at such temperatures [5.17]. It should be remembered that for microcrystallites state **b** represents a continuum allowing this thermal excitation to occur via numerous small increases of energy. The greater prominence of this interesting spectral feature at higher temperatures is why several experiments whose results are presented in this thesis were performed at room temperature rather than at cryogenic temperatures.

5.5 Stoichiometry Dependence of Photoluminescence

Figure 5.8, below, illustrates the Raman spectra and photoluminescence spectra of commercially available Schott filter glasses GG495 and RG695. The selenium fractions estimated from the Raman spectra (see section 5.1) are 100% (only a LO phonon typical of CdSe was observable), for RG695, and 27% ±2%, for GG495.
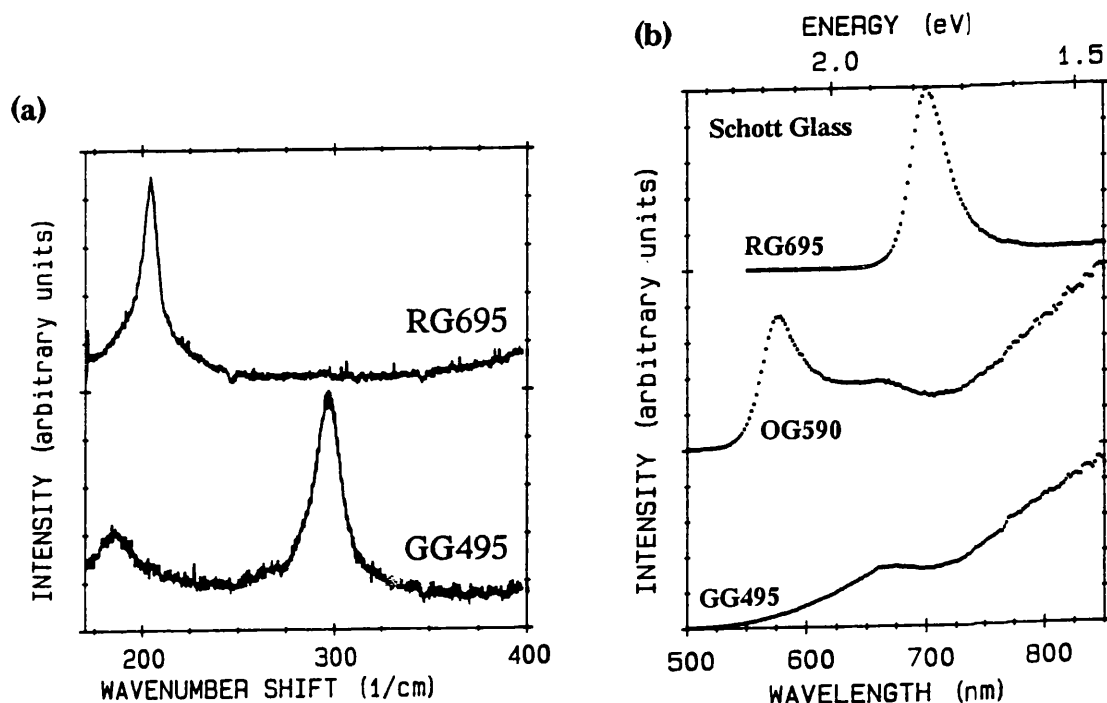
Figure 5.8 (a) Raman spectra from "as bought" Schott filter glasses RG695 and GG495.
(b) Photoluminescence spectra (room temperature) of "as bought" Schott filter glasses RG695, OG590 and GG495.

As can be seen from this figure, the low energy luminescence becomes more prominent as the sulphur content of the crystallites is increased (ie from top to bottom in Figure 5.8(b)). The following are suggested as possible explanations of this observation.

(i) The defects or impurities responsible for the low energy luminescence are particularly associated with sulphur.

(ii) If the low energy luminescence is associated with surface states, Figure 5.8 might indicate a reduction in the quality of the glass/semiconductor interface as increasing amounts of sulphur are incorporated into the crystallites.

(iii) The recombination times indicated in Figure 5.6 vary as the sulphur to selenium ratio of the crystallites is altered. The results of Figure 5.8 could be explained if, for example, τ_1 were

to increase relative to τ_2 as the sulphur content of the crystallites is increased.

It should be mentioned that the above observation is not a result of variations in the absorption edges of the crystallites, relative to the excitation wavelength, as their sulphur content is altered. This was eliminated as an explanation by altering the excitation wavelength (see section 4.2.1).

5.6 Carrier Relaxation in Quantum Dots

Electron and hole recombination times were investigated using a pump-probe experiment (see section 4.7) where an intense "pump pulse" from a picosecond laser system partially saturates the absorption of a sample of microcrystallite doped glass. This partially "bleached" absorption is then probed some variable time later by a much less intense probe pulse. In the following figures the transmission of the probe pulse is displayed as a function of the delay time between this probe pulse and the preceding pump pulse. The peak change in transmission indicated beside each curve is the maximum change (reduction) in transmission normalised with respect to the linear transmission of the material at the pump and probe wavelength.

Figure 5.9, below, illustrates the carrier relaxation of sample B1 (see section 5.2) containing 6.6nm diameter crystallites with an estimated selenium fraction of 0.6. As can be seen from this figure there are two quite distinct components within the carrier relaxation: a rapid component, of ~20ps, and a much longer component, of ~800ps.
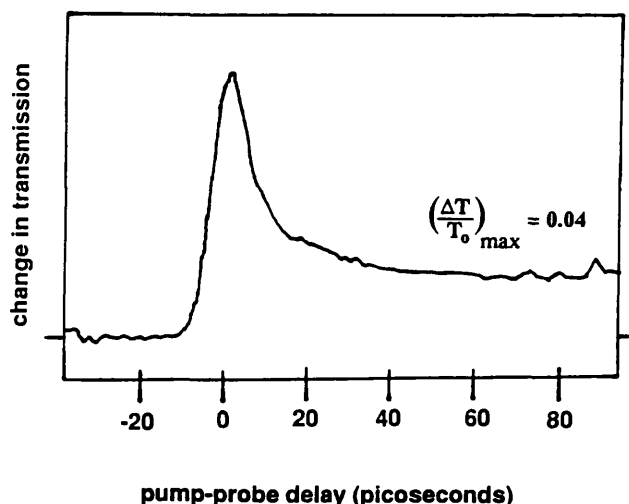
Figure 5.9   Relaxation of the saturated absorption of sample B1.

The slower relaxation component for this sample is illustrated in Figure 5.10, below.

91
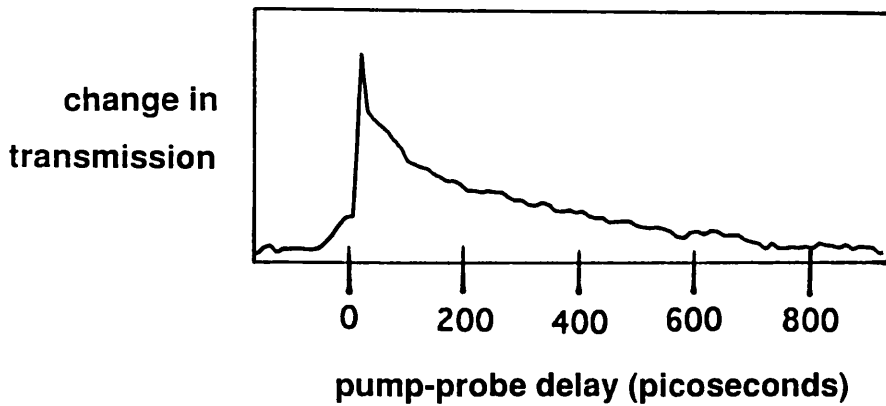
Figure 5.10 Slow component of the relaxation of the saturated absorption of sample B1.

Two suggestions are offered to explain this two component relaxation:-

(i) That the rapid relaxation component results from direct recombination between states **a** and **c** in Figure 5.6. This corresponds to either direct band to band recombination or recombination via impurity or defect states with a quite well defined energy near the conduction or valence band (see the discussion in section 5.2). The slow component is attributed to recombination via the continuum of defect/impurity states represented by state **b** in Figure 5.6. It has been suggested that the confinement of electrons and holes in microcrystallites can reduce the direct electron-hole recombination time below that of the corresponding bulk material by, for example, increasing the overlap of the electron and hole wavefunctions [5.11].

(ii) That the rapid relaxation component results from nonradiative Auger recombination whereby the carriers recombine by transferring their energy to another carrier (see, for example, [5.15,5.18]).

The carrier relaxation depicted above was found to be dependent upon both the intensity and wavelength of the pump pulse. The intensity dependence is illustrated in Figure 5.11, below. As can be seen from this diagram, the rapid relaxation component becomes more pronounced relative to the slow component. as the excitation intensity is increased.
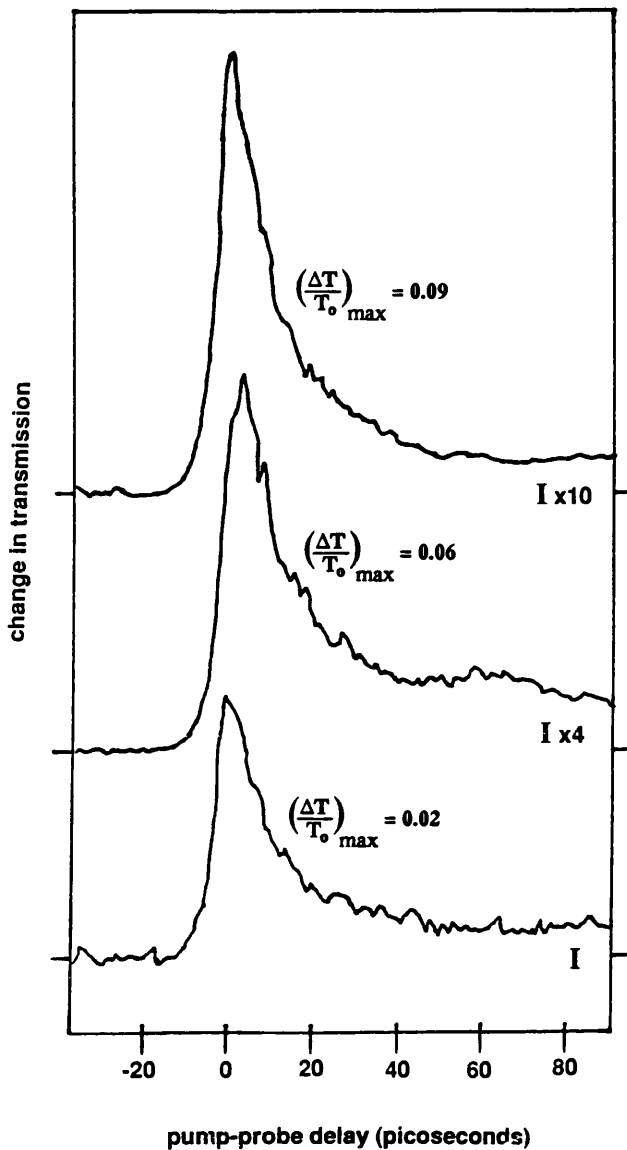
Figure 5.11   Intensity dependence of the relaxation of the saturated
absorption in sample B1.

Again two possible suggestions are offered to explain this intensity dependence.

(i) This intensity dependence can be explained with reference to the carrier recombination processes illustrated schematically in Figure 5.6. At low intensities the recombination is via long lived trap-like states within the energy gap which trap the carriers for a relatively long period resulting in a slow carrier relaxation. At higher intensities these states are saturated increasing the probability of the faster more "direct" recombination route being dominant.

(ii) The higher intensity excitation pulses promote the faster non-radiative Auger recombination and hence the rapid relaxation component becomes more dominant at these intensities.

The wavelength dependence of the material's relaxation is shown in Figure 5.12, below.
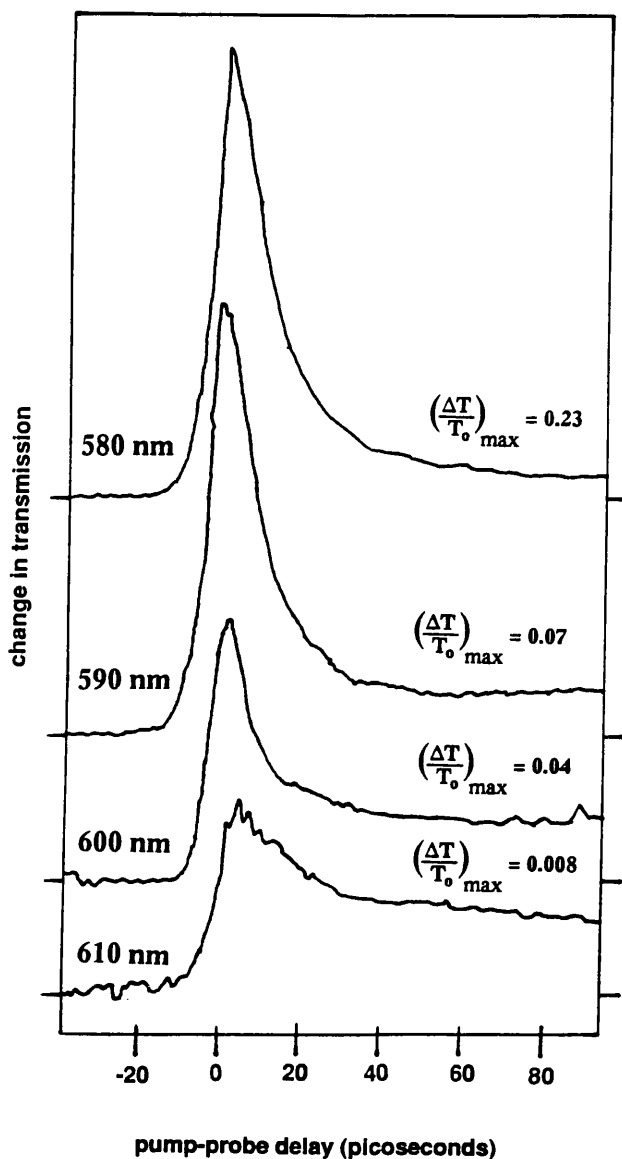
Figure 5.12 Wavelength dependence of the relaxation of the saturated absorption in sample B1.

This wavelength dependence is attributed to the same physical phenomena as the intensity dependence discussed above. As the pump/probe wavelength is decreased the pump pulses are absorbed more strongly by the sample producing an effect similar to that brought about by increasing the intensity of the pump pulse (ie an increase in the prominence of the rapid relaxation component relative to the slow component).

5.7 Photodarkening

An interesting, although, for experimentalists, a sometimes infuriating, property of microcrystallite doped glasses occurs when the material is exposed to quite intense laser radiation. Under such excitation conditions the light emitting efficiency of the material is reduced and occasionally a visible darkening in the colour of the material can be observed (hence the term "photodarkening"). In this section the consequences of this photodarkening for

the light emission spectra and carrier relaxation properties of microcrystallites in glass will be discussed.

5.7.1 Photodarkening - Effects on Light Emission

Figure 5.13, below, illustrates the photoluminescence spectra of sample B1 in a "fresh", unphotodarkened, condition and in a photodarkened condition.
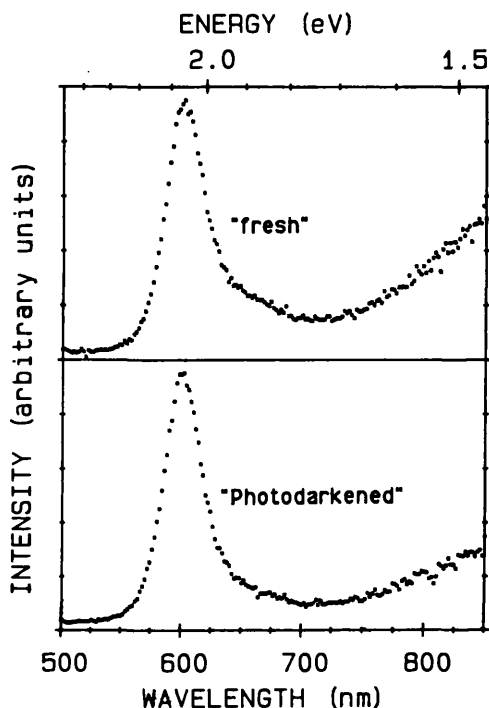
Figure 5.13   Room temperature photoluminescence of sample B1 in a "fresh" and photodarkened condition.

The photodarkening depicted in the above figure was largely produced by exposing the excited area of the sample to an intensity of ~800mW/mm^2 for a period of 30 minutes, although a relatively small amount of photodarkening occurred during the course of the measurements. The light induced photoluminescence change was found to be "irreversible" in the sense that the spectrum from a photodarkened portion of the material, left unexposed to further laser radiation, does not, over the course of at least a day, at room temperature, revert to that of "fresh" material. For the degree of photodarkening illustrated in Figure 5.13 (both spectra are plotted to the same intensity scale) the result is a reduction in the intensity of the low energy emission (the continuum corresponding to the transitions a-b-c in Figure 5.6) with negligible effect on the states responsible for the high energy emission peak (transition a-c in Figure 5.6). For spectra illustrating more extreme photodarkening a relatively small reduction in the strength of the high energy emission peak is observed but with a much larger reduction in the intensity of the lower energy emissions.

From these measurements, which illustrate the strength of the various radiative recombination routes, the probability of transitions involving the continuum-like defect/surface states is

greatly reduced by photodarkening while the probability of the more direct recombination process is reduced to a much lesser extent.

5.7.2 Photodarkening - Effects on Carrier Relaxation

Figure 5.14, below, illustrates the carrier relaxation of sample B1, as measured using a pump-probe experiment, in a "fresh" and photodarkened condition.
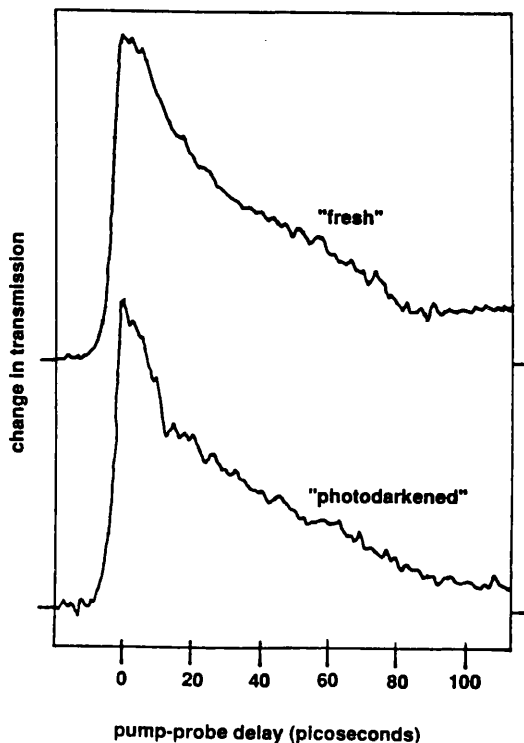
Figure 5.14   Relaxation of the saturated absorption of sample B1 in a "fresh" and photodarkened condition.

The above sample was photodarkened by exposure to laser pulses of wavelength 580nm, duration ~3ps and energy 200pJ. At this intensity the material reached a fully photodarkened state after a few seconds exposure to the laser radiation. In this fully photodarkened state further exposure to the laser beam produced no additional change in the material's relaxation properties. When exposed to lower intensity continuous wave laser radiation the material was not found to reach such a fully photodarkened condition even after several hours exposure (see section 5.7.1). As illustrated in the above figure, photodarkening has two clear effects on the material's pump/probe response:-

(i) The prominence of the slow relaxation component is reduced significantly in relation to the faster component.

(ii) The overall magnitude of the peak absorption change brought about by the pump pulse

(ΔT) is reduced from (ΔT/T_o)=0.18 to (ΔT/T_o)=0.09. The reduction in the magnitude of the transmission change can be attributed to the reduction of the importance of the slow relaxation component. With this slow component of less importance it is more difficult to saturate the absorption of the material since, overall, the carriers are recombining by the faster process.

This can be compared with the photoluminescence spectra illustrated in Figure 5.13, possibly suggesting that the slow relaxation component is associated with the low energy luminescence and hence with the continuum of energy states within the energy gap of the crystallites and that possibly the faster component is associated with the more direct radiative recombination process, transition **a-c**. It has been suggested that photodarkening results from the photoformation of Cd^{2+} within the crystallites which act as recombination centres [5.19] or that it results from electrons, or holes, being trapped at impurity or defect sites [5.15]. It has also been suggested that it results from ionisation of the crystallites, with electrons being trapped in the surrounding glass. With this description the reduced recombination time arises from the presence of extra holes within the ionised crystallites, which promote nonradiative Auger recombination [5.20] (see also [5.21,5.22]).

5.8 Photoluminescence Excitation Spectroscopy

This experimental arrangement (see section 4.4) was constructed to test the feasibility of using photoluminescence excitation spectroscopy to characterise samples of semiconductor doped glass. Such a technique would be useful in allowing an absorption type measurement to be performed on poor quality samples of semiconductor doped glass which at times are not sufficiently robust to survive mechanical thinning and polishing. Although absorption spectroscopy was discussed in chapter two no mention was made of the related technique of photoluminescence excitation spectroscopy. The principles underlying this type of measurement will therefore be briefly outlined below.

5.8.1 Principles of Photoluminescence Excitation Spectroscopy

When a material is excited with light of a short wavelength and emits light at a longer wavelength several transitions are involved. These are illustrated schematically in Figure 5.15, below.

P_{abs} = Probability of absorption of excitation light

$P_{\alpha \rightarrow \beta}$ = Probability of a transition from α to β

$P^{rad}_{\beta \rightarrow \gamma}$ = Probability of a radiative transition from β to γ

λ_{excite} = Variable wavelength excitation
λ_{emit} = Wavelength at which luminescence is observed
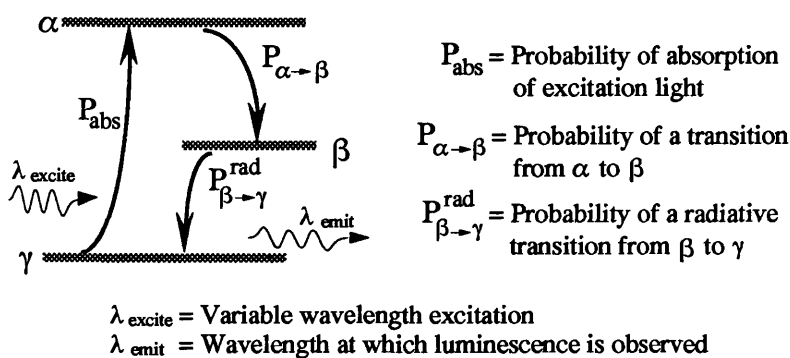
Figure 5.15   Schematic diagram illustrating the processes involved in photoluminescence excitation spectroscopy.

The probability of light being emitted at wavelength λ_{emit}, and hence the intensity of the emitted light, depends upon the probability of a photon of wavelength λ_{excite} being absorbed, the probability of the electron making a transition from state α to state β and the probability of a radiative transition from state β to state γ. Since the probability of the excitation light (λ_{excite}) being absorbed depends upon the material's absorption coefficient at that wavelength, any spectrum which illustrates the intensity of the emission at wavelength λ_{emit} as a function of the wavelength of the excitation light will take a form which, in part, reflects the variation of the material's absorption coefficient with wavelength. This spectrum will also reflect any wavelength dependence of the two transition probabilities mentioned above. This qualitative result is expressed mathematically in Equation 5.2, below, in which the two transition probabilities are combined and expressed as the material's radiative quantum efficiency [5.23].

$$\frac{I_L}{I_0(\lambda)} = Q\left(1 - \exp\left(- \alpha(\lambda)\, a\right)\right) \qquad \textbf{Equation 5.2(a)}$$

In the low absorbing region   In the high absorbing region

$$\frac{I_L}{I_0(\lambda)} \approx Q\, \alpha(\lambda)\, a \quad \textbf{Equation 5.2(b)} \qquad\qquad \frac{I_L}{I_0(\lambda)} \approx Q \quad \textbf{Equation 5.2(c)}$$

where I_L = Emitted intensity
$I_0(\lambda)$ = Intensity of the excitation light
$\alpha(\lambda)$ = Absorption coefficient
Q = Luminescence quantum efficiency
a = Sample thickness

The photoluminescence excitation spectrum will only match the absorption spectrum closely at low absorption levels and when the material's quantum efficiency is independent of wavelength. However, even if these conditions do not apply such a spectrum will still in part reflect the absorption edge of the material and many of the features present in its absorption spectrum.

Figure 5.16, below, illustrates the photoluminescence excitation (PLE) spectrum of a sample of $CdSe_xS_{1-x}$ doped glass containing crystallites 4.5nm in diameter with a selenium fraction of 80% (ie equivalent to sample B2 in section 5.1.1, see Table 5.2).
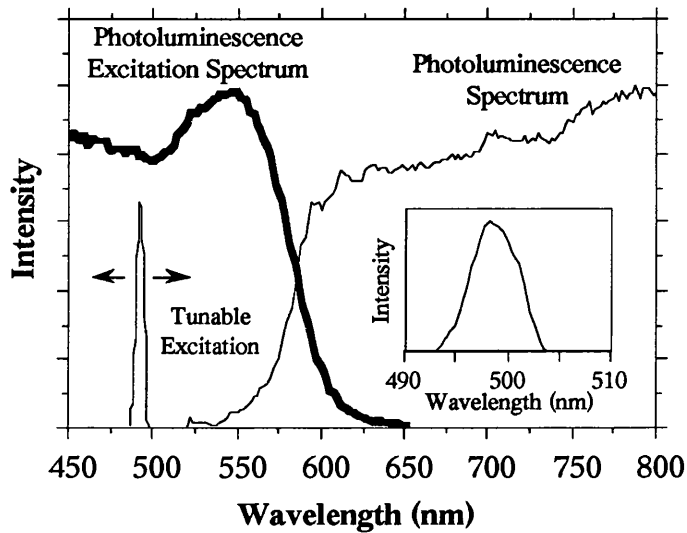
Figure 5.16   Photoluminescence excitation spectrum and photoluminescence spectum of a sample equivalent to sample B2. Also illustrated is a typical spectrum of the excitation source on an identical and expanded scale (inset).

The PLE spectrum represents the emitted light (at 750nm) normalised with respect to the intensity of the excitation source as a function of wavelength (see Figure 4.9(d)). The above figure also illustrates the photoluminescence spectrum of this sample which was obtained by exciting the sample with light from the lamp/spectrometer system of wavelength 500nm and full bandwidth ~5nm. The photoluminescence spectrum has been corrected for the spectral response of the THR1000 spectrometer system (see Figure 4.15).

The PLE spectrum illustrates a clear feature which corresponds well with the lowest energy feature present in the absorption spectrum (see Figure 5.3). There is also the expected qualitative relationship between the positions of the PL and PLE spectra. The photoluminescence spectrum does not posses the high energy peak (A in Figure 5.3). This, considering the low power of the excitation source (see Figure 4.9(d)), is as expected. It is also this low power which makes the normalisation of the PLE spectrum with respect to the excitation intensity, as a function of wavelength, reasonable. At low excitation intensities the light emitted at the observation wavelength, 750nm, was found to vary linearly with wavelength (see section 4.5) justifying this normalisation. At higher excitation intensities the photoluminescence from semiconductor doped glasses clearly varies nonlinearly with the excitation intensity (see section 5.3).

5.9 Sample Preparation Study

For the series of experiments discussed in section 5.10 it was considered of importance to study the effects of crystallite size variation while maintaining the crystallite stoichiometry as constant as possible. A series of experiments was therefore undertaken to study the effects of growth temperature and other parameters on crystallite size and stoichiometry. The samples studied were prepared at Glasgow University from commercially available Schott filter glasses. Figure 5.17, below, illustrates typical transmission characteristics of the series of Schott filter glasses which contain crystallites of $CdSe_xS_{1-x}$ [5.24].
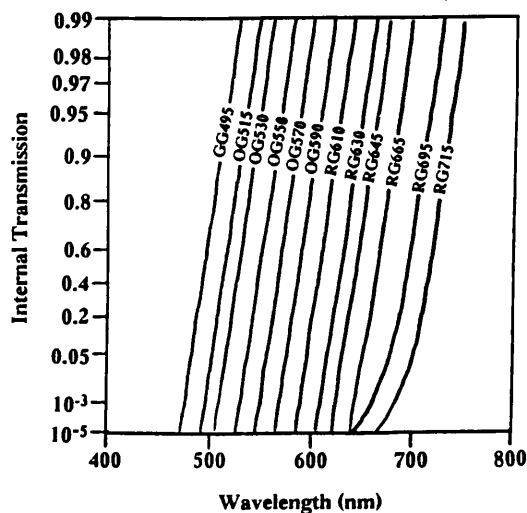
Figure 5.17   Internal transmission characteristics of commercially available Schott filter glasses containing CdSeS crystallites [5.24].

In the above diagram the glasses GG495 to RG715 are cadmium selenium sulphide doped glasses with varying selenium content (see in section 5.5).

5.9.1 Dependence of Stoichiometry on Crystallite Growth Temperature

For this investigation Schott filter glass of type OG590, from a single batch, was used as a starting material. The samples were first heated to 1150C for 30 minutes then cooled rapidly to room temperature, by removing them quickly from the furnace, in order to clear the material of crystallites (see chapter three). This was followed by a subsequent annealing stage during which the crystallites were reformed. The heat treatment parameters are detailed in Table 5.4, below.

Sample	Starting Glass	"Clearing"		Nucleation and Growth	
		T	t	T	t
S1	Schott OG590	1150C	30 min.	675C	24 hr.
S2	Schott OG590	1150C	30 min.	663C	24hr.
S3	Schott OG590	1150C	30 min.	650C	24 hr.

Table 5.4 Preparation conditions for samples S1, S2 and S3. Prepared to investigate stoichiometry variations between samples.

It should be mentioned that small quantities (~5%) of a borosilicate glass were added to the Schott glass melt for the samples considered in this thesis. This was found to decrease the time period necessary to nucleate and grow crystallites. Without this addition significant nucleation/growth required several days annealing for Schott glass (compare this with the nucleation/growth period of minutes/hours required for the Hoya glasses of section 5.1 and Corning glasses [5.6]). It is likely that the borosilicate glass provides an impurity which acts as a centre around which particles of $CdSe_xS_{1-x}$ have a greater probability of nucleating and growing. Such an impurity is presumably present in Hoya glasses in greater concentrations than in Schott glasses (see the growth periods in Tables 5.1 and 5.4).

The stoichiometries of the samples were then determined using Raman scattering. Figure 5.18, below, illustrates the Raman spectra for these samples.
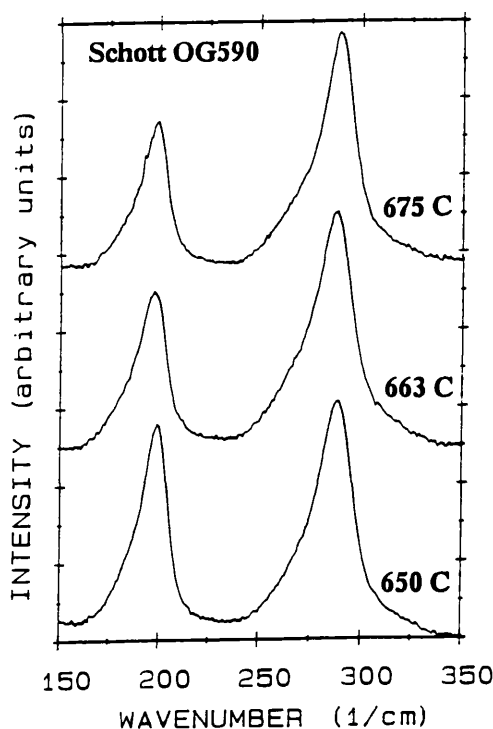
Figure 5.18 Raman spectra of samples with crystallites grown at 650C (bottom), 663C (middle) and 675C (top).

As can be seen from the above diagram, the CdSe-like LO phonon becomes more pronounced as the crystallite growth temperature is reduced indicating the presence of crystallites with an increasing selenium content. The sulphur fractions as determined by Raman scattering for these samples are tabulated in Table 5.5, below.

Sample	Growth Temperature	Composition
S1	675C	57% ± 1% S
S2	663C	55% ± 1% S
S3	650C	48% ± 1% S

Table 5.5   Compositions of samples prepared at different temperatures.

Factors which influence the stoichiometry of crystallites within semiconductor doped glass include:-

(i) The diffusion coefficients of the crystallite components.
(ii) The volatility of the crystallite components.
(iii) The stability of the crystallites as a function of stoichiometry.

(i) Assuming that the diffusion process is characterised by an activation energy the diffusion coefficients of selenium and sulphur will be given by Equation 5.3 [5.25].

$$D = D_o \exp\left(-\frac{Q}{kT}\right) \quad \textbf{Equation 5.3}$$

where D = Diffusion coefficient
D_o = Constant
Q = Activation energy
k = Boltzmann's constant
T = Absolute temperature

Since selenium ions are considerably more massive than sulphur ions it would be expected that the activation energy of selenium (Q_{Se}) would be greater than that for sulphur (Q_S). Under these circumstances the diffusion coefficient for selenium will increase relative to that of sulphur as the sample temperature is increased. Thus, this effect would increase the probability of selenium being incorporated into a crystallite in preference to sulphur as the material's temperature is increased. The experimental observations indicate a reduced selenium fraction as the crystallite growth temperature is increased, suggesting that variations of the diffusion coefficients with temperature is not the dominant physical process.

(ii) The boiling points of selenium and sulphur are 685C and 445C respectively. It would, therefore, be expected that as the temperature is increased towards and above 685C increasing amounts of selenium would be lost from the sample by evaporation. Since the lower growth temperatures for crystallites is already significantly above the boiling point of sulphur it would also be expected that a further increase in temperature would have a relatively small effect on the amounts of sulphur lost. The overall effect of this would be greater quantities of selenium being lost (relative to sulphur) as the growth temperature is increased, resulting in less selenium being incorporated into the crystallites. This is consistent with the experimental observations, however a possibly more important contributing factor is discussed in (iii), below.

(iii) The melting points of CdSe and CdS are 1239C and 1475C, respectively. Thus, as the temperature is increased it would be expected that selenium rich crystallites would become unstable more rapidly than sulphur rich crystallites and have a greater tendency to "redissolve" into the solid solution. This effect would result in samples produced at higher growth temperatures containing crystallites with a higher sulphur content. This is also consistent with the experimental observations.

It has been shown in this section that the stoichiometry of crystallites is not solely determined by the relative concentrations of the dopants initially within the glass but also by the crystallite growth temperature. Thus, whenever it is necessary to study finite size effects by investigating a series of samples containing quantum dots of different sizes but of the same stoichiometry the growth temperature is an inappropriate parameter with which to control the sizes of $CdSe_xS_{1-x}$ crystallites. As can be seen from Table 5.5 a 25C variation in growth temperature results in a stoichiometry variation of $\Delta x = 0.09$. This correspond to a bulk energy gap shift of 62meV (see Equation 2.2 in section 2.1.2) and a shift in the position of the bulk zone centre CdS-like LO phonon of ~3.5cm^{-1} (see Figure 5.2).

Possible solutions to this problem are:-

(i) Use different temperatures to grow crystallites of different sizes and compensate for temperature induced stoichiometric variations by altering the initial sulphur/selenium doping concentration in each sample in order to produce samples containing crystallites of different sizes but of constant stoichiometries. This is would be very difficult to accomplish and, since a much better solution exists, was not seriously considered.

(ii) Control the crystallite sizes by varying the annealing period and not the growth temperature. However, Borrelli et al [5.6] and Potter et al [5.9] have suggested that the stoichiometries of $CdSe_xS_{1-x}$ crystallites vary with time during the growth process, even if the annealing temperature is fixed. This suggestion is based on an observed deviation of the crystallite radius as a function of growth period from the behaviour predicted by Lifshitz and

Slezov (see section 3.1.3). This eliminates using the growth period as a variable with which to produce crystallites of different sizes but a fixed stoichiometry.

(iii) Completely remove the crystallite stoichiometry as a variable parameter by using only CdS or CdSe crystallites. This solution was adopted in order to prepare samples in which to study three dimensional phonon confinement (see section 5.10). The $CdSe_xS_{1-x}$ doped Schott glasses which are commercially available (see section 5.9) do not contain a selenium free glass. However, glasses RG695 and RG715 were found, using Raman scattering, to contain CdSe crystallites, with any sulphur present existing at levels too low to produce an observable CdS-like LO phonon peak (see section 5.5). This will be discussed further in section 5.10.

5.9.2 Dependence of Crystallite Size on Growth Temperature

A series of samples were then prepared from Schott filter glass RG695. As mentioned previously this glass shows only a Raman scattering feature characteristic of CdSe indicating that any sulphur present is only incorporated into the crystallites at a level of a few percent at most. The thermal processing applied to these samples is summarised in Table 5.6, below.

Sample	Starting Glass	"Clearing"		Nucleation and Growth	
		T	t	T	t
T1	Schott RG695	1150C	30 min.	650C	16 hr.
T2	Schott RG695	1150C	30 min.	700C	16 hr.

Table 5.6 Thermal processing conditions for samples T1 and T2. These samples were prepared to study the effects of growth temperature on crystallite size.

Figure 5.19, below, illustrates the photoluminescence spectra of these samples. In this diagram the spectral features corresponding to peak A in Figure 5.3 are indicated by arrows. These features are less prominent than in Figure 5.3 because of the relatively low excitation powers with which these spectra were obtained.

104

ENERGY (eV)

INTENSITY (arbitrary units)

700C

650C

WAVELENGTH (nm)
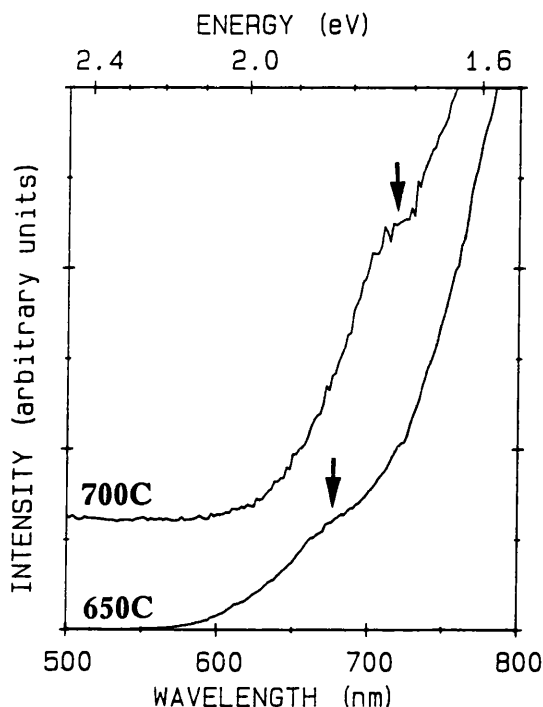
Figure 5.19   Photoluminescence spectra of samples prepared at different growth temperatures.

There is a clear high energy shift in the position of the spectral feature corresponding to peak A in Figure 5.3. This indicates a reduction in crystallite size as the growth temperature is reduced. Varying the crystallite growth temperature while maintaining a constant growth period is a common method by which to prepare crystallites of different sizes and will be adopted in section 5.10.

5.9.3 Dependence of Crystallite Size on Doping Concentrations

The novel effect of doping concentrations on crystallite growth was then investigated by "diluting" commercial Schott glass RG695 with different quantities of a similar borosilicate glass. The sample preparation details are tabulated in Table 5.7, below.

Sample	Starting Glass	Concentration of RG695	"Clearing"		Nucleation and Growth	
			T	t	T	t
D1	Schott RG695	50%	1150C	30 min.	700C	16 hr.
D2	Schott RG695	20%	1150C	30 min.	700C	16hr.
D3	Schott RG695	10%	1150C	30 min.	700C	16hr.

Table 5.7   Thermal preparation conditions of samples D1, D2 and D3. These samples were prepared to study the effect of doping concentration on crystallite size.

105

The photoluminescence spectra of these samples are illustrated in Figure 5.20, below.
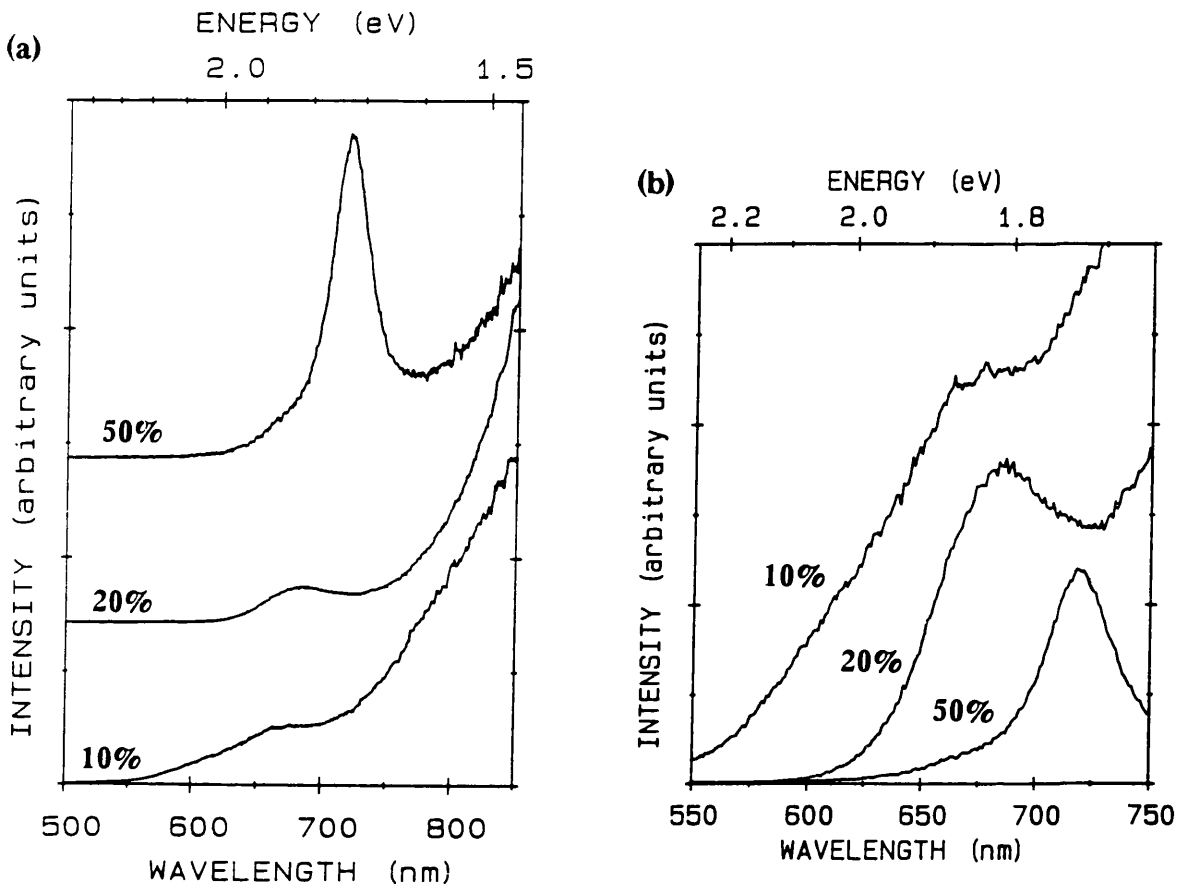
Figure 5.20 (a) Photoluminescence spectra of samples containing
different levels of initial semiconductor dopant.
(b) Spectra have been suitably normalised to illustrate
clearly the shift in the high energy peak.

This figure clearly illustrates a "blue" shift in the emission and, hence, a reduction in crystallite size as the doping concentration of the microcrystallite doped glass is reduced. This size reduction is probably to be expected as the doping concentration is reduced. If the density of crystallites within the glass remains approximately constant a stage will clearly be reached after which a further reduction in doping concentration will inevitably result in crystallites of a reduced size due to the lower quantities of component material available.

5.9.4 Miscellaneous Observations on Crystallite Growth

(a) Samples which were given a heat treatment consistent with the production of very large crystallites became opaque and lost their transparency.

(b) Samples of Schott glass GG495 which were heated at 1150C for 300 hours were found to be impossible to "strike". Even if annealed within the temperature range of crystallite growth

for long periods these samples remained transparent. This is attributed to the loss by evaporation of, in particular, sulphur and selenium from the sample. This effect, although in a less extreme form, was discussed in section 5.9.1.

(c) Samples which were produced at high growth temperatures with long annealing times were found to have emission spectra which differed markedly from those already presented. Figure 5.21, below, illustrates the photoluminescence spectrum of a sample in which the crystallites were grown at 800C for 48 hours.
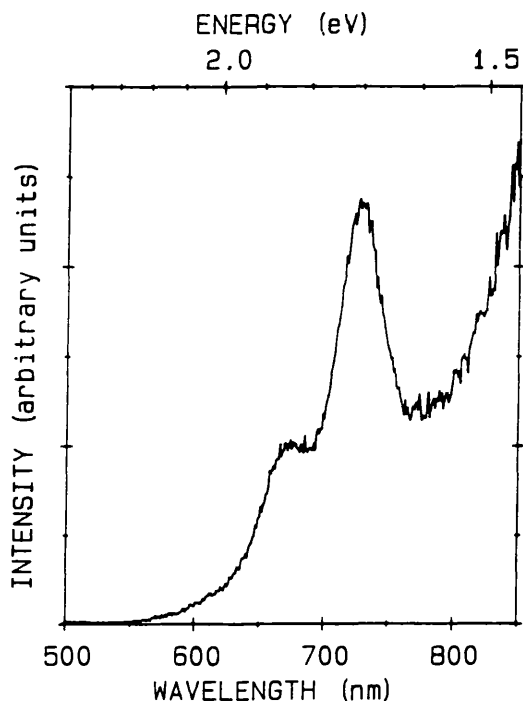
Figure 5.21 Photoluminescence spectrum of a sample illustrating two high energy peaks.

This figure illustrates two peaks which resemble the peak labelled as "A" in Figure 5.3. Warnock et al [5.11,5.12] have observed emission spectra with two sharp peaks in some commercially available Corning filter glasses. They attribute the higher energy peak to emission from small microcrystals, illustrating quantum confinement, and the lower energy peak to emission from larger bulk-like fragments. If this explanation is correct it is not obvious why some growth conditions should produce a crystallite size distribution function with peaks at low and high crystallite radii. A possible explanation is that at high growth temperatures, the critical radius is large (see chapter three) and only a relatively small number of crystallites will spontaneously form with sizes which exceed this radius. These will continue to grow and become the bulk-like crystallites, corresponding to the low energy peak in Figure 5.21. The high temperature and, hence, the high diffusion coefficients of the dopants will result in crystallites of sizes smaller than the critical radius forming spontaneously very rapidly. If the critical radius (and hence the growth temperature) is not too large the "redissolving" of these crystallites might be relatively slow. Hence a large number of these small crystallites will exist

at any given time, although, being unstable, they cannot grow into "bulk-like" crystallites. When the material is cooled (removed from the furnace) these "unstable" crystallites will be "frozen" in the glass resulting in a sample which contains both "bulk-like" crystallites and smaller crystallites illustrating quantum confinement. At higher still temperatures the "unstable" crystallites will redissolve too rapidly for a large number of them to exist at the same time and the critical radius will be too large to allow the formation of a significant number of "stable" growing crystallites. These are the "clearing" temperatures of the glass.

5.10 Three Dimensional Phonon Confinement

In this section the effects of three dimensional phonon confinement in semiconductor doped glasses will be considered. Sample choice and preparation will be discussed followed by the experimental Raman spectra and a comparison between the experimental results and the theory described in section 2.4.

5.10.1 Sample Choice and Preparation

For this experiment it was considered important to produce samples with crystallites of differing sizes but of stoichiometries as constant as possible. As discussed in section 5.9.1, the independent control of these two variables is difficult for $CdSe_xS_{1-x}$ ($x \neq 0, 1$) microcrystallites. The preferred material for this series of experiments was therefore CdS or CdSe doped glasses. By considering the phonon dispersion relations for these two semiconductors (CdS and CdSe) the material can be chosen in which phonon confinement will be more readily observed. Figure 5.22, below, schematically illustrates the dispersion characteristics of a longitudinal optical phonon in these materials.
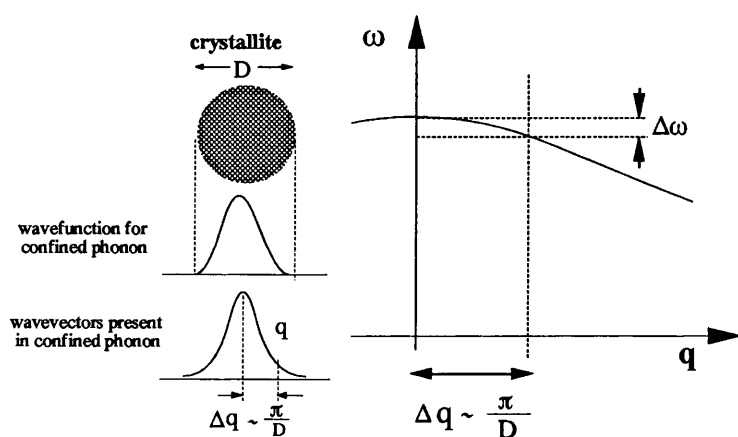
Shift in the phonon energy due to phonon confinement ~ $\Delta\omega/2$

Figure 5.22   Schematic diagram illustrating the relaxation of the q≈0 selection rule in small crystallites.

As can be seen from the above diagram the expected low energy "red" shift in the "q≈0" phonon will be of the order of $\Delta\omega/2$. For a completely flat dispersion curve $\Delta\omega$ will be zero, with $\Delta\omega$ increasing with the "steepness" of the dispersion curve around q=0. CdSe has a flatter dispersion curve than CdS and so, for a given crystallite size, CdS would be expected to produce a greater "red shift" in the "q≈0" phonon energy. Unfortunately, no commercially available Schott filter glass was found to contain crystallites of CdS. The nearest to this stoichiometry is glass GG495 which contains crystallites of $CdSe_{0.3}S_{0.7}$ (see section 5.5). Rather than tolerate significant stoichiometry variations it was decided to perform the experiments on CdSe doped glasses. As was discussed in section 5.5, Schott glass RG695 was found to contain crystallites of CdSe with any sulphur present existing at levels of a few percent. Even if this glass contains small levels of sulphur, or another "impurity" that is incorporated into the crystallites, the low levels of this third material will assist in minimising stoichiometry fluctuations between the samples. This glass was used as a starting material from which crystallites of different sizes were prepared by the method discussed previously (see chapter three). The preparation conditions for the samples discussed are tabulated in Table 5.8, below.

Sample	Starting Glass	"Clearing"		Nucleation and Growth	
		T	t	T	t
P1	Schott RG695	1150C	30 min.	625	24hr.
P2	Schott RG695	1150C	30 min.	629	24hr.
P3	Schott RG695	1150C	30 min.	633	24hr.
P4	Schott RG695	1150C	30 min.	637	24hr.
P5	Schott RG695	1150C	30 min.	646	24hr.
P6	Schott RG695	1150C	30 min.	650	24hr.
P7	Schott RG695	Unprocessed Schott Glass			
P8	Schott RG695	1150C	30 min.	675	24hr.

Table 5.8   Thermal preparation conditions for samples P1 to P8. These samples were prepared to study the effects of phonon confinement.

In Table 5.8 the samples (from P1 to P8) are arranged in order of expected increasing crystallite size.

5.10.2 Experimental Raman Spectra

Figure 5.23, below, illustrates the Raman spectra for three of the samples discussed in section 5.10.1.
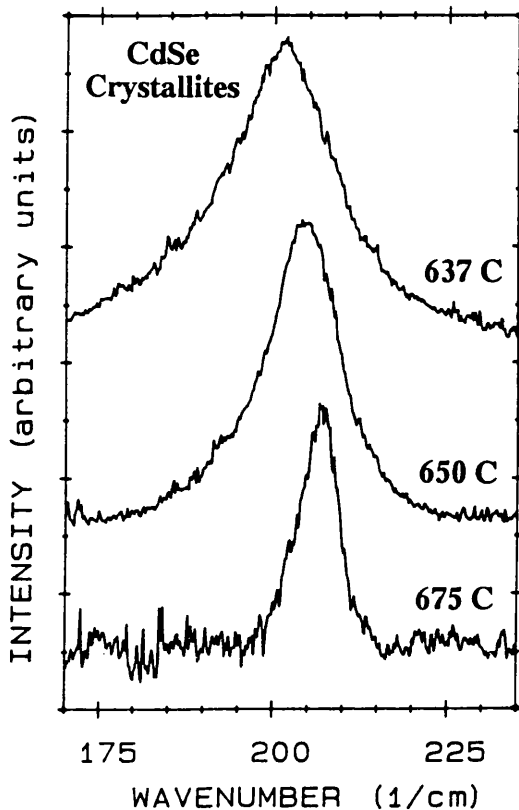
Figure 5.23 Raman spectra of samples prepared at different growth temperatures. From bottom to top the samples contain crystallites of decreasing size.

The lower the growth temperature the smaller the expected size of the crystallites, thus the spectra in Figure 5.23 represent, from bottom to top, Raman scattering from crystallites of decreasing size. A clear "red shift" and broadening with decreasing crystallite size are evident and are certainly qualitatively consistent with the relaxation of the $q \approx 0$ selection rule that is to be expected for small crystallites.

5.10.3 Comparison of Theory and Experiment

In Figure 5.24, below, the low energy shift in the position of the LO phonon is shown as a function of the width of the LO phonon peak (full width at half maximum) for the samples P1 to P8. The solid line is the theoretically predicted result based on the model of section 2.4.

110
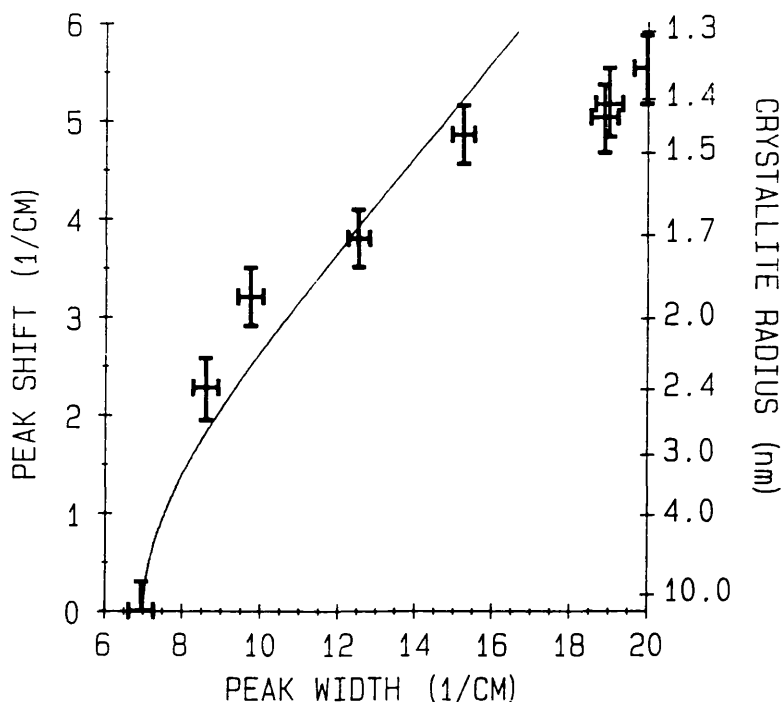
Figure 5.24 A graph of phonon shift as a function of peak width. The solid curve is the theoretical prediction and the points are from samples P1 to P8.

The shift illustrated in this figure has been measured relative to the position of the LO phonon peak in samples which received heat treatments which would be expected to produce crystallites with a very large size. Further annealing of these samples (containing large crystallites) produced no significant addition shift in the phonon position and its was therefore assumed that they represented the scattering of light by essentially bulk material. These samples had a peak at $208cm^{-1}$ which compares with a reported peak position of $210cm^{-1}$ for bulk CdSe. If this discrepancy is attributed to the presence of sulphur in Schott glass RG695 then the crystallites in these samples would have a sulphur content of <5%. A small, even if non-zero, sulphur content is, of course, advantageous in minimising phonon shifts associated with stoichiometry variations. The samples given these heat treatments also displayed a phonon width which compared closely with that reported from bulk material, further justifying the assumption that they represent crystallites with essentially bulk phonon characteristics.

The experimental and theoretical results are in good quantitative agreement, however, other factors which can influence the position of the LO phonon position should also be considered.

(i) S/Se Ratio Variation

As shown in Figure 5.18 decreasing the crystallite growth temperature results in relatively lower quantities of sulphur being incorporated into the crystallites. This produces a high energy shift in the position of the CdSe-like LO phonon (see Figure 5.2). This is the opposite of what is observed experimentally and must be discarded as an explanation.

(ii) Hydrostatic Pressure from the Glass Matrix

This effect results from the different thermal expansion properties of the semiconductor microcrystals and the glass host, and as reported by Zhou et al [5.26] produces a high energy shift in the position of the LO phonon. Hence this must also be rejected as an explanation of the experimental results.

In view of the above discussion and the favourable comparison with theory it would seem likely that the experimentally observed effect is indeed the result of three dimensional phonon confinement. It should be emphasised that the theoretical graph of peak position versus peak width (Figure 5.24 with the exception of the right vertical axis) is entirely independent of the "adjusted parameter", α, (see section 2.4) and is therefore an extremely good test of the model's validity. The sizes indicated on the right vertical axis in Figure 5.24 are, of course, dependent upon the choice of α. If the observed shifts and broadening are interpreted in terms of phonon confinement there is a clear discrepancy between the theoretical result and the experimental observations for the smaller crystallites. Since the LO phonon dispersion curve is of finite width (in energy) the phonon cannot be "red shifted" indefinitely and it would be expected that a maximum shift would eventually be reached even though the peak width may still be increasing (although obviously this would also reach a maximum limit within the model presented here). The model does produce this effect but the limiting value of phonon shift predicted is ~6cm^{-1} whereas the experimental points would indicate a value of ~5.5cm^{-1}. Possible reasons for this discrepancy and other limitations of the model are discussed below (see also section 2.4.4).

(i) As shown by the theoretical study of the effect of crystallite size distribution on phonon confinement, a nonuniform size distribution could partly account for the discrepancy (see section 2.4, Figure 2.29).

(ii) The form of the confinement function does affect the confinement energies and the fit between the experimental points and the theory could possibly be improved by choosing an alternative form for this function (see section 2.4).

(iii) Hydrsostatic pressure from the glass host can produce a "blue shift" in the phonon energy which, for smaller crystallites, might partially counteract the "red shift" due to phonon confinement.

(iv) The presence of an amorphous component within the crystallites would widen the phonon peak to an extent greater than that indicated by the theoretical curve shown in Figure 5.24 [5.27].

(v) Surface phonon features have been observed on the low energy side of the CdS-like LO phonon in sulphur rich microcrystallites investigated by Zhou et al [5.26]. No such features were observed in any of the samples prepared in this project. It is difficult to explain the appearance of surface phonon features in the samples of Zhou et al and their absence in samples P1 to P8. Even sulphur rich crystallites investigated in this project showed no features resembling those of Zhou et al and their absence must presumably be attributed to the nature of

the glass/semiconductor interface and the chemical, and thermal, properties of the host glass. If, however, due to broadening, there existed an unresolved surface phonon peak in the spectra of samples P1 to P8 this would have a broadening effect on the Raman peak that the model presented here does not describe.

(vi) The model assumes the crystallites to be spherical. If the crystallites are hexagonal columns the phonon confinement energies will be altered.

(vii) The model inherently becomes increasingly inaccurate as the crystallite sizes are reduced and a discrepancy for the smaller crystallites might be expected. For very small crystallites contributions to the scattering will occur from phonons with wavevectors further from the zone centre, where the simplified model of the phonon dispersion will be less accurate (again, see section 2.4, in particular Equation 2.28).

5.10.4 Conclusions

The observed phonon shifts and broadening have been found to be in reasonably good quantitative agreement with a simple model based upon a relaxation of the "q≈0" selection rule in small crystallites. Although the contribution of other factors to the position of the LO phonon cannot be discounted its seems probable, given the agreement between experiment and theory, that the model used does describe the dominant physical effect occurring in this system of microcrystals. Other workers, however, have not found this to be the case. Scamarcio et al [5.28] predict via a theoretical model that the stress induced "blue shift" from the host glass will always dominate the finite size induced "red shift". They also present results from three samples of $CdSe_xS_{1-x}$ which show a phonon "blue shift" with decreasing size. They estimated the S/Se ratio from the relative intensities of the CdS-like and CdSe-like LO phonon peaks in order to correct for stoichiometry variations between the samples. It is difficult to reconcile the results presented here with those of Scamarcio et al without detailed information about the samples involved. If the samples were prepared at different temperatures (to produce the different sizes of crystallites), then the expected S/Se ratio variations between them would be such as to produce a stoichiometric "blue shift" in the phonon energy as the crystallite sizes are reduced. Scamarcio, however, observed "blue shifts" in the CdS-like and CdSe-like LO phonons relative to the LO phonons in CdS and CdSe respectively. This cannot be explained in terms of a stoichiometry variation. A stoichiometry variation would never cause the CdS-like LO phonon or CdSe-like LO phonons to be shifted to energies higher than the LO phonons in CdS and CdSe, respectively (see Figure 5.2). The qualitative discrepancy between the results presented here and those of Scamarcio et al could conceivably result from differing thermal properties the host glasses.

5.11 Other Systems of Microcrystallites

In this section preliminary results will be presented of measurements made on crystallites of InAs prepared in an aqueous solution and coloured glasses which were prepared in an attempt to produce silicon crystallites within a glass matrix.

5.11.1 Indium Arsenide Crystallites in Aqueous Solution

The sample investigated was prepared by T.J. Cumberbatch and A. Putnis, of the University of Cambridge, by passing arsine through an aqueous solution of indium nitrate [5.29]. A sample of indium arsenide microcrystallites in solution prepared by this method was investigated using Raman spectroscopy. Figure 5.25, below, illustrates the Raman spectrum from this sample.
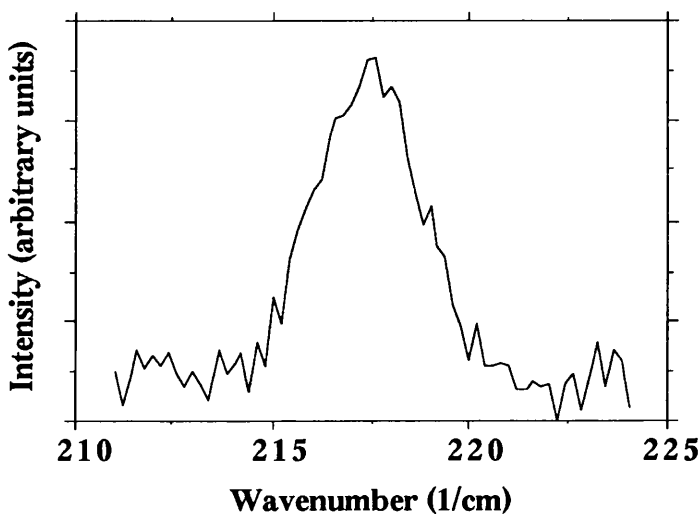
Figure 5.25   Raman spectrum of InAs crystallites illustrating a bulk-like TO phonon.

This spectrum was obtained from a quantity of the solution (containing crystallites) that was allowed to dry on a clean metal plate leaving a dark deposite of powder. The Raman scattering signal from this material, when excited at 488nm, was found to be extremely weak, however, Figure 5.25 does illustrate a sharp peak at $217.5cm^{-1}\pm0.3cm^{-1}$ with a full width at half maximum of $\sim3cm^{-1}$. This compares with the reported bulk InAs TO phonon position of $217.3cm^{-1}$ [5.30,5.31]. The bulk-like Raman scattering properties of these crystallites are as would be expected considering their relatively large sizes, $\sim100nm$. Using the simple argument illustrated in Figure 5.22 it would be expected that in order to observe a shift in the Raman scattering peak of $\sim1cm^{-1}$ the crystallite sizes would have to be of the order of a few nanometres (the phonon dispersion curve for TO phonons in InAs is relatively flat) [5.29,5.30].

The spectrum illustrated above was obtained using the photomultiplier tube detection system. For such a weak signal it would have been advantageous to use the "multichannel" CCD detection system (see chapter four). This was, however, not found to be practical. The use of a

"multichannel" detection system requires spectrometer slits F_2 and F_3 to be opened very wide (see section 4.3.1) which reduces the stray light rejection capability of the instrument. With a reduced stray light rejection, stray laser light can reach the detector and forms a background to the signal being measured. In the case of this sample this background completely masked the weak Raman signal and, for longer integration times, saturated the CCD detecting elements. A possible solution to this problem would be to use a suitably chosen bandpass interference filter. Alternatively, an iodine gas cell could be placed before the entrance slit of the spectrometer. Iodine has an atomic absorption line which coincides closely with the 514nm laser emission of an argon ion laser and will absorb this line very strongly, preventing stray laser light entering the spectrometer. This atomic absorption line is extremely sharp so will only absorb a small range of wavelengths around the laser emission wavelength allowing light to be observed which is only shifted slightly from the laser line (in this respect an iodine gas cell is preferable to an interference filter). Although iodine has many other absorption lines in the spectral region that a typical Raman spectrum will cover, these line are extremely sharp (Doppler broadened to 500MHz) and would not be resolved by the U1000 spectrometer, allowing the excitation light (514nm) to be removed without noticeably altering the measured Raman spectrum [5.32].

5.11.2 Coloured Glass Produced by the Addition of a Silicon Dopant

This section will describe the preparation and characterisation of coloured glasses produced by the addition of a silicon dopant to an otherwise transparent silica glass melt. Preliminary results of absorption, photoluminescence and Raman scattering measurements will be presented and discussed in relation to the work of other researchers who have produced silicon crystallites by sputtering and evaporation techniques.

5.11.2.1 Sample Preparation and Characterisation

These samples of coloured glass were prepared by adding finely powdered silicon (~40μm particles) to either a standard soda-lime or borosilicate glass, which was also finely powdered. Depending upon the quantity of silicon added, the resultant glass varied in colour from yellow to yellow/brown to black. The preparation conditions for two samples, SI1 (black in colour) and SI2 (yellow in colour), are given in Table 5.9, below.

Sample	Starting Glass	Concentration of Silicon	Thermal Processing		
			T	t	
SI1	soda-lime	1.0%	1150C	25 hr.	The samples were then allowed to cool slowly in the furnace from 1150C to 600C over typically 5 hours
SI2	soda-lime	0.1%	1150C	24 hr.	

Table 5.9   Preparation details for samples SI1 and SI2.

Figure 5.26 below, illustrates absorption spectra for samples SI1 and SI2.

Figure 5.26
Absorption spectra of "silicon doped glasses" prepared with different doping concentrations.
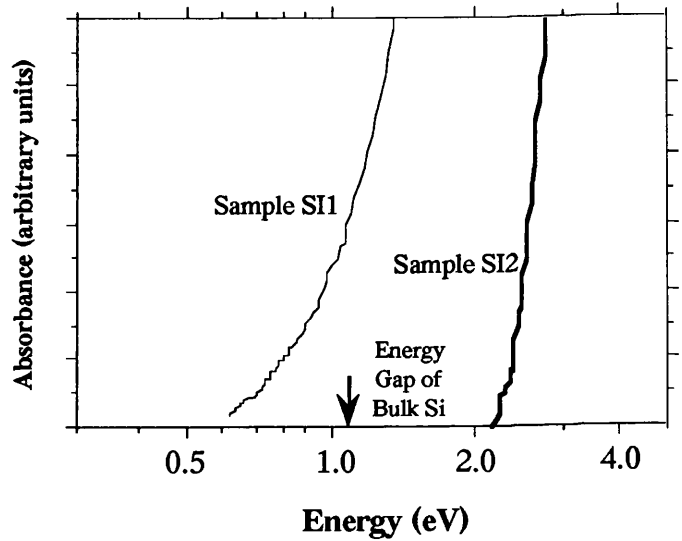
The absorption of sample SI1 starts to rise sharply ~1eV with a long tail extending to lower energies, while the absorption edge of sample SI2 is ~2.2eV. If the observed absorption characteristics are attributed to the presence of silicon crystallites within the glass the observed energy gaps are qualitatively consistent with those expected from the preparation conditions for the two samples. Sample SI2 was prepared with a much lower doping concentration than sample SI1 and, as discussed in section 5.9.3, it would therefore be expected that sample SI2 would contain crystallites of a considerably smaller size than those within sample SI1. Under such circumstances the observed energy gap shift would be consistent with the effects of carrier confinement within the crystallites (other possibilities will be considered later).

Figure 5.27, below, illustrates the absorption and emission spectra for one of these samples (sample SI2).
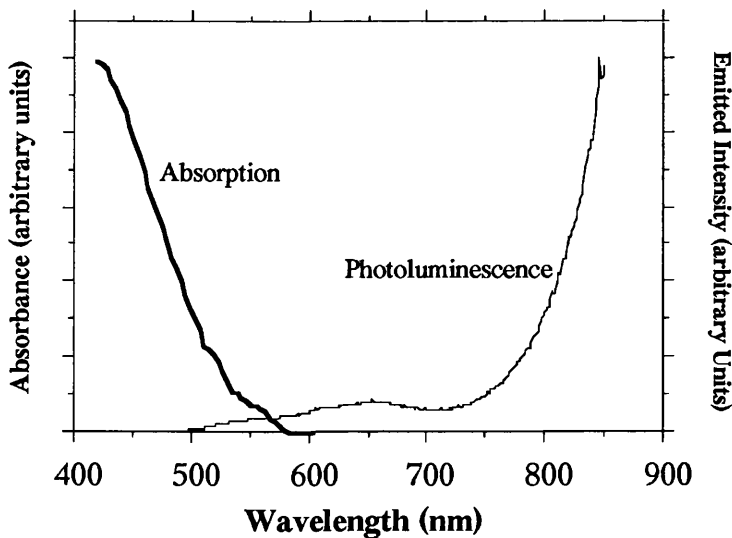
Figure 5.27   Absorption and photoluminescence spectra of "silicon doped glass" prepared with the lower doping concentration (ie sample SI2).

The features present in the emission spectrum of Figure 5.27 have not been identified,

however, a resemblance to the emission spectra of $CdSe_xS_{1-x}$ doped glasses is evident (the spectrum of Figure 5.27 has been normalised with respect to the spectral response of the U1000 spectrometer system).

In order to try to identify the source of the absorption and photoluminescence induced by the added silicon (ie, to determine if they result from the presence of silicon microcrystallites within the glass) a Raman scattering experiment was performed. The Raman spectrum of sample SI2 is illustrated in Figure 5.28, below.
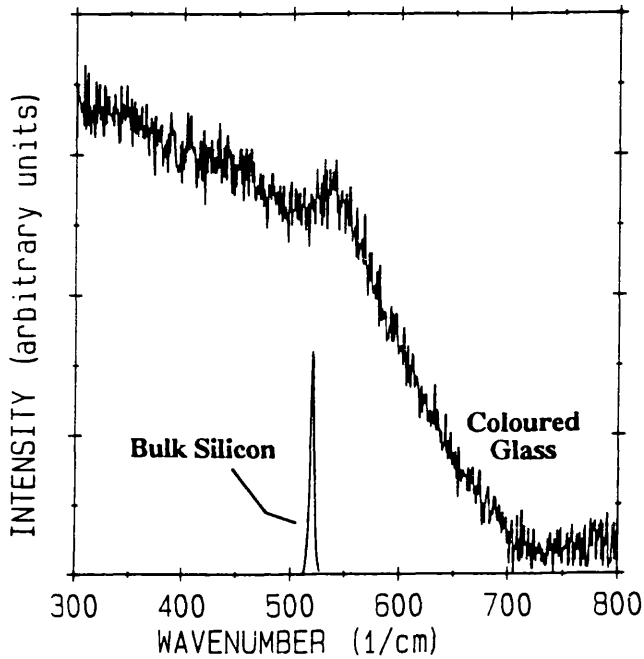
Figure 5.28   Raman spectrum of sample SI2. Also shown, for comparison, is a spectrum of bulk silicon.

The spectrum illustrated above has had the emission of the "undoped" glass numerically subtracted from it. This was done by taking a "reference" spectrum from an "undoped" glass sample, identifying the spectral region where the "reference" spectrum matched that of the sample, normalising both spectra to be of equal intensities in this region and then subtracting the "reference" spectrum from that of the sample. This manipulation does not greatly affect the shape of the final spectrum, with the "uncorrected" spectrum qualitatively resembling the "corrected" spectrum. For comparison Figure 5.28 also illustrates the LO phonon peak for bulk silicon.

5.11.2.2 Discussion

The broad Raman spectrum of Figure 5.28 is very different from that of the powdered silicon added initially to the glass, which matched that of the bulk material. These coloured glass samples are therefore not a simple suspension of the initial silicon powder within the glass. The Raman spectra of these samples are similar to that of amorphous silicon possibly suggesting

117

that the glass contains particles of amorphous silicon. However, it has been observed by some researchers that the spectra of small crystalline particles can produce broad amorphous-like Raman spectra. Figure 5.29, below, illustrates Raman spectra of silicon crystallites obtained by Tonouchi et al [5.33]. Tonouchi et al prepared their samples by sputtering silicon onto silicon or fused quartz substrates.
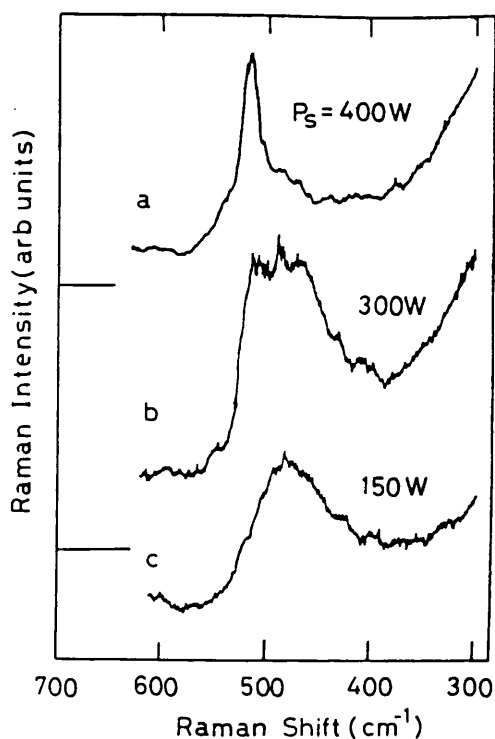
Figure 5.29   Raman spectra of silicon crystallites prepared using a sputtering technique by Tonouchi et al [5.33]. P_s is the sputtering power which is used to control the crystallite sizes, with a reduced sputtering power resulting in smaller crystallitres.

Tonouchi et al used x-ray diffraction techniques to determine the crystalline volume fraction of the crystallites and found it to remain approximately constant as the crystallite size is reduced. Figure 5.30, below, illustrates Raman spectra from Ge microcrystals embedded within a GeO_2 matrix reported by Ovsyuk et al [5.34], who suggest that the broad Raman spectra may result from scattering from an amorphous component of the crystallites or from their surfaces.

Figure 5.30
Raman spectra of germanium microcrystals within a GeO_2 matrix, as measured by Ovsyuk et al [5.34].

a-Ge amorphous germanium
c-Ge crystalline germanium

a to e are the spectra of crystallites of increasing size
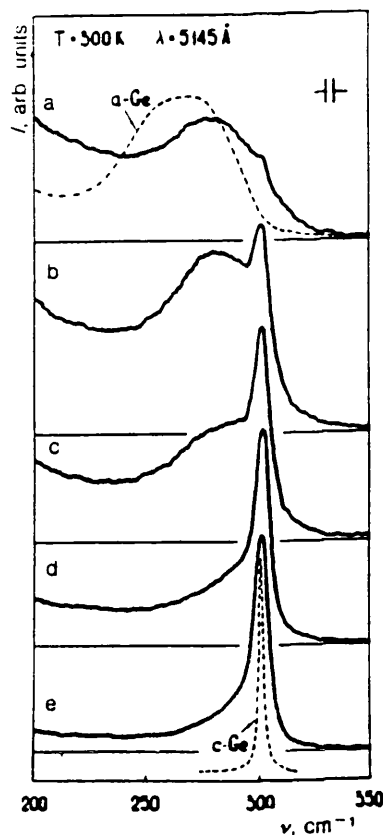
Hayashi et al report amorphous-like Raman spectra from Si, Ge and GaP microcrystals even though they have performed electron diffraction experiments which show the crystallites to be crystalline [5.35-5.38]. Fujii et al [5.39] report a sharp Raman peak from Ge crystallites embedded in a thin film of SiO_2, even though their crystallites were of comparable sizes (6nm-15nm) to those of Hayashi et al [5.35-5.38]. They attribute the broad Raman spectra of Hayashi et al to enhanced scattering from the crystallite surfaces, where the atoms are, to a large extent, disordered. They explain their sharp Raman features by assuming that, for their crystallites, the boundary conditions applying to the crystallites prevent vibrations in the disordered surface layer (see also [5.40-5.42]).

Silicon crystallites prepared by sputtering techniques have also been found to possess energy gaps greatly "blue-shifted" from that of bulk silicon. Furakawa et al [5.41-5.43] prepared silicon microcrystals of sizes 2nm-3nm by sputtering silicon onto substrates cooled to ~100K and report optical energy gaps shifted to energies as high as 2.4eV. They attribute the energy gap shift to three dimensional quantum confinement. Figure 5.31, below, illustrates an absorption spectrum of such crystallites [5.41].
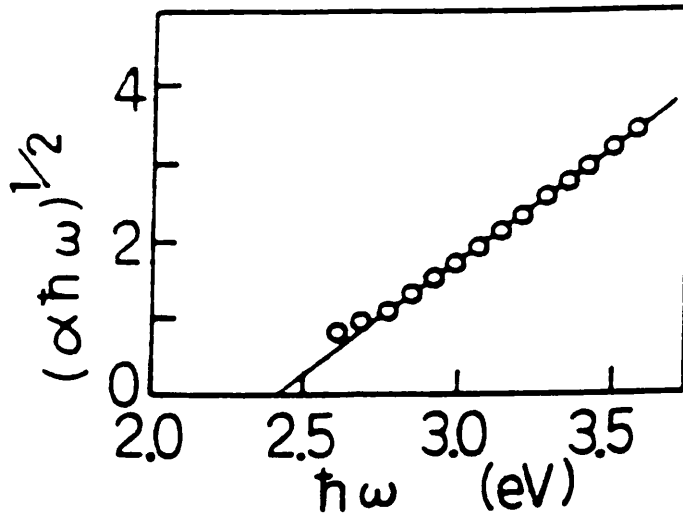
Figure 5.31 Optical band gap of silicon microcrystals prepared by a sputtering technique, as reported by Furakawa et al [5.41].

Figure 5.32, below, illustrates a comparison between optical energy gaps observed by Furakawa et al [5.41] for crystallites and the predictions of their carrier confinement model.
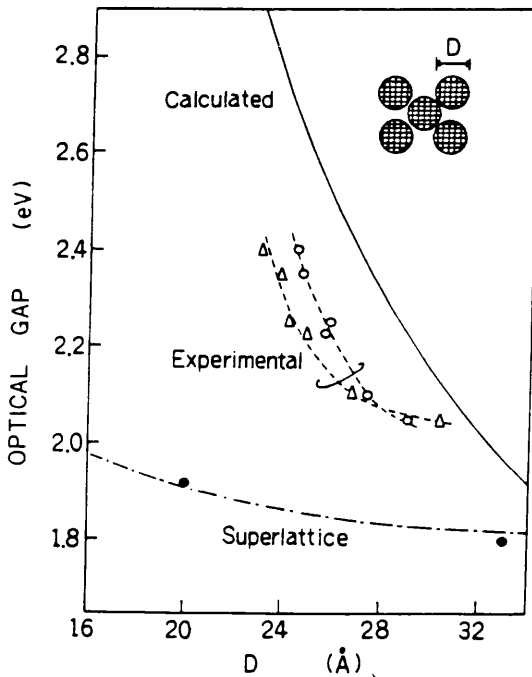
Figure 5.32 Theoretical effective energy gap of silicon microcrystals (solid curve) and experimentally measured optical band gaps ($\triangle$,o). The broken curve is the calculated effective energy gap for a a-Si:H/a-SiN$_x$:H superlattice. As reported by Furakawa et al [5.41].

Yamamoto et al [5.44] also observed high energy shifts in the absorption edge of silicon microcrystals, prepared by a sputtering technique, which they attribute to quantum confinement. They also present a theoretical model to describe their observations. High energy

shifts in the emission spectra of silicon "wires" prepared by an electro-chemical etching technique have also been reported [5.45-5.47]. However, it has been suggested that the visible light emitted by this material, known as "porous silicon" because of its sponge-like appearance after the etching process, originates from siloxene ($Si_6O_3H_6$), which is produced during the etching, and not from carrier confinement within the etched "wires" [5.47].

The properties of the coloured glasses described earlier possess similarities with the properties of the Si crystallites prepared by other researchers. It might therefore be tentatively suggested that these samples contain silicon crystallites and that the observed colour variation results from three dimensional quantum confinement.

Since the starting undoped glass was not prepared from its initial oxides it is difficult to exclude the possibility of other chemical factors being responsible for the glasses becoming coloured when doped with silicon. One such alternative explanation would involve the added silicon acting as a reducing agent causing a colourless atom within the glass matrix to become a coloured ion. It is, however, difficult to explain why, if this alternative explanation is correct, adding a lower quantity of silicon would result in a shift in the absorption edge rather than just increasing the magnitude of the absorption and deepening the colour of the glass. Obviously, considerably more work would be required in order to reach any firm conclusions on this topic. The limitations of the results presented here and suggested further research which might allow the verification or contradiction of the above suggestions will be discussed in chapter six.

5.12 Summary

In this chapter results of an optical investigation into the properties of semiconductor crystallites have been presented and some explanations of the experimental observations have been offered. The techniques of absorption, photoluminescence and Raman spectroscopies, together with a time resolved pump probe experiment, have been utilised to investigate the effects of crystallite size and stoichiometry variations. A study of the variables involved in the preparation of microcrystallite doped glasses has been presented which, it is hoped, would be of use to those wishing to investigate further the properties of this very interesting class of materials. Of the more firm conclusions arrived at in this work, the study of the effects of crystallite size on the Raman scattering properties of microcrystallites has produced good evidence for three dimensional phonon confinement within CdSe crystallites. The results of preliminary work on samples produced by the addition of crystalline silicon to silicate glass melts have also been presented. This area in itself would offer ample scope to continue the work of this experimental investigation. Such further work, together with a overall review of the achievements and limitations of this project, is the topic of the next, and final, chapter of this thesis.

Chapter 6 - Overall Conclusion and Suggested Future Work

In this chapter the work presented in this thesis will be briefly summarised together with possible ways in which the work might be extended in order to verify or refute the explanations suggested in the previous chapters.

6.1 Summary of Work Presented in the Thesis

The energy states within $CdSe_xS_{1-x}$ crystallites embedded within a glass matrix were probed by means of absorption and photoluminescence spectroscopies. The absorption edge structure associated with the discrete energy states of the confined electrons and holes within the crystallites was found to increase and become more prominent as the crystallite sizes were reduced, in agreement with the work of many other researchers. The photoluminescence spectra of the crystallites were found to display two or three quite distinct features. The observed high energy peak, it was suggested, results from either direct, band to band recombination or recombination via states lying close to the conduction or valence band. The Stokes shifts observed between these high energy peaks (assuming them to represent band to band recombination) and the corresponding absorption edge features are large compared with the energies of optical phonons and increase as the crystallite sizes are reduced, suggesting an enhanced coupling between the electronic and vibrational states for small crystallites. If these high energy peaks represent recombination via impurity or defect states the shift between them and the absorption edge features, corresponding to the lowest energy bound states of the electrons and holes, would be expected to increase as the crystallite sizes are reduced due to a "confinement" effect on the impurity or defect. The photoluminescence spectra also displayed an intensity dependence, with the high energy peak discussed above becoming more prominent as the excitation intensity is increased. An explanation for this observation was offered in terms of the saturation of the deep lying states responsible for the very broad low energy luminescence of these crystallites. The difficulty in saturating these energy gap states was found to increase as the crystallites become smaller, which is consistent with the interpretation of these states as being associated with the surfaces of the crystallites.

The relaxation of excited carriers within the crystallites was investigated using a pump probe experiment in which an intense pump pulse partially saturated the absorption of the material via a state filling effect. The relaxation of the material's nonlinear absorption was then measured some variable time later by a much less intense probe pulse. The relaxation of the carriers was

found to possess rapid and slow components. The relative importance of these components was found to depend upon the intensity and wavelength of the excitation pulses. Under low intensity excitation the slow relaxation component was dominant with the fast component increasing in importance as the excitation pulses became more intense. The slow component of the relaxation is also dominant at long pump/probe wavelengths with the fast component becoming increasingly prominent as the pump/probe wavelength is reduced. The wavelength dependence is attributed to the same physical effect as the intensity dependence, namely, the saturation of states within the energy gaps of the crystallites. At long pump/probe wavelengths the low absorption of the crystallites produces a condition analogous to a low intensity pump excitation. At shorter wavelengths the higher absorption of the material results in a greater amount of light being absorbed and is analogous to exciting the material with a high intensity pump pulse. Two suggestions were offered to explain the two component relaxation of the material:-

(i) The rapid component results from direct, band to band, recombination and the slow component from recombination via the energy gap states. It has been suggested (see chapter five) that direct electron hole recombination in microcrystallites can be faster than in the corresponding bulk material due to the greater overlap of the wavefunctions for the electrons and holes. The intensity dependence would then result from a saturation of the states within the energy gap as the intensity of the pump pulse is increased.

(ii) The rapid component results from nonradiative Auger recombination and the slow component from radiative recombination processes. This Auger recombination would become of increasing importance as the number of excited carriers is increased by, for example, exciting the material with a higher intensity pump pulse.

The phenomenon of photodarkening was then investigated by photoluminescence spectroscopy and the pump probe experiment. Photodarkening was found to reduce the light emission from the energy gap states while leaving the high energy emission peak relatively unaffected and to reduce the importance of the slow component of the nonlinear absorption relaxation. This might possibly suggest that the slow relaxation component is associated with the deep lying energy gap states (see (i), above).

The possibility of using the technique of photoluminescence excitation spectroscopy was then discussed and results were presented of measurements on crystallites using a tunable excitation source consisting of a white tungsten halogen lamp and a small grating spectrometer. This technique was found to be practical and could be useful in situations where transmission measurements are not possible.

The results of a study of sample preparation were then presented. The stoichiometries of samples of $CdSe_xS_{1-x}$ doped glasses were found to be dependent upon the crystallite growth temperature as well as the doping level of the initial glass. It was found that increasing the

growth temperatures (in the 650C to 700C range) resulted in crystallites with a higher sulphur content. The effect of doping concentrations on CdSe doped glasses was then investigated. It was found that reducing the doping concentration resulted in the growth of smaller crystallites as does a reduced growth temperature. The results of this study proved useful in the interpretation of the results of later measurements.

A range of samples containing CdSe crystallites were then described together with the results of Raman scattering measurements performed on them. The samples were prepared at different temperatures and consequently contained crystallites of different sizes. The Raman spectra of these samples illustrate a clear low energy shift in the position of the LO phonon peak and a broadening of this peak with decreasing crystallite size, both of which are qualitatively consistent with a relaxation of the q≈0 selection rule due to the finite extent of the phonon in space causing the nominally q=0 phonon to possess a range of wavevectors around q=0. The experimental results were then compared with the predictions of a simple model of phonon confinement and good quantitative agreement was found. No surface phonon features were observed and the effect of pressure from the glass host material was not found to be of primary importance in determining the LO phonon energy.

Finally, some preliminary work on other systems of microcrystallites was briefly described. InAs crystallites in aqueous solution were studied using Raman scattering and found to possess bulk-like properties consistent with their relatively large sizes. Absorption, photoluminescence and Raman spectra were then presented from measurements performed on coloured glasses prepared by adding crystalline silicon to an initially transparent silica glass melt. By analogy with the published work of other researchers concerning the properties of silicon crystallites prepared by sputtering techniques, it could be tentatively suggested that the colour in these glasses results from the presence of silicon crystallites, with optical energy gaps as large as 2eV resulting from the quantum confinement of carriers within the silicon crystallites. This suggestion is, however, speculative and demands a thorough and systematic investigation (see section 6.2, below).

6.2 Suggested Further Work

This section will discuss some ways in which the work presented here could be extended and the properties of the materials discussed clarified. The following suggestions are not exhaustive in extent but merely indicate experiments which might produce information of particular relevance to the results presented in this thesis.

(i) The photoluminescence spectra presented in this thesis could be complemented by time resolved measurements in which the recombination times associated with the spectral features

discussed in chapter five would be determined. This would also complement the pump probe measurements in which the overall recombination dynamics, by both radiative and nonradiative routes, were probed. A study of the radiative recombination time associated with the high energy peak observed in the photoluminescence spectra of these samples as a function of crystallite size would be an interesting investigation.

(ii) A continued study of the crystallite growth process would also be informative. The properties of $CdSe_xS_{1-x}$ microcrystallite doped glasses prepared by different research groups often vary to a disconcertingly large extent. Since the semiconductor crystallites are nominally the same it is likely that these property variations result largely from the chemical and thermal properties of the glass host. The chemical composition and structure of the glass matrix determine not only the impurities which can be incorporated into the semiconductor crystallites during their growth but also the properties of the glass/semiconductor interface and, hence, the carrier trapping and recombination processes which can occur at these surfaces. The thermal properties of the glass determine the stress applied by it to the crystallites when the material is cooled from the crystallite growth temperature. Such applied stress influences the energy gap of the crystallites and the energy of phonons within them. An investigation of these properties could take the form of preparing different glass melts from the initial oxides and studying the effects of glass composition on the crystallite nucleation and growth rates, the photoluminescence and Raman scattering properties of the samples. This would possibly explain the diverse properties observed by different research groups and explain several observations discussed in chapter five, such as the very different nucleation and growth periods required for Schott and Hoya glasses and the relative importance of the competing effects of stress and confinement in determining the energies of zone centre optical phonons. To prepare such silica glasses from the initial oxides would require a furnace and associated equipment capable of heating the melt to 1450C rather than the 1150C which was used in this project to clear Schott glasses of crystallites.

(iii) The preliminary work on coloured glasses prepared by the addition of crystalline silicon to silica glass melts presented in section 5.11.2 is clearly an area where further, detailed investigations are necessary. In any further study it would be advisable to prepare the glasses from initial oxides in order that the possibility of the glass colour resulting from a chemical effect, such as the reduction of a coloured atom into a coloured ion, might be fully investigated. The chosen glass composition would have to be considered remembering this possibility. Additional techniques which might be employed to study any coloured samples produced could include transmission electron microscopy, Bragg diffraction and small angle x-ray scattering. These techniques might provide more direct evidence than that presented here for the existence of crystallites within these glasses.

Although numerous other studies could be suggested, the few mentioned above, and the

additional work which might follow naturally from them, are probably, in themselves, sufficient to form a project similar to the one discussed in this thesis.

6.3 *Final Remarks*

In this chapter the results of a study of the optical properties of semiconductor crystallites have been summarised. This chapter and the preceeding one, it is hoped, will illustrate some of the scientifically interesting, and possibly technologically important, properties which structures of this type possess. The greater part of this thesis concerned the properties of cadmium selenium sulphide doped glasses which although first produced a century ago still attract attention from researchers on an international scale. In recent years researchers have shown less of an interest in applying the material to the production of ornamental glassware and more of an interest in its nonlinear optical and electronic properties. In this respect and for those wishing to study three dimensional quantum confinement of electrons, holes and phonons it is, and for some time will certainly remain, an "excellent red glass".[†]

[†] Johann Kunckel, glassmaker, chemist, apothecary and alchemist (see chapter one).

References

References for Chapter One

[1.1]   Yanagawa, T., Sasaki, Y. and Nakano, H.
         "Quantum Size Effects and Observation of Microcrystallites in Colored Filter Glasses"
         Appl. Phys. Lett. 54(16) 1495 (1989).

[1.2]   Shinojima, H., Yumoto, J., Uesugi, N., Omi, S. and Asahara, Y.
         "Microcrystallite Size Dependence of Absorption and Photoluminescence Spectra of
         CdS_xSe_{1-x} - Doped Glass"
         Appl. Phys. Lett. 55(15) 1519 (1989).

[1.3]   "Encyclopaedia of Physical Science and Technology" vol. 6 pp. 262-293
         Meyers, R.A. (editor)
         Academic Press Inc (London) 1987.

[1.4]   Borrelli, N.F., Hall, D.W., Holland, H.J. and Smith, D.W.
         "Quantum Confinement Effects of Semiconducting Microcrystallites in Glass"
         J. Appl. Phys. 61(12) 5399 (1987).

[1.5]   "Scientific, Laboratory Glassware, In Clear Fused Quartz" p. 4
         Catalogue, Multilab Ltd.

[1.6]   "Glass - A World History" p. 141
         Kämpfer, F. and Beyer, K.G.
         Studio Vista Ltd. (London) 1966.

[1.7]   "Colored Glasses" chapters XXI, XXIII
         Weyl, W.A.
         Dawson's of Pall Mall (London) 1959.

[1.8]   "Glass" pp. 66-80
         Hurst Vose, R.
         William Collins Sons and Co. (London) 1980.

[1.9]   "Alchemy" p. 218
         Holmyard, E.J.
         D. Appleton and Company (New York) 1924.

[1.10]   "The Story of Early Chemistry" pp. 392, 417-418
         Maxson Stillman, J.
         Penguin Books Ltd. (Harmondsworth) 1957.

[1.11]   "Prelude to Chemistry - An Outline of Alchemy its Literature and Relationships" p. 38
         Reid, J.
         G. Bell and Sons Ltd. (London) 1936.

[1.12]   "Colored Glasses" chapter XVIII
         Weyl, W.A.
         Dawson's of Pall Mall (London) 1959.

[1.13]   "Colored Glasses" pp. 270-272
         Weyl, W.A.
         Dawson's of Pall Mall (London) 1959.

[1.14] Kelly, M.J. and Nicholas, R.J.
"The Physics of Quantum Well Structures"
Rep. Prog. Phys. **48** 1699 (1985).

[1.15] "Physics and Applications of Semiconductor Microstructures" pp. 103-105
Jaros, M.
Clarendon Press (Oxford) 1989.

[1.16] Arnot, H., Andrews, S.R. and Beaumont, S.P.
"Photoluminescence Studies of GaAs-AlGaAs Quantum Dots"
Microelectronic Engineering **9** 365 (1989).

[1.17] Notomi, M., Naganuma, M., Nishida, T., Tamamura, T., Iwamura, H., Nojima, S. and Okamoto, M.
"Clear Energy Level Shift in Ultranarrow InGaAs/InP Quantum Well Wires Fabricated by Reverse Mesa Chemical Etching"
Appl. Phys. Lett. **58**(7) 720 (1991).

[1.18] Brus, L.
"Electronic Wave Functions in Semiconductor Clusters: Experiment and Theory"
J. Phys. Chem. **90** 1555 (1986).

[1.19] Cumberbatch, T.J. and Putnis, A.
"The Preparation of III-V Semiconductors in Aqueous Solutions"
in "Materials Issues in Microcrystalline Semiconductors"
Materials Research Society Symposium Proceedings vol. **164** p. 129
Materials Research Society (Pittsburgh) 1990.

[1.20] Hayashi, S. and Yamamoto, K.
"Amorphous-Like Raman Spectra of Semiconductor Microcrystals"
Superlatt. and Microstruct. **2**(6) 581 (1986).

[1.21] Tonouchi, M., Moriyami, F. and Miyamoto, T.
"Characterisation of μc-Si:H Films Prepared by H_2 Sputtering"
Japan. J. Appl. Phys. (part 2) **29**(3) L385 (1990).

[1.22] Agata, M., Kurase, H., Hayashi, S. and Yamamoto, K.
"Photoluminescence Spectra of Gas-Evaporated CdS Microcrystals"
Solid State Commun. **76**(8) 1061 (1990).

[1.23] Furukawa, S. and Miyasato, T.
"Quantum Size Effects on the Optical and Electrical Properties of Microcrystalline Si:H"
Superlatt. and Microstruct. **5**(3) 317 (1989).

[1.24] Finlayson, N., Banyai, W.C., Seaton, C.T., Stegeman, G.I., O'Neill, M.,
Cullen, T.J. and Ironside, C.N.
"Optical Nonlinearities in CdS_xSe_{1-x} - Doped Glass Waveguides"
J. Opt. Soc. Am. B **6**(4) 675 (1989).

References for Chapter Two

[2.1] "Physics of Semiconducting Devices" 2nd Edition p. 9
Sze, S.M.
John Wiley and Sons (New York) 1981.

[2.2] "Physics and Chemistry of II-VI Compounds" p. 44
Aven, M. and Prener, J.S. (editors)
North Holland Publishing Company (Amsterdam) 1967.

[2.3]   "Current Topics in Materials Science" volume 9 p. 43
         Kaldis, E. (series editor)
         North-Holland Publishing Company (Amsterdam) 1982.

[2.4]   "Landolt-Börnstein Numerical Data and Functional Relationships in Science and Technology"
         Hellwege, K.H. (editor in chief)
         Volume 17 subvolume b p. 225
         Madelung, O. (editor)
         Springer-Verlag (Berlin) 1982.

[2.5]   "Introduction to Solid State Physics" 6th edition p. 133
         Kittel, C.
         John Wiley and Sons (New York) 1986.

[2.6]   "Physics and Chemistry of II-VI Compounds" p. 369
         Aven, M. and Prener, J.S. (editors)
         North Holland Publishing Company (Amsterdam) 1967.

[2.7]   Dutton, D.
         "Fundamental Absorption Edge in Cadmium Sulfide"
         Phys. Rev. 112(3) 785 (1958).

[2.8]   "Current Topics in Materials Science" volume 9 p. 52
         Kaldis, E. (series editor)
         North-Holland Publishing Company (Amsterdam) 1982.

[2.9]   Spiegelberg, F., Gutsche, E. and Voigt, J.
         "Exciton-Phonon Interaction in CdS"
         Phys. Stat. Sol. (b) 77 233 (1976).

[2.10]   "Optical Processes in Semiconductors" pp. 116-119
         Pankove, J.I.
         Dover Publications, Inc. (New York) 1971.

[2.11]   Gilleo, M.A., Bailey, P.T. and Hill, D.E.
         "Free Carrier and Exciton Recombination Radiation in GaAs"
         Phys. Rev. 174(3) 898 (1968).

[2.12]   Pollak, F.H.
         "Raman Characterization of Semiconductors Revisited"
         SPIE Proc. (Bellingham, USA) 452 26 (1983).

[2.13]   Loudon, R.
         "The Raman Effect in Crystals"
         Advan. Phys. 13 423 (1964).

[2.14]   Beserman, R.
         "Zone Edge Phonons in $CdS_{1-x}Se_x$"
         Solid State Commun. 23 323 (1977).

[2.15]   Rama Rao, C.S. and Sundaram, S.
         "Study of Ion-Implanted Damage in GaAs:Be and InP:Be Using Raman Scattering"
         J. Appl. Phys. 54(4) 1808 (1983).

[2.16]   Kelly, M.J. and Nicholas, R.J.
         "The Physics of Quantum Well Structures"
         Rep. Prog. Phys. 48 1699 (1985).

[2.17]   Arakawa, Y.
         "Quantum Well Lasers - Gain, Spectra, Dynamics"
         IEEE J. Quant. Electr. **QE-22**(9) 1887 (1986).

[2.18]   Weisbuch, C. and Nagle, J.
         "On the Impact of Low-Dimensionality in Quantum-Well, Wire and Dot-Semiconductor Lasers"
         in "Science and Engineering of 1 and 0 Dimensional Semiconductor Systems" p.309
         Beaumont, S.P. and Sotomayor Torres, C.M. (editors)
         Plenum Press (New York) 1990.

[2.19]   Ruppin, R. and Englman, R.
         "Optical Phonons of Small Crystals"
         Rep. Prog. Phys. **33** 149 (1970).

[2.20]   Ruppin, R.
         "Size Effects on the Plasmon-Phonon Modes in Polar Semiconductors"
         J. Phys. Chem. Solids **30** 2349 (1969).

[2.21]   Klein, M.V.
         "Phonons in Semiconductor Superlattices"
         IEEE J. Quant. Electr. **QE-22** 1760 (1986).

[2.22]   "Physics and Chemistry of II-VI Compounds" pp. 27-31
         Aven, M. and Prener, J.S.
         North-Holland Publishing Company (Amsterdam) 1967.

[2.23]   Brus, L.E.
         "Electron-Electron and Electron-Hole Interactions in Small Semiconductor Crystallites:
         The Size Dependence of the Lowest Electronic State"
         J. Chem. Phys. **80**(9) 4403 (1984).

[2.24]   Brus, L.
         "Electronic Wave Functions in Semiconductor Clusters: Experiments and Theory"
         J. Phys. Chem. **90** 2555 (1986).

[2.25]   Brus, L.
         "Zero Dimensional "Excitons" in Semiconducting Clusters"
         IEEE J. Quant. Electr. **QE-22**(9) 1909 (1986).

[2.26]   Brus, L.E.
         "A Simple Model for the Ionisation Potential, Electron Affinity and Aqueous Redox Potentials
         of Small Semiconducting Crystallites"
         J. Chem. Phys. **79**(11) 5566 (1983).

[2.27]   "Physics of Semiconducting Devices" 2nd Edition Appendices H and I
         Sze, S.M.
         John Wiley and Sons (New York) 1981.

[2.28]   Éfros, Al.L. and Éfros, A.L.
         "Interband Absorption of Light in a Semiconductor Sphere"
         Sov. Phys. Semicond. **16**(7) 772 (1982).

[2.29]   Ekimov, A.I., Efros, Al.L. and Onushchenko, A.A.
         "Quantum Size Effect in Semiconductor Microcrystals"
         Solid State Commun. **56**(11) 921 (1985).

[2.30]   Bryant, G.W.
         "Excitons in Quantum Boxes: Correlation Effects and Quantum Confinement"
         Phys. Rev. B **37**(15) 8763 (1988).

[2.31] Ekimov A.I., Onushchenko, A.A. and Efros, Al. L.
        "Quantization of the Energy Spectrum of Holes in the Adiabatic Potential of the Electron"
        JETP Lett. 43(6) 377 (1986).

[2.32] Ekimov, A.I., Onushchenko, A.A., Plyukhin, A.G. and Efros, Al.L.
        "Size Quantization of Excitons and Determination of the Parameters of their Energy Spectrum
        in CuCl"
        Sov. Phys. JETP 61 891 (1985).

[2.33] Lifshitz, I.M. and Slezov, V.V.
        "Kinetics and Diffusive Decomposition of Supersaturated Solid Solutions"
        Sov. Phys. JETP 35(2) 331 (1959).

[2.34] Grigoryan, G.B., Kazaryan, É.M., Éfros, Al.L. and Yazeva, T.V.
        "Quantized Holes and the Absorption Edge in Spherical Microcrystals with a Complex
        Valence Band Structure"
        Sov. Phys. Solid State 32(6) 1031 (1990)

[2.35] Nair, S.V., Sinha, S. and Rustagi, K.C.
        "Quantum Size Effects in Spherical Semiconductor Microcrystals"
        Phys. Rev. B 35(8) 4098 (1987).

[2.36] Austin, E.J.
        "Exciton Binding Energies and Absorption Intensities in Quantum Dots"
        Semicond. Sci. Technol. 3 960 (1988).

[2.37] "Quantum Mechanics" pp. 21-23
        Davies, P.C.W.
        Routledge and Kegan Paul (London) 1984.

[2.38] Wu, W-Y, Schulman, J.N., Hsu, T.Y. and Efron, U.
        "Effect of Nonuniformity on the Absorption Spectrum of a Semiconductor Quantum Dot System"
        Appl. Phys. Lett. 51(10) 710 (1987).

[2.39] Kern, K., Demel, T., Heitmann, D., Grambow, P., Zhang, Y.H. and Ploog, K.
        "Quantum Dots in InGaAs-InAlAs-InP Heterostructures"
        Superlatt. and Microstruct. 9(1) 11 (1991).

[2.40] Notomi, M., Naganuma, M., Nishida, T., Tamamura, T., Iwamura, H., Nojima, S. and Okamoto, M.
        "Clear Energy Level Shift in Ultranarrow InGaAs/InP Quantum Well Wires Fabricated by Reverse
        Mesa Chemical Etching"
        Appl. Phys. Lett. 58(7) 720 (1991).

[2.41] Miller, D.A.B., Chemla, D.S. and Schmitt-Rink, S.
        "Electroabsorption of Highly Confined Systems: Theory of the Quantum Confined Franz-Keldysh
        Effect in Semiconductor Quantum Wires and Dots"
        Appl. Phys. Lett. 52(25) 2154 (1988).

[2.42] Hache, F., Ricard, D. and Flytzanis, C.
        "Quantum-Confined Stark Effect in Very Small Semiconductor Crystallites"
        Appl. Phys. Lett. 55(15) 1504 1989.

[2.43] Rockstad, H.K.
        "Application of Electro-Absorption Techniques to the Study of Crystal Particles in Glass"
        Appl. Optics 7(5) 759 (1968).

[2.44] Nomura, S. and Kobayashi, T.
        "Clearly Resolved Exciton Peaks in CdS_xSe_{1-x} Microcrystallites by Modulation Spectroscopy"
        Solid State Commun. 73(6) 425 (1990).

[2.45]   Henneberger, F., Puls, J., Rossmann, H., Woggon, U., Freundt, S., Spiegelberg, Ch.
and Schülzen, A.
"Nonlinear Optical Properties of Wide-Gap II-VI Bulk Semiconductors and Microcrystallites"
J. Crystal Growth **101** 632 (1990).

[2.46]   Nair, S.V. and Rustagi, K.C.
"Saturating Optical Resonances in Quantum Dots"
Superlatt. and Microstruct. **6**(4) 377 (1989).

[2.47]   Jungk, G.
"Optical Bistability in Composite Media"
Phys. Stat. Sol. b **144** 335 (1988).

[2.48]   Peschel, Th.
"Possibilities for Intrinsic Optical Bistability in Semiconductor-Doped Glass"
Phys. Stat. Sol. b **159** 291 (1990).

[2.49]   Takagahara, T.
"Excitonic Optical Nonlinearities and Exciton Dynamics in Semiconductor Quantum Dots"
Phys. Rev. B **36**(17) 9293 (1987).

[2.50]   Banyai, L., Hu, Y.Z., Lindberg, M. and Koch, S.W.
"Third-Order Optical Nonlinearities in Semiconductor Microstructures"
Phys. Rev. B **38**(12), 8142 (1988).

[2.51]   Schmitt-Rink, S., Miller, D.A.B. and Chemla, D.S.
"Theory of the Linear and Nonlinear Optical Properties of Semiconductor Microcrystallites"
Phys. Rev. B **35**(15) 8113 (1987).

[2.52]   Hanamura, E.
"Very Large Optical Nonlinearities of Semiconductor Microcrystallites"
Phys. Rev. B **37**(3) 1273 (1988).

[2.53]   Miyamoto, Y., Miyake, Y., Asada, M. and Suematsu, Y.
"Threshold Current Density of GaInAsP/InP Quantum Box Lasers"
IEEE J. Quant. Electr. QE-**25**(9) 2001 (1989).

[2.54]   Vahala, K.J.
"Quantum Box Fabrication Tolerance and Size Limits in Semiconductors and their Effect
on Optical Gain"
IEEE J. Quant. Electr. QE-**24**(3) 523 (1988).

[2.55]   Asada, M., Miyamoto, Y. and Suematsu, Y.
"Gain and the Threshold of Three-Dimensional Quantum Box Lasers"
IEEE J. Quant. Electr. QE-**22**(9) 1915 (1986).

[2.56]   Scott, J.F. and Damen, T.C.
"Raman Scattering from Surface Modes of Small CdS Crystallites"
Optics Commun. **5**(5) 410 (1972).

[2.57]   Watt, M., Sotomayor Torres, C.M., Arnot, H.E.G. and Beaumont, S.P.
"Surface Phonons in GaAs Cylinders"
Semicond. Sci. Technol. **5** 285 (1990).

[2.58]   Zhou, F., Sun, Y. and Pan, J.
"Raman Scattering of CdS and CdS_xSe_{1-x} Microcrystals in a Glass Medium"
J. of Luminescence **40&41** 739 (1988).

[2.59]   Campbell, I.M. and Fauchet, P.M.
         "The Effect of Microcrystallite Size and Shape on the One Phonon Raman Spectra of
         Crystalline Semiconductors"
         Solid State Commun. 58(10) 739 (1986).

[2.60]   Campbell, I.M. and Fauchet, P.M.
         "The Raman Spectrum of Semiconductor Nanograins"
         "18th International Conference on the Physics of Semiconductors"
         Stockholm, Sweden 1988 p.1357
         World Scientific Publishing Co. (Singapore) 1988.

[2.61]   Ohtani, N. and Kawamura, K.
         "Theoretical Investigation of Raman Scattering from Microcrystallites"
         Solid State Commun. 75(9) 711 (1990).

[2.62]   Richter, H., Wang, Z.P. and Ley, L.
         "The One Phonon Raman Spectrum in Microcrystalline Silicon"
         Solid State Commun. 39 625 (1981).

[2.63]   Fauchet, P.M.
         "The Raman Lineshape of Semiconductor Nanocrystals"
         in "Light Scattering in Semiconductor Structures and Superlattices" p. 229
         Lockwood, D.J. and Young, J.F. (editors)
         Plenum Press (New York) 1991.

[2.64]   "Landolt-Börnstein Numerical Data and Functional Relationships in Science and Technology"
         Hellwege, K.H. (editor in chief)
         Volume 17   subvolume b   p. 213, 421 & 422
         Madelung, O. (editor)
         Springer-Verlag (Berlin) 1982,

[2.65]   Nusimovici, M.A. and Birman, J.L.
         "Lattice Dynamics of Wurtzite: CdS"
         Phys. Rev. 156(3) 925 (1967).

[2.66]   "Solid State Physics" p. 483
         Ashcroft, N.W. and Mermin, N.D.
         Holt, Rinehart and Winston (Philadelphia) 1976.

[2.67]   Tu, A. and Persans, P.D.
         "Raman Scattering in Semiconductor Nanocrystals"
         Clusters and Cluster-Assembled Materials 206 97 (1991).

References for Chapter Three

[3.1]   Borrelli, N.F., Hall, D.W., Holland, H.J. and Smith, D.W.
         "Quantum Confinement Effects of Semiconducting Microcrystallites in Glass"
         J. Appl. Phys. 61 9120, 5399 (1987).

[3.2]   Potter, B.G. and Simmons, J.H.
         "Quantum Size Effects in Optical Properties of CdS Glass Composites"
         Phys. Rev. B 37(18), 10838 (1988).

[3.3]   "The Physical Properties of Glass"   chapter 7
         Holloway, D.G.
         Wykeham Publications (London) Ltd. 1973.

[3.4]   "Crystallization" chapter 5
         Mullin, J.W.
         Butterworths and Co. (London) 1961.

[3.5]   Lifshitz, I.M. and Slyezov, V.V.
         "The Kinetics of Precipitation from Supersaturated Solid Solution"
         J. Phys. Chem. Solids 19(1/2) 35 (1961).

[3.6]   Lifshitz, I.M. and Slezov, V.V.
         "Kinetics and Diffusive Decomposition of Supersaturated Solid Solutions"
         Sov. Phys. JETP 35(2) 331 (1959).

[3.7]   Schmelzer, J., Pascova, R. and Gutzow, I.
         "Cluster Growth and Ostwald Ripening in Viscoelastic Media"
         Phys. Stat. Sol. a 117 363 (1990).

[3.8]   Voorhees, P.W. and Glicksman, M.E.
         "Solution to Multi-particle Diffusion Problem with Applications to Ostwald
         Ripening - I. Theory"
         Acta Metall. 32(11) 2001 (1984).

[3.9]   Voorhees, P.W. and Glicksman, M.E.
         "Solution to the Multi-Particle Diffusion Problem with Applications to Ostwald
         Ripening - II. Computer Simulations"
         Acta Metall. 32(11) 2013 (1984).

[3.10]   Ekimov, A.I., Efros, Al.L. and Onushchenko, A.A.
         "Quantum Size Effect in Semiconductor Microcrystals"
         Sol. State Commun. 56(11) 921 (1985).

[3.11]   "Small Angle X-Ray Scattering"
         Guinier, A. and Fournet, G.
         John Wiley and Sons 1955.

[3.12]   Woggon, U., Müller, M., Lembke, I., Rückmann, I. and Cesnulevicius, J.
         "Growth and Characterisation of Semiconductor Microcrystallites in a Glass Matrix with Respect to
         their Nonlinear Optical Properties"
         Superlatt. and Microstruct. 9(2) 245 (1991).

References for Chapter Four

[4.1]   Watt, M.
         "Inelastic Light Scattering by Low Dimensional Structures" Chapter 4
         PhD Thesis, University of Glasgow 1989.

[4.2]   Ferguson, I.
         "Optical Properties of Novel GaAs-Based Semiconductors" Chapter 2
         PhD Thesis, University of St Andrew's 1989.

[4.3]   "Model 2030 High Power Ion Laser Instruction Manual"
         Spectra Physics Laser Products Division.

[4.4]   "Model 2040 and 2045 High Power Ion Laser Instruction Manual"
         Spectra Physics Laser Products Division.

[4.5]   "Laserspec III Instruction Manual"
         Spectrolab X-Ray Systems Electro-Optics.

[4.6]   "Laserspec III"
        Technical Literature Spectrolab Electro-Optics.

[4.7]   "Spectralink Technical Manual" version 2.1
        Jobin Yvon Division d'Instruments S.A.

[4.8]   "Luminescence Spectroscopy"
        Lumb, M.D. (editor)
        Section 3 p. 185 by T.D.S. Hamilton and I.H. Munro
        Academic Press (London) 1978.

[4.9]   "Ramanor U1000 Monochromator Operating Instructions"
        Jobin Yvon Division d'Instruments S.A.

[4.10] "Enhanced Prism Software Instruction Manual" version 1.2
        Jobin Yvon Division d'Instrument S.A.

[4.11] "Instructions Models 3457, 3461, 3463, 3470 Thermoelectric PMT Housings"
        Pacific Instruments Inc.

[4.12] "Model 33 Power Supply / Temperature Controller Operation and Maintenance Manual"
        Pacific Instruments Inc.

[4.13] "Equilibrium Thermodynamics" 3rd Edition pp. 174-5
        Adkins, C.J.
        Cambridge University Press 1983.

[4.14] "Photomultiplier Power Supply Type PM 28B and Type PM 28B/VP Operating Manual"
        Thorn EMI Electron Tubes Ltd.

[4.15] "Accessories for Photomultiplier Tubes"
        Hamamatsu Photonics K.K., Electron Tubes Division.

[4.16] "The Design of Optical Spectrometers" p. 73
        James, J.F. and Sternberg R.S.
         Chapman and Hall 1969.

[4.17] "Model 780 Tungsten Halogen Lamp Source"
        Newport Corporation.

[4.18] "CRC Handbook of Chemistry and Physics" 63rd Edition 1982-83 p. F-109
        Weast, R.C. (editor)
        CRC Press Inc. (Florida) 1982.

[4.19] "RS Components Part1 Electronic and Electrical Components" Nov 1991 - Feb 1992 p. 1053
        RS Components Ltd.

[4.20] "Labmaster Laser Measurement System"
        Coherent Components Group.

[4.21] "RS Components Part1 Electronic and Electrical Components" Nov 1991 - Feb 1992 p. 522
        RS Components Ltd.

[4.22] "The Design of Optical Spectrometers" p. 191
        James, J.F. and Sternberg R.S.
         Chapman and Hall 1969.

[4.23] "Optical Glass Filters"
        Schott Glaswerke.

[4.24]   "THR1000 Instruction Manual"
          Jobin Yvon Division d'Instrument S.A.

[4.25]   "THR1000 Monochromator / Spectrometer" Technical Literature
          Jobin Yvon Division d'Instrument S.A.

[4.26]   "Newport Catalogue" 1989 p. N-87
          Newport Corporation.

[4.27]   "RS Components Part1 Electronic and Electrical Components" Nov 1991 - Feb 1992 p. 813
          RS Components Ltd.

[4.28]   "Microelectronics - Digital and Analogue Circuits and Systems" pp. 625-7
          Millman, J.
          McGraw-Hill Book Company 1979.

References for Chapter Five

[5.1]   "Landolt-Börnstein Numerical Data and Functional Relationships in Science and Technology"
          Hellwege, K.H. (editor in chief)
          Volume 17 subvolume b p. 317
          Madelung, O. (editor)
          Springer-Verlag (Berlin) 1982.

[5.2]   Savatinova, I. and Nikiforova, M.
          "Raman Study of Phonon Processes in CdS_xSe_{1-x} Mixed Crystals"
          Spectro. Lett. 7(12) 597 (1974).

[5.3]   Chang, I.F. and Mitra, S.S.
          "Application of a Modified Random-Element-Isodisplacement Model to Long-Wavelength Optical
          Phonons of Mixed Crystals"
          Phys. Rev. B 172(3) 1924 (1968).

[5.4]   Tu, A. and Persans, P.D.
          "Raman Scattering as a Compositional Probe of II-VI Ternary Semiconductor Nanocrystals"
          Appl. Phys. Lett. 58(14) 1506 (1991).

[5.5]   Persans, P.D., Tu, A., Lewis, M., Driscoll, T. and Redwing, R.
          "Optical Properties of II-VI Semiconductor Doped Glass"
          in "Materials Issues in Microcrystalline Semiconductors"
          Materials Research Society Symposium Proceedings vol. 164 p. 105
          Materials Research Society (Pittsburgh) 1990.

[5.6]   Borrelli, N.F., Hall, D.W., Holland, H.J. and Smith, D.W.
          "Quantum Confinement Effects of Semiconducting Microcrystallites in Glass"
          J. Appl. Phys. 61(12) 5399 (1987).

[5.7]   Hache, F., Klein, M.C., Ricard, D. and Flytzanis, C.
          "Photoluminescence Study of Schott Commercial and Experimental CdSSe - Doped Glasses:
          Observation of Surface States"
          J. Opt. Soc. Am. B 8(9) 1802 (1991).

[5.8]   Brus, L.
          "Zero Dimensional "Excitons" in Semiconductor Clusters"
          IEEE J. Quant. Electron. QE-22(4) 1909 (1986).

[5.9]   Potter, B.G. and Simmons, J.H.
         "Quantum Size Effects in Optical Properties of CdS-Glass Composites"
         Phys. Rev. B 37(11) 10838 (1988).

[5.10]   Shinojima, H., Yumoto, J., Uesugi, N., Omi, S. and Asahara, Y.
         "Microcrystallite Size Dependence of Absorption and Photoluminescence Spectra in
         CdS_xSe_{1-x} - Doped Glass"
         Appl. Phys. Lett. 55(15) 1519 (1989).

[5.11]   Warnock, J. and Awschalom, D.D.
         "Picosecond Studies of Electron Confinement in Simple Colored Glasses"
         Appl. Phys. Lett. 48(6) 425 (1986).

[5.12]   Warnock, J. and Awschalom, D.D.
         "Quantum Size Effects in Simple Colored Glass"
         Phys. Rev. B 32(8) 5529 (1985).

[5.13]   Uhrig, A., Banyai, L., Hu, Y.Z., Koch, S.W., Klingshirn, C. and Neuroth, N.
         "High-Excitation Photoluminescence Studies of $CdS_{1-x}Se_x$ Quantum Dots"
         Z. Phys. B - Condensed Matter 81 385 (1990).

[5.14]   Uhrig, A., Banyai, L., Hu, Y.Z., Koch, S.W., Gaponenko, S., Neuroth, N. and Klingshirn, C.
         "High- and Low-Excitation Photoluminescence Studies of CdS_xSe_{1-x} Quantum Dots"
         20th International Conference on the Physics of Semiconductors" vol. 1
         Anastassakis, E.M. and Joannopoulos, J.D. (editors)
         Thessaloniki, Greece August 6-10, 1990, p. 2395
         World Scientific Publishing Co. (Singapore) 1990.

[5.15]   Roussignol, P., Ricard, D., Lukasik, J. and Flytzanis, C.
         "New Results on Optical Phase Conjugation in Semiconductor-Doped Glasses"
         J. Opt. Soc. Am. B 4(1) 5 (1987).

[5.16]   Tomita, M., Matsumoto, T. and Matsuoka, M.
         "Nonlinear Dynamical Relaxation Processes in Semiconductor-Doped Glass at Liquid-Nitrogen
         Temperature"
         J. Opt. Soc. Am. B 6(2) 165 (1989).

[5.17]   Zhang, J., Gan, F. and Qi, C.
         "Spectral Properties of CdS(Se) Microcrystallites in Amorphous Media"
         J. Lumin. 40&41 741 (1988).

[5.18]   Zheng, J.P. and Kwok, H.S.
         "Ultrafast Carrier Dynamics in Modified Semiconductor Doped Glass"
         Appl. Phys. Lett. 54(1) 1 (1989).

[5.19]   Mitsunaga, M., Shinojima, H. and Kubodera, K.
         "Laser Annealing Effect on Carrier Recombination Time in CdS_xSe_{1-x} - Doped Glasses"
         J. Opt. Soc. Am. B 5(7) 1448 (1988).

[5.20]   Chepic, D.I., Efros, Al.L., Ekimov, A.I., Ivanov, M.G., Kharchenko, V.A., Kudriavtsev, A.I.
         and Yazeva, T.V.
         "Auger Ionization of Semiconductor Quantum Drops in a Glass Matrix"
         J. Lumin. 47 113 (1990).

[5.21]   Horan, P. and Blau, W.
         "Photodarkening Effect and the Optical Nonlinearity in a Quantum-Confined, Semiconductor-Doped
         Glass"
         J. Opt. Soc. Am. B 7(3) 304 (1990).

[5.22]   Kull, M., Coutaz, J.L., Manneberg, G. and Grivickas, V.
         "Absorption Saturation and Photodarkening in Semiconductor-Doped Glasses"
         Appl. Phys. Lett. 54(19) 1830 (1989).

[5.23]   "Luminescence Spectroscopy"
         Lumb, M.D. (editor)
         Section 3.1.2 by T.D.S. Hamilton and I.H. Munro
         Academic Press (London) 1978.

[5.24]   "Optical Glass Filters"
         Schott Glasswerke.

[5.25]   "CRC Handbook of Chemistry and Physics" 63rd edition p. F-52
         Weast, R.C. (editor)
         CRC Press Inc. (Florida) 1982.

[5.26]   Zhou, F., Sun, Y. and Pan, J.
         "Raman Scattering of CdS and CdS_xSe_{1-x} Microcrystals in the Glass Medium"
         J. Lumin. 40&41 739 (1988).

[5.27]   Bustarret, E., Hachicha, M.A. and Brunel, M.
         "Experimental Determination of the Nanocrystalline Volume Fraction in Silicon Thin Films from
         Raman Scattering"
         Appl. Phys. Lett. 52(20) 1675 (1988).

[5.28]   Scamarcio, G., Lugara, M. and Manno, D.
         "Size-Dependent Lattice Contractions in $CdS_{1-x}Se_x$ Nanocrystals Embedded in Glass Observed by
         Raman Scattering"
         Phys. Rev. B 45(23) 13792 (1992).

[5.29]   Cumberbatch, T.J. and Putnis, A.
         "The Preparation of III-V Semiconductors in Aqueous Solution"
         in "Materials Issues in Microcrystalline Semiconductors"
         Materials Research Society Symposium Proceedings vol. 164 p. 129
         Materials Research Society (Pittsburgh) 1990.

[5.30]   "Landolt-Börnstein Numerical Data and Functional Relationships in Science and Technology"
         Hellwege, K.H. (editor in chief)
         Volume 17 subvolume a pp. 304, 575
         Madelung, O. (editor)
         Springer-Verlag (Berlin) 1982.

[5.31]   Carles, R., Saint-Cricq, N., Renucci, J.B. and Zwick, A.
         "Second-Order Raman Scattering in InAs"
         Phys. Rev. B 22(10) 4804 (1980).

[5.32]   "Laser Handbook" chapter E8 p. 1416 by Mooradian, A.
         Arecchi, F.T. and Schulz-DuBois, E.O. (editors)
         North-Holland Publishing Company (Amsterdam) 1972.

[5.33]   Tonouchi, M., Moriyama, F. and Miyasato, T.
         "Characterisation of μc-Si:H Films Prepared by H_2 Sputtering"
         Japan J. Appl. Phys. (part 2) 29(3) L385 (1990).

[5.34]   Ovsyuk, N.N., Gorokhov, E.B., Grishchenko, V.V. and Shebanin, A.P.
         "Low-Frequency Raman Scattering by Small Semiconductor Particles"
         JETP Lett. 47(5) 298 (1988).

[5.35]   Hayashi, S., Ito, M. and Kanamori, H.
         "Raman Study of Gas-Evaporated Germanium Microcrystals"
         Solid State Commun. 44(1) 75 (1982).

[5.36]   "Hayashi, S. and Abe, H.
         "Implications of Amorphous-Like Raman-Spectra of Gas-Evaporated Si and Ge Microcrystals"
         Japan J. Appl. Phys. (part 1) 23 824 (1984).

[5.37]   Hayashi, S. and Yamamoto, K.
         "Amorphous-Like Raman Spectra of Semiconductor Microcrystals"
         Superlatt. and Microstruct. 2(6) 581 (1986).

[5.38]   Hayashi, S.
         "Amorphous-Like Raman Spectra of GaP Microcrystals"
         Solid State Commun. 56(4) 375 (1985).

[5.39]   Fujii, M., Hayashi, S. and Yamamoto, K.
         "Raman Scattering from Quantum Dots of Ge Embedded in SiO_2 Thin Films"
         Appl. Phys. Lett. 57(25) 2692 (1990).

[5.40]   Okada, T., Iwaki, T., Yamamoto, K., Kasahara, H. and Abe, K.
         "Raman Scattering from Gas-Evaporated Silicon Small Particles"
         Solid State Commun. 49(8) 809 (1984).

[5.41]   Furukawa, S. and Miyasata, T.
         "Quantum Size Effects on the Optical Band Gap of Microcrystalline Si:H"
         Phys. Rev. B 38 5726 (1988).

[5.42]   Furukawa, S. and Miyasato, T.
         "Quantum Size Effects on the Optical and Electrical Properties of Microcrystalline Si:H"
         Superlatt. and Microstruct. 5(3) 317 (1989).

[5.43]   Furukawa, S. and Miyasato, T.
         "Three-Dimensional Quantum Well Effects in Ultrafine Silicon Particles"
         Japan. J. Appl. Phys. (part 2) 27 L2207 (1988).

[5.44]   Yamamoto, M., Hayashi, R., Tsunetomo, K., Kohno, K. and Osaka, Y.
         "Preparation and Properties of Si Microcrystals Embedded in SiO_2 Glass Films"
         Japan. J. Appl. Phys. (part 1) 30(1) 136 (1991).

[5.45]   Canham, L.T.
         "Silicon Quantum Wire Array Fabrication by Electrochemical and Chemical Dissolution of Wafers"
         Appl. Phys. Lett. 57(10) 1046 (1990).

[5.46]   "Red Light from Warm Silicon"
         Electronic World + Wireless World p. 936 Nov. 1990

[5.47]   Hecht, J.
         "Does Etching Lend Light to Silicon"
         Scientific American p. 18 16th May 1992.